

DISSERTATION

SOFT X-RAY LASER INTERFEROMETRY OF DENSE PLASMAS

Submitted by

Jorge Filevich

Department of Physics

In partial fulfillment of the requirements

for the degree of Doctor of Philosophy

Colorado State University

Fort Collins, Colorado

Summer 2007

UMI Number: 3279509

INFORMATION TO USERS

The quality of this reproduction is dependent upon the quality of the copy submitted. Broken or indistinct print, colored or poor quality illustrations and photographs, print bleed-through, substandard margins, and improper alignment can adversely affect reproduction.

In the unlikely event that the author did not send a complete manuscript and there are missing pages, these will be noted. Also, if unauthorized copyright material had to be removed, a note will indicate the deletion.

UMI[®]

UMI Microform 3279509

Copyright 2007 by ProQuest Information and Learning Company.

All rights reserved. This microform edition is protected against unauthorized copying under Title 17, United States Code.

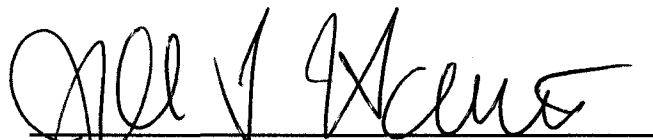
ProQuest Information and Learning Company
300 North Zeeb Road
P.O. Box 1346
Ann Arbor, MI 48106-1346

COLORADO STATE UNIVERSITY

June 11, 2007

WE HEREBY RECOMMEND THAT THE DISSERTATION PREPARED UNDER OUR SUPERVISION BY JORGE FILEVICH ENTITLED "SOFT X-RAY LASER INTERFEROMETRY OF DENSE PLASMAS" BE ACCEPTED AS FULFILLING IN PART REQUIREMENTS FOR THE DEGREE OF DOCTOR OF PHILOSOPHY.

Committee on Graduate Work



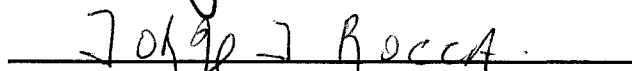
Prof. John Harton



Prof. Siu Au Lee



Prof. Paul J. Wilbur



Adviser: Prof. Jorge J. G. Rocca



Department Chair: Prof. Hans D. Hochheimer

ABSTRACT OF DISSERTATION

SOFT X-RAY LASER INTERFEROMETRY OF DENSE PLASMAS

This Dissertation presents the results of the study of plasmas using soft x-ray laser interferometry. The use of soft x-ray wavelengths (14.7 nm and 46.9 nm) permits probing plasmas that are more dense and that have steeper density gradients than those that can be probed using optical interferometry, opening the opportunity to uncover new dense plasma phenomena. The use of diffraction gratings as beam splitters permitted the construction of a novel interferometer design that is robust, stable and with high throughput. The measurements conducted include the first demonstration of soft x-ray laser interferometry with picosecond resolution.

The interferometer was used extensively to probe laser-created plasmas. Two of the main results are presented herein. The first is the observation of an unexpected on-axis density depression in narrow-focus laser-created plasmas. The density depression is caused by plasma-radiation-induced ablation of target material outside of the region irradiated by the plasma-heating laser. This colder material expands at a slower velocity than the hotter central region, resulting in the observed on axis density depression. The effect is shown to be a general phenomenon, present in many narrow focus plasmas under different irradiation conditions. This was verified using three different irradiation conditions: a 13 ns long pulse in both

30 μm wide line focus and point focus geometries impinging on solid copper targets, with irradiation intensities of $\sim 10^{11} \text{ Wcm}^{-2}$ and $\sim 10^{12} \text{ Wcm}^{-2}$ respectively, and a short, 600 ps pulse in a 12 μm wide line focus geometry impinging on solid aluminum targets with an irradiation of $\sim 10^{13} \text{ Wcm}^{-2}$. The onset of the density depression changes in time and distance from the target, but the general physical picture is the same in all cases. The second set of results unveiled the significant contribution of bound electrons to the index of refraction of multiply ionized plasmas. In a series of experiments that mapped the evolution of plasmas created on flat aluminum targets using a $\lambda=14.7 \text{ nm}$ laser beam, interference fringes that bent in the direction opposite to that expected were observed. This result contradicted the widely accepted assumption that the index of refraction for multiply ionized plasmas at soft x-ray wavelengths only depends on the free electrons. The contribution of bound electrons to the index of refraction is shown to be significant even relatively far away from resonances, and to affect a broad range of wavelengths due to numerous bound-bound and bound-free transitions of the many ionization stages present in the plasma. Moreover, the contribution of bound electrons to the index of refraction was shown to be important in several materials at different probe soft x-ray wavelengths. In particular, bound electron contributions to the index of refraction of tin, silver and carbon plasmas at $\lambda=46.9 \text{ nm}$ were predicted and observed experimentally. This fundamental result affects not only the interpretation of soft x-ray interferograms for plasma density measurements, but also the propagation of soft x-ray light in plasmas in general.

Jorge Filevich
Department of Physics
Colorado State University
Fort Collins, Colorado 80523
Summer 2007

ACKNOWLEDGEMENTS

I would like to thank Prof. Jorge Rocca for the opportunity to work at Colorado State University and for his constant and supportive guidance. I would like to thank my committee members, Dr. Siu Au Lee, Dr. John Harton and Dr. Paul Wilbur for their critical reading of the manuscript. I would also like to acknowledge Dr. James Dunn for the fructuous collaboration in the LLNL experiments. I have worked together with many people and always learnt something from each. At Colorado State University: Mario Marconi, Kelly Kanizay, Brad Luther, Eric Hammarsten, Elizabeth Jankowska, Jonathan Grava, Mike Purvis, and many more. At LLNL: Ray Smith, Jim Hunter and Roisin Keenan. To everybody else in the lab. To the people outside the lab that helped me get distracted from work, the underwater hockey clubs, many skiing partners, my friends. To Orri and Soley, for the L^AT_EX template and help. To Betty Shoemaker.

A mi Familia por estar siempre.

TABLE OF CONTENTS

1	Introduction	1
1.1	Studies of plasmas	5
1.1.1	Laser-created plasmas	7
1.1.2	Magneto-hydrodynamic computer codes	8
1.2	Diagnostics techniques for laser-created plasmas	11
1.2.1	Temperature measurement	12
1.2.2	Density measurement	13
1.3	The index of refraction of a plasma	15
1.4	Soft X-Ray Lasers	26
1.4.1	Ne-Like Ar soft x-ray laser	29
1.4.2	Ni-like Pd soft x-ray laser	31
	Bibliography	35
2	Diffraction Grating Soft X-Ray Laser Interferometry	43
2.1	Interferometry	45
2.2	Advantages of shorter probe wavelengths in plasma interferometry	47
2.2.1	Refraction of the probe beam	48
2.2.2	Absorption of the probe beam	51
2.2.3	Detectable fringe density	55
2.3	Review of previous soft x-ray laser interferometers	57
2.3.1	Wavefront division soft x-ray interferometers	58
2.3.2	Amplitude division soft x-ray interferometers	61
2.4	Diffraction Grating Interferometer	63
2.4.1	Alignment of the interferometer	65
2.4.2	Detector systems	69
2.4.3	Proof of principle experiments	73
2.5	Picosecond resolution plasma probing	75
2.6	Conclusions	79
	Bibliography	80
3	Two dimensional effects in laser created plasmas	86
3.1	Two Dimensional effects in copper line-focus plasmas	89
3.2	Density depression in aluminum plasmas with a 600 ps heating pulse	100

3.3	Density depression in point-focus laser-created plasmas	107
3.4	Conclusions	115
	Bibliography	116
4	Multiply Ionized plasma with index of refraction greater than one	121
4.1	Setup for the experiments	124
4.2	Observation of anomalous fringe shifts in aluminum plasmas	127
4.3	Interpretation of the anomalous fringe shifts in aluminum	131
4.4	Average Atom method	139
4.5	Anomalous fringe shifts at 46.9 nm	142
4.6	Plasma interferometry setup for the 46.9 nm experiments	145
4.7	Anomalous fringe shifts in tin plasmas probed at 46.9 nm	147
4.8	Anomalous fringe shifts in Silver plasmas probed at 46.9 nm	151
4.9	Anomalous fringe shifts in carbon plasmas probed at 46.9 nm	153
4.10	Cu, Al and Mo plasmas probed at 46.9 nm	160
4.11	Conclusions	164
	Bibliography	165
5	Summary	172

LIST OF FIGURES

1.1	Real and imaginary parts of the index of refraction for a material showing resonances in the visible, ultraviolet and EUV regions of the spectrum.	23
1.2	Schematic diagram of a four level lasing system for soft x-ray by collisional electron impact excitation.	28
1.3	Schematic design of the capillary discharge soft x-ray laser.	30
1.4	Photograph of the capillary discharge 46.9 nm soft x-ray laser. The multimeter is included as a size reference.	31
1.5	COMET laser at Lawrence Livermore National Laboratory.	32
1.6	Focusing system used to create a traveling wave line focus for soft x-ray laser excitation, by using an echelon reflector.	33
1.7	Temporal profile of the Ni-like Pd 14.7 nm x-ray laser probe emitted from a 1 cm target and pumped by a 6.7 ps short pulse [0.38].	34
2.1	Ray propagating through a plasma, showing the refraction length L_r , that is shorter than the plasma length L	48
2.2	Numerical computations of the trajectories of rays traveling through a plasma with an exponential density profile given by equation 2.9. The plasma is assumed to be uniform along the direction of propagation. The shorter wavelength rays (46.9 nm and 14.7 nm) experience much less deflection than the 4 th harmonic of a YAG laser (266 nm). Notice that the horizontal scale is 10 times larger than the vertical scale.	50
2.3	Transmission in a 1 mm long plasma due to free-free absorption as a function of the wavelength for a 100 eV plasma with a mean ionization of 10, for three different plasma electron densities.	53
2.4	Parameter space accessible for different probe wavelength due to the limitations imposed by refraction and free-free absorption.	54
2.5	Simulated interferograms for different probe wavelengths show the effect of reducing the wavelength on the number of fringe shifts. All the interferograms were computed using the same density profile, a radially decreasing exponential given by equation 2.12. The peak density was 10^{21} cm^{-3}	56

2.6	Schematic diagram of the Lloyd's mirror interferometer. The real source S and the virtual source S' (formed by a reflection on the mirror) interfere and fringes can be observed on the screen.	59
2.7	Schematic diagram of the Fresnel bi-mirror interferometer. The interference pattern is formed by the overlap of the two portions of the beam produced by the tilt of the mirrors.	60
2.8	Schematic diagram of the Mach-Zehnder interferometer based on thin film beam splitters and used in combination with a neon-like yttrium x-ray laser ($\lambda = 15.5$ nm).	62
2.9	Schematic diagram of the Diffraction Grating Interferometer with the target position and the plasma forming beam indicated in the drawing.	63
2.10	Position of the Low magnification and Foot print camera used to facilitate the alignment in the 14.7 nm version of the DGI. The flip mirrors were placed at the position where the output and input beams intercept the dashed line.	70
2.11	Transmission curve for 1000 Å Al filter that can be used to block the stray light and plasma self emission from reaching the CCD camera. The transmission was obtained from the Lawrence Berkely Laboratory tool available at: http://www.cxro.lbl.gov	71
2.12	Transmission curve for Å Zr + 1000 Å polyimide ($C_{22}H_{10}N_2O_5$) filter used to block the stray light and plasma self emission from reaching the CCD camera. The transmission was obtained from the Lawrence Berkely Laboratory tool available at: http://www.cxro.lbl.gov	72
2.13	Photograph of the Diffraction Grating Interferometer used in the first experiments with the 46.9 nm probe laser.	74
2.14	Sequence of interferograms depicting the evolution of a copper plasma.	76
2.15	Two synthesized interferograms created by averaging a LASNEX simulated plasma evolving over 500 ps and 5 ps respectively. The structure observed on the 500 ps interferogram, for example fringes that bifurcate, is due to the averaging over a changing plasma.	78
3.1	Picture of the experimental setup used, that includes the Diffraction Grating Interferometer, the capillary discharge soft x-ray laser and the plasma forming Nd:YAG laser.	91
3.2	Sequence of soft x-ray interferograms describing the evolution of 1.8 mm long plasma generated by focusing a 13 ns FWHM Nd:YAG laser pulses with 0.6 J energy onto a ~ 30 μ m wide line on a copper target. The time delays are measured with respect to the beginning of the laser pulse. A very noticeable change in the curvature of the fringes is seen starting in the 6 ns frame.	93

3.3	Sequence of two-dimensional density maps depicting the evolution of the electron density of a copper plasma, extracted from the interferograms in Fig. 3.2.	95
3.4	Image of the line focus used to generate the plasma of figure 3.2. The lineouts show very small structure on the beam.	96
3.5	Simulated electron density (line contours) and temperature (filled contour) profiles of the line focus plasma of figure 3 computed using LASNEX. The heating laser is incident from the right. The calculations were done for a 10^{11} Wcm ⁻² , 13 ns FWHM laser pulse. . . .	98
3.6	Simulated density (line contours) and electron temperature (filled contour) profiles for the line focus plasma at 12 ns (left), and with the motion of the ablated material from the target outside the spot constrained (right). Otherwise the conditions for the two simulations are identical. The heating laser is incident from the top. Both figures are calculated at the peak of the 10^{11} Wcm ⁻² , 13 ns FWHM laser pulse.	99
3.7	14.7 nm x-ray laser interferogram measured at 0.3 ns after the peak of the laser pulse of aluminum plasma heated at 10^{13} Wcm ⁻² in 12 μ m (FWHM) focus. The laser is incident from right side. A density depression is observed on-axis	102
3.8	Density profile extracted from the interferograms in Fig. 3.7.	104
3.9	(a) 14.7 nm x-ray laser interferogram of an aluminum plasma heated with 10^{13} Wcm ⁻² in 12 μ m (FWHM) focus, measured at 0.3 ns after the peak of the laser pulse. (b) Density contours extracted from the interferogram. (c) 2-D LASNEX simulations corresponding to the same plasma at the same time. The extended sequence is shown in Fig. 3.7.	105
3.10	2-D LASNEX simulations corresponding to an aluminum target heated by a 600 ps pulse at 10^{13} Wcm ⁻² in a 10 μ m square spatial focus. The laser is incident from the left. The 10^{20} and 10^{21} cm ⁻³ contours are indicated by the gray and black filled circles.	106
3.11	Schematic representation of the plasmas formed inside the target in first and fifth shots and how much the plasma is extended.	109
3.12	Sequence of interferograms corresponding to spot-focus plasmas generated firing a 5 th shot in the same location on a copper target. The spot diameter was ~ 30 μ m and the beam intensity was 7×10^{12} cm ⁻³ . The times indicated are measured with respect to the beginning of the laser pulse.	110
3.13	Plasma density profiles corresponding to the interferograms of Fig. 3.12	112

3.14	Sequence of simulated electron density (line contours) and temperature (filled contour) profiles for the spot-focus plasma of Fig. 3.12 computed using LASNEX. The heating laser is incident from the right	114
4.1	Schematic illustration of the Diffraction Grating Interferometer tailored to work at $\lambda = 14.7$ nm.	126
4.2	Sequence of soft x-ray laser interferograms ($\lambda = 14.7$ nm) of Al line focus plasmas. The plasmas were generated by a 3.1 J heating beam focused into a $12 \mu\text{m} \times 3.1$ mm line focus. The times are measured respect to the peak of the 600 ps heating pulse. Fringes that bend toward the target are clearly observed in the last two frames in the periphery of the plasma and close to the target surface (yellow circle).	128
4.3	Fringe shift maps obtained from the interferograms in Fig. 4.2. The maps show that the regions where the largest densities were present now have negative fringe shifts. It is not possible to compute an electron density map from the fringe shift information because the assumption that only free electrons contribute is not valid.	130
4.4	Comparison of interferograms obtained 3.2 ns after the peak of the heating laser pulse for Al, Ti and Pd targets. All the interferograms were created using the same heating conditions as the one used to create the Al interferogram sequence in Fig. 4.2. The striking difference in behavior is most noticeable in the circled area.	132
4.5	Scattering factor f_1^0 for the neutral atoms of the elements with atomic number ranging from 1 to 86. aluminum is the only in the region with $Z < 50$ that has $f_1^0 < 1$	133
4.6	Sequence of simulated electron density contours and mean ionization distribution maps computed using the LASNEX code for an Al plasma created with the irradiation conditions of Fig. 4.2.	137
4.7	Synthesized interferograms computed using the calculated electron and ion densities from Fig. 4.6 and the calculated scattering factors for Al ions. The red lines indicate the position of the reference fringes.	138
4.8	Optical constant f_1^0 versus photon energy for various neutral materials. These values are an extrapolation of the Henke tables to lower energy.	144
4.9	Experimental setup showing the Diffraction Grating Interferometer and detailed schematic of the $500 \mu\text{m} \times 1000 \mu\text{m}$ semi-cylindrical targets used.	145

4.10	Soft x-ray interferograms corresponding to three times during the evolution of Sn plasmas generated by illuminating a 500 μm diameter Sn semi-cylindrical groove with a $\sim 1.3 \times 10^{12} \text{ W cm}^{-2}$, 800 nm, 120 ps laser beam. The early shot (4.5 ns from the heating beam) shows a plasma for which the fringes shift to the right, while the later frame (33 ns) shows fringes that bend to the left of the reference line (drawn), an indication of an index of refraction greater than one.	148
4.11	Optical constant f_1^0 versus photon energy calculated directly for SnIII (dotted line) and by the average atom code (solid line) for a Sn plasma with an ion density of 10^{20} cm^{-3} , a temperature of 4 eV, and $\bar{Z} = 1.98$.	150
4.12	Soft x-ray interferograms of a Silver plasma, the experimental conditions are the same as those used to obtain the interferograms in figure 4.10. Anomalous fringe shifts are clearly observed in the late stages of the evolution. The black line in the 31 ns frame represents the position of the reference fringes.	151
4.13	Optical constant f_1^0 versus photon energy calculated by the average atom code for a Ag plasma with an ion density of 10^{20} cm^{-3} , a temperature of 4 eV, and $\bar{Z} = 2.08$.	152
4.14	Soft X-ray interferograms taken at 5 and 15 ns in the evolution of a Carbon plasma created inside a 500 μm diameter semi-cylindrical groove with an irradiance of $\sim 1 \times 10^{12} \text{ Wcm}^{-2}$ was formed at the target plane, using the same setup as described above.	154
4.15	Number of fringe shifts computed from the interferograms in Fig. 4.14.	155
4.16	Index of refraction for Carbon plasmas computed using the Average Atom code. The plasma used had a density of 10^{20} cm^{-3} . A value of $(\eta - 1)/(\eta_{free} - 1)$ of 1 indicates that the contribution is solely due to free electrons.	156
4.17	Complete sequence of interferograms of Carbon plasmas created inside a 500 μm diameter semicylindrical groove. The white contours indicate the region in the plasma where the mean ionization is higher than 3. These contours were created using simulation results from the HYDRA code.	158
4.18	Complete sequence of density maps obtained from the interferograms in Fig. 4.17. The white contours indicate the region in the plasma where the mean ionization is higher than 3. Outside these contours unrealistic negative electron density values were measured.	159
4.19	Soft x-ray interferometry data similar to that in Figures 4.10 and 4.12 showing that for the case of copper no anomalous fringe shifts are observed.	161

4.20	Index of refraction for copper plasmas computed using the Average Atom code. The plasma used had a density of 10^{20} cm^{-3} . A value of $(1 - \eta)/(1 - \eta_{free})$ of 1 indicates that the contribution is solely due to free electrons.	162
4.21	Average atom calculation of an aluminum plasma with a density of 10^{20} cm^{-3} . A value of $(1 - \eta)/(1 - \eta_{free})$ of 1 indicates that the contribution is solely due to free electrons.	163

Chapter 1

INTRODUCTION

Interferometry has been used for more than one hundred years to measure both fundamental optical constants and properties of materials. In 1887 Michelson and Morley used what was later known as a Michelson interferometer to try to measure the relative speed between the earth and the “luminiferous ether” [1.1]. This was the first strong experimental evidence against the ether theory that led to it being abandoned. In 1891 and 1892, Zehnder and Mach separately described what has become known as the Mach–Zehnder interferometer. It was used to measure changes in refractive index, and hence density, in compressible gas flows [1.2, 1.3]. Since then, interferometry has been used in many applications that include metrology, astronomy and plasma physics. In particular, interferometry can be used to directly produce two-dimensional maps of the electron density in large scale plasmas. For example, interferometry is a diagnostic technique routinely used in Tokamak research to monitor the slow varying fusion plasmas [1.4]. Time-resolved laser interferometry of fast evolving plasmas can help in the understanding of plasma dynamics and can be used to validate and improve numerical plasma codes. The study of plasmas using optical interferometry has produced many results relevant to many plasma phenomena, like profile steepening [1.5], filamentation [1.6], the diagnostic of exploding foils for the production of soft x-ray lasers [1.7] and more. However, refraction of the probe beam, free–free absorption, and the limited number of fringe shifts that can be detected limit the maximum electron density, plasma size, and plasma density gradient that can be probed with optical lasers [1.8]. Since all of these limitations are significantly reduced by using shorter wavelength probe beams, the extension of plasma interferometry to soft x-ray wavelengths can significantly expand the maximum plasma densities and sizes that can be probed.

The development of gain-saturated soft x-ray lasers opened the possibility of extending laser interferometry to a significantly broader range of plasma pa-

rameters. The first soft x-ray interferometry experiments were performed using a 15.5 nm Ne-like Y laser pumped by the NOVA laser, conducted at Lawrence Livermore National Laboratory. The experiments used a skewed Mach Zehnder interferometer based on thin strained multilayer films to split and recombine the beam. Da Silva *et al.* successfully probed dense large scale laser-created plasmas as close as 25 μm from the target surface and electron densities up to 10^{21} cm^{-3} [1.8], and also studied the collision and subsequent interaction of counterstreaming high-density plasmas [1.9]. Subsequent experiments were conducted at Colorado State University utilizing a greatly more compact capillary discharge laser emitting at 46.9 nm combined with a Lloyd's mirror interferometer [1.10]. This and other gain-saturated tabletop soft x-ray lasers created the opportunity to develop portable soft x-ray tools that allow mapping in detail the evolution of the electron density distribution in a great variety of dense plasmas.

This dissertation presents results of newly observed phenomena in dense plasmas resulting from soft x-ray laser interferometry experiments. The interferograms unveiled two dimensional dynamics in laser-created plasmas as well as a result of fundamental significance: the importance of the contribution of bound electrons to the index of refraction of plasmas.

The interferometer used is the first amplitude division interferometer designed to work in combination with a table top soft x-ray laser. The interferometer avoids the use of the delicate multilayer thin film beam splitters, used in the Da Silva *et al.* experiments, by using instead specially tailored diffraction gratings to split and recombine the probe beam. The use of diffraction gratings makes the interferometer robust, stable and scalable to different soft x-ray wavelengths, in particular to 46.9 nm, where thin film beam splitters cannot be manufactured because of the

lack of materials with adequate optical constants. A second interferometer was designed to work together with a 14.7 nm wavelength picosecond soft x-ray laser. These two interferometer setups have been extensively used to produce many results in plasma diagnostics, and they clearly show the advantages of performing plasma interferometry at soft x-ray wavelengths.

This chapter discusses the motivation for the study of dense plasmas, followed by a brief review of some of the plasma diagnostic tools available and a discussion of the index of refraction of plasmas. The chapter concludes by describing the two soft x-ray lasers used in the plasma diagnostic experiments presented in the following chapters.

Chapter 2 first discusses the advantages of reducing the probe wavelength in plasma interferometry. Subsequently the Diffraction Grating Interferometer used in the experiments is described, including the alignment procedure, the detection system and the advantages of combining the interferometer with a picosecond probe beam.

Chapter 3 presents the study of the formation of a central density depression and surrounding side lobes in laser-created plasmas. This two dimensional effect is shown to be produced by radiation induced ablation of target material outside of the focal region of the plasma-heating laser. A subsequent pressure balance between the colder sidelobe material and the hotter central region results in the observed on-axis density depression. The effect should be general, and be present in many plasmas under many irradiation conditions. This effect was understood thanks to the feedback between the experimental data and hydrodynamic simulations, that were also validated as part of this study.

In Chapter 4 the contribution of bound electrons to the index of refraction in multiply ionized plasmas is discussed. It has been generally accepted that the index

of refraction is given only by the free electrons in the plasma. This assumption has been widely used in the analysis of plasma diagnostics experiments, including all soft x-ray laser plasma diagnostics to date. However, at soft x-ray wavelengths, the presence of absorption lines and edges makes the contribution of the bound electrons in ions significant. This results in the experimental observation of fringes bending in the opposite direction than expected when the index of refraction is given only by free electrons. A combination of hydrodynamic simulations with atomic calculations was used to understand the experimental data obtained by probing aluminum plasmas at 14.7 nm. Also, the effect was predicted and shown experimentally to be present at other wavelengths and in plasmas created using other materials. The significance of this result goes beyond interferometry, as the index of refraction is used in calculations of the self-generated plasma radiation and it can significantly affect the results.

1.1 Studies of plasmas

Plasmas are a collection of neutral and charged particles that exhibit a collective behavior. Plasmas carry electrical currents producing magnetic fields that, together with the electric fields, interact with the charged particles. Out of all matter in the visible universe, 99 % of it is in some sort of plasma state. Plasmas can exist in a parameter space that spans many orders of magnitude in scale, density and temperature. The parameter space covers values that go from interplanetary space plasmas that are very diffuse ($\sim 10^{-3}$ particles cm^{-3}) and cold ($\sim 10^2$ K) to the interior of stars with densities that exceed $\sim 10^{27}$ particles cm^{-3} and temperatures of $\sim 10^7$ K and from sub micrometer-size plasmas (10^{-7} m), studied in the laboratory to large scale space plasmas (10^7 m). The behavior of small and large

scale plasmas can be similar, for example, large scale space plasmas can be studied using equivalent small scale laboratory models by matching dimensionless numbers that characterize the plasma.

Plasmas are used in a large number of applications in industry and science. The website *www.plasmas.org* lists nearly one hundred different main applications in many fields that include plasmas being used in thin film deposition, in plasma-based lighting systems and displays, in materials synthesis and more. Plasmas are very good emitters of electromagnetic radiation, this includes light in the extreme ultraviolet spectral region. Therefore plasmas can, for example, be used to generate the 13.5 nm wavelength light to be used for lithography in the printing of the new generation of computer processors with a 38 nm structure size and below [1.11, 1.12]. A particular plasma application that would have a very wide impact in everyday life, is the generation of energy through thermo-nuclear fusion reaction in plasmas. Fusion, which only occurs naturally in the interior of stars, is being pursued in laboratories using different approaches. Magnetic and inertial confinement fusion both use plasmas in different regimes. In the case of indirect drive inertial confinement fusion, laser-created plasmas are used to generate the radiation that heats and compresses the fusion fuel [1.13].

The study of plasmas involves many different fields in physics. The motion of large collections of particles are described with statistical mechanics. Atomic physics is needed to describe the atoms in the plasma and their interaction with free electrons and collective fields, which in turn, are described by electro-magnetic theory. Special relativity has to be used in the case of very hot plasmas where electron speeds near the speed of light.

To completely describe a plasma, the position and velocities of all particles would have to be known. This information can then be used to calculate the

fields and with the field, the forces that can be used to compute the next step in the plasma evolution. The very large number of particles typically forming the plasma ($10^{15} - 10^{20}$) prohibits this treatment. The particle in cell technique does this but with a reduced number of “super” particles, selected to represent the plasma behavior [1.14]. However, in many cases many of the plasma characteristics can be described treating them as fluids with the field equations coupled into the fluid motion equations. Statistical parameters that average over many particles are useful to describe the plasma behavior. Some of the most important plasma parameters are electron and ion density, electron and ion temperatures, and mean ionization.

1.1.1 Laser-created plasmas

The plasmas studied in this work were all created by heating solid targets with intense optical laser light. The first stage in the plasma formation process is the heating of the material by the absorption of the incident light. In the case of metals, which is what was used as target material in most of the experiments, the heating process starts with the electrons in the conduction band of the metal absorbing some of the incident light and being excited to a higher energy level. As the electrons collide with the atoms in the material they transfer some of the energy to the bulk material that heats up in the regions close to the surface. This process continues until the temperature reaches the melting point of the material and a significant number of atoms expand into vacuum. The absorption of light increases for some materials at this stage, which results in a short transition to the evaporation stage. The temperature of the vapor will rise as long as the laser is depositing enough energy to overcome the cooling by expansion and conduction. When the vapor reaches sufficiently high temperatures a significant number

of atoms will be ionized by collisions. Now, with free electrons available in the plasma, the dominant heating process becomes inverse bremsstrahlung. This process involves free-free transitions of electrons in collision with positive ions. With an increase in the density of free electrons and ions, the process becomes stronger, so the plasma is heated up even more and more free electrons are created, until eventually a saturation is reached. When short and intense laser pulses are used to create the plasma, all the surface atoms in the focal spot are ionized very rapidly, creating a shallow plasma with solid densities. In many plasma simulations this shallow and dense plasma is the starting point for the calculation with inverse bremsstrahlung as the main laser deposition mechanism. The typical plasma density profile resulting from this process is an exponential decay with distance away from the target surface, and with a scale length increasing with time [1.15]. Once the heating pulse is over, the plasma will only expand and cool down, redistributing the energy through heat and radiation transport mechanisms. The plasmas created by lasers irradiating solid materials are usually hot (from a few eV to keV), dense (can reach and even surpass solid densities), relatively small in size (from μm to mm scale lengths), and with a very short life, usually on the order of tens of ns. These characteristics make laser-created plasmas challenging to diagnose. Some of the techniques used in the diagnostic of these type of plasmas are reviewed in the next section.

1.1.2 Magneto-hydrodynamic computer codes

Two computer codes were used in this work to simulate the experiments and to compare the results with the experimental results, aiding in the understanding of the physical phenomena in the plasma measured with the interferometer. The codes, LASNEX and HYDRA, were developed to help in the design of inertial

confinement fusion (ICF) experiments and to help analyze the results from these ICF experiments. They have been developed for many decades and are complex codes that include all the main physical processes that occur in plasmas. The code LASNEX was developed starting in 1972 [1.16], and the code HYDRA in 1993 [1.17]. The codes are versatile and permit the users to apply them to model physical problems that were not the ones originally intended by the authors.

Both LASNEX and HYDRA are hydrodynamic codes that treat the plasma as a fluid, governed by the fluid equations of motion. They also contain an “atomic model” in which both collisions and radiation are used to compute the population distributions. Treating the plasma as a fluid means that the motion of a large number of individual particles is described collectively, and it assumes that the plasma is dense enough for an infinitesimally small fluid element to still contain enough particles to be possible to specify in it a mean velocity and kinetic energy. In a plasma, the fluid equations of motion are coupled to the Maxwell equations that describe the fields in the plasma.

The codes divide the problem in cells that form a mesh that can be tailored in shape to match the specific geometries being studied. The mesh can either be let to evolve following the plasma motion, with each cell keeping a constant mass (Lagrangian scheme), or it can be a static container that divides the calculation and through which the mass flows (Eulerian scheme). The Lagrangian scheme is widely used because it provides an advantage in the case of an expanding plasma, where the spatial extension of the plasma can be large but where the region of interest can be small. This can reduce the number of computations required as a fine grid can be used just in the regions that need it. LASNEX is essentially a Lagrangian code, while HYDRA works in what is known as an Arbitrary Lagrangian Eulerian (ALE)

mode and can switch from being fully Lagrangian to permit some of the mass to advect from the cells. The ALE technique is useful to prevent mesh distortion present in the Lagrangian scheme, and is commonly used to simulate converging plasma geometries as those utilized in ICF.

The codes include different packages that can treat all the main physical processes that occur in the plasma. The different packages can be turned on and off to suit the particular experimental conditions. They can simulate, among others, the radiation generation and transport in the plasma, the thermal and electrical conductions of the electrons and ions and calculate the magnetic fields present in the plasmas. The atomic physics models provide the equation of state variables, for example the pressure and energy as a function of the temperatures and density, that are used in the hydrodynamic calculations. They also provide the different collisional rates that are needed to calculate the degree of ionization and the wavelength dependent opacities that are used to compute the transport of radiation. Different separate codes or tables that facilitate this calculation are available (*e.g.* the Lawrence Livermore National Laboratory Equation of State data, LEOS). Also, there are packages that can be used to drive the simulations with different sources like lasers and ion beams, and to calculate the propagation of light in the plasmas. Another difference between the two codes is that LASNEX is limited to two-dimensional cylindrical geometries while HYDRA is a fully three-dimensional code. The limitation of the cylindrical geometry is usually avoided by working far from the z -axis, where planar geometries can be approximated. Another practical difference is that HYDRA is an export controlled but non-classified code while LASNEX remains classified due to its ability to simulate thermo-nuclear reactions.

The LASNEX simulation results presented in this work were obtained by Steve Moon from Lawrence Livermore National Laboratory and the HYDRA simulation results were obtained by Mike Purvis from Colorado State University.

1.2 Diagnostics techniques for laser-created plasmas

There are many techniques that can be used to study and diagnose plasmas, and they vary according to the duration, density and temperature of the plasma studied. The short time scale and small dimensions of laser-created plasmas limit the type of diagnostic tools that can be used. Many of the techniques are complementary as they provide information on different and independent parameters of the plasma. The diagnostic techniques can be classified in many ways, for example according to what parameter they measure, *e.g.* density, temperature or by the method used in the measurement, *e.g.* probing the plasma with light or collecting the light emitted by the plasma.

As mentioned above, plasmas are very good emitters of light. The wavelength distribution of the light emitted depends on the temperature and density of the plasma and on the elements forming the plasma. The plasma emission has two components, a continuum arising from the photons emitted in free-free and free-bound transitions, and line emission from the photons emitted in bound-bound transitions. The spectral distribution of the emission intensity has a near thermal continuum caused by the emission of photons by the accelerated electrons as they collide with the ions. The distribution of velocities of electrons in the plasma makes this process effectively random, producing a continuum spectrum that nearly follows the plasma's thermal distribution. There is also a recombination continuum that gives rise to a continuum emission for photon energies larger than the ionization potential of the recombining ion, characterized by edges or steps in the

spectrum. The line emission from the plasma is formed by the discrete electron transitions in the elements as electrons recombine and rearrange themselves in the atoms and can give information on the state of ionization, temperature and density of the plasma. In spectroscopy, the spectrum of the light emitted by the plasma is studied. A spectrometer can be operated in a time integrated mode or it can be gated to obtain a time resolved spectrum. For very high time resolution (*e.g.* picosecond) it is possible to combine a streak camera with a spectrometer but in detriment of the amount of light collected. Also, if the plasma is imaged, spectrograms with spatial resolution can be obtained in one dimension of the plasma. The light emitted from a plasma can also be imaged to obtain a map of the intensity of the light emitted. In general, hotter and denser regions in the plasma will emit more radiation and so result in brighter regions of the image. Different types of detectors/filter combinations can be used to acquire the images in this qualitative technique. Some of these are MCP (multi channel plate) detectors, back-thinned CCD (coupled charge device), both sensitive to the short wavelengths emitted by plasmas, and regular CCD cameras sensitive to visible light.

1.2.1 Temperature measurement

There are several ways of measuring the plasma temperatures using spectroscopy. For example the ion temperature can be obtained by measuring the line shape of the plasma emission. The line width can be dominated by Doppler broadening, which arises from the relative velocity of the emitting atoms to the observer. The line width is proportional to $\sqrt{T_i/m_i}$, where T_i is the ion temperature of the moving ions and m_i is the mass of the ion. The electron temperature, T_e , can be inferred from the continuum radiation, since for $h\nu \geq T_e$, the emission from both free-free and free-bound transitions has an exponential dependence with the

electron temperature [1.18]. It is also possible to measure the electron temperature of a plasma by using the ratios of line emissions. Some of these techniques require modeling and knowledge of the rate coefficients so there is a significant uncertainty in these measurements, which can rise up to 30 %.

1.2.2 Density measurement

Spectroscopy can also be used to measure the electron density of plasmas that are relatively cold and dense. Stark broadening dominates the line shape in those cases: the surrounding electric field produces a broadening of the line that is proportional to the electron density of the plasma. If the absolute line intensities are measured, the density of an atomic species can be obtained if the transition rates, A_{ij} , are known. [1.19].

Some plasma density diagnostic methods take advantage of the effect that the plasma has on light that traverses it. The scattering of radiation by the electrons can be used to measure the electron density of plasmas. The scattered power P_s per unit length of a laser beam of power P_0 in a plasma of electron density n_e is given approximately by:

$$P_s = P_0 \sigma_T n_e, \quad (1.1)$$

where σ_T is the Thomson scattering cross section. The scattering cross section is given by $\sigma_T = \frac{8\pi r_e^2}{3} = 6.65 \times 10^{-33} \text{ cm}^2$. Where the classical electron radius is given by $r_e = \frac{e^2}{4\pi\epsilon_0 mc^2}$. Since this cross section is extremely small, the technique is difficult to implement. A narrow wavelength and a short pulse duration can help to discriminate against the background radiation emitted from the plasma. If the beam size is not smaller than the scale of the density variation of the plasma, only an average of the density will be measured. Thomson scattering has been used in

the diagnostics of large scale and dense plasmas, where the number of scattered photons is sufficiently large.

Shadowgraphy is a simple method that can be used to obtain qualitative information on the density of plasmas. An image of a probe beam is obtained after it traverses a plasma and is partially absorbed by it. The attenuation of the probe beam will depend on the density and ionization of the plasma, but the extraction of a value of the density would require knowledge of the absorption process and cross sections. In general the technique is used to backlight the plasma and diagnose features like uniformity and velocity of expansion as is the case in many z -pinch experiments [1.20].

A more experimentally complex but more powerful plasma diagnostic method is refractometry. It is used to measure the electron density of plasmas by measuring the deflection of a probe beam as it travels through a plasma. The refraction of the beam is caused by the change in the index of refraction of the plasma due to gradients in the electron density. In some cases and with some plasma geometries it is possible to reconstruct the density profile from the deflected wavefront of the probe beam [1.21]. This generally requires complex calculations and symmetry assumptions of the plasma that make this an indirect measurement.

A still more experimentally elaborate but more powerful method is interferometry. It measures the electron density of a plasma by measuring the phase delay of a probe beam as it travels through the plasma. This technique, that is discussed in greater detail in the next chapter, can produce electron density information without the need to rely on modeling or extensive calculations. Under the assumption of a uniform plasma along the direction of propagation of the probe beam, interferometry provides a direct measurement of the electron density. This

is done by assuming that the index of refraction of the plasma is given by

$$\eta = \sqrt{1 - \frac{n_e}{n_c}}, \quad (1.2)$$

where n_c is the critical density of the plasma, discussed in the next section, and n_e is the electron density. This expression, that is also used in refractometry, only considers the contribution of the free electrons but, as it is shown experimentally in this work, is not always valid, and bound electrons in the plasma must be considered in some cases.

1.3 The index of refraction of a plasma

The index of refraction is a very important characteristic of a plasma that describes its interaction with light and that depends on the density of particles in the plasma. It affects the propagation of self generated plasma radiation as well as that of the probe beams that are often used in plasma characterization techniques that include interferometry and refractometry. The index of refraction of a plasma can be thought of as the effect of the interaction of the light in the plasma, with, for the general case, both the free and the bound electrons.

The index of refraction of a plasma is given by

$$\eta(\omega) = \frac{c}{v_\phi}, \quad (1.3)$$

where v_ϕ is the phase velocity of a wave propagating in the medium, and c is the speed of light in vacuum. The index of refraction gives the speed of the individual waves of different frequencies propagating in the plasma relative to the speed of light in vacuum. For soft x-ray wavelengths the speed of light in a plasma is very close to the speed of light in vacuum, c , so it is common to write the index as a

deviation from the value 1, in the following way:

$$\eta(\omega) = 1 - \delta + i\beta. \quad (1.4)$$

Where the real part of the index modifies the phase of the wave and the imaginary part, the amplitude. This can be seen by writing

$$\frac{\omega}{k} = \frac{c}{\eta} = \frac{c}{1 - \delta + i\beta}, \quad (1.5)$$

which results in a wave vector k ,

$$k = \frac{\omega}{c}(1 - \delta + i\beta). \quad (1.6)$$

This wave vector can be used in the expression for a plane wave,

$$E(\mathbf{r}, t) = E_0 \exp[-i(\omega t - \mathbf{k} \cdot \mathbf{r})], \quad (1.7)$$

to yield

$$E(\mathbf{r}, t) = E_0 e^{-i\omega(t-r/c)} \underbrace{e^{-i(2\pi\delta/\lambda)r}}_{\text{phase shift}} \underbrace{e^{-(2\pi\beta/\lambda)r}}_{\text{decay}}. \quad (1.8)$$

To calculate the index of refraction of a plasma, first only taking into account the contribution of free electrons, an electro magnetic wave will be considered as it travels through the plasma. Starting from the Maxwell equations applied to the free electrons in the plasma,

$$\nabla \times \mathbf{H} = \epsilon_0 \frac{\partial \mathbf{E}}{\partial t} - en_e \mathbf{v} \quad (1.9)$$

and

$$\nabla \times \mathbf{E} = -\mu_0 \frac{\partial \mathbf{H}}{\partial t} \quad (1.10)$$

where the term $-en_e \mathbf{v}$ accounts for the current of free electrons. Taking the curl of (1.10) and replacing the curl of H with (1.9), and then using the well known

vector identity $\nabla \times (\nabla \times \mathbf{A}) = \nabla(\nabla \cdot \mathbf{A}) - \nabla^2 \mathbf{A}$ the following wave equation is obtained after recognizing that for transverse waves $\nabla \cdot \mathbf{E} = 0$

$$-\nabla^2 \mathbf{E} = -\mu_0 \epsilon_0 \frac{\partial^2 \mathbf{E}}{\partial t^2} + \mu_0 e n_e \frac{\partial \mathbf{v}}{\partial t} \quad (1.11)$$

To account for the effect of the propagating electric field on the free electrons, a simple classical model can be used by applying Newton's law, $\mathbf{F} = m \cdot \mathbf{a}$, in this case,

$$m \frac{\partial \mathbf{v}}{\partial t} = -e(\mathbf{E} + \mathbf{v} \times \mathbf{B}). \quad (1.12)$$

The $\mathbf{v} \times \mathbf{B}$ term is small when compared with the \mathbf{E} term for non relativistic motion, as it contains a $\frac{v}{c}$ term, so it can be ignored for the case of non-relativistic motion. Then this expression can be used to replace the velocity term in (1.11). After rearranging the expression,

$$\frac{\partial^2 \mathbf{E}}{\partial t^2} + \frac{e n_e}{\epsilon_0} \left(\frac{e \mathbf{E}}{m} \right) - \frac{1}{\epsilon_0 \mu_0} \nabla^2 \mathbf{E} = 0, \quad (1.13)$$

and recognizing that $c^2 = \frac{1}{\epsilon_0 \mu_0}$ and defining the plasma frequency as $\omega_p^2 = \frac{e^2 n_e}{\epsilon_0 m}$, the transverse wave equation in a plasma is reached.

$$\left(\frac{\partial^2}{\partial t^2} + \omega_p^2 - c^2 \nabla^2 \right) \mathbf{E} = 0. \quad (1.14)$$

The dispersion relation is obtained by applying this wave equation to the case of a plane wave, expression (1.7),

$$\omega^2 = \omega_p^2 + k^2 c^2, \quad (1.15)$$

so

$$k = \frac{\sqrt{\omega^2 - \omega_p^2}}{c}. \quad (1.16)$$

This dispersion relation indicates that for frequencies below the critical frequency, ω_p , k will be imaginary and the wave will not propagate but instead decay exponentially with distance. For a particular frequency, the plasma electron density at which the wave cannot propagate is called the critical density and is given by

$$n_c = \frac{\epsilon_0 m \omega^2}{e^2} = \frac{\pi}{r_e \lambda^2} \quad (1.17)$$

Where r_e is the classical electron radius. To calculate the index of refraction the phase velocity is needed, that using (1.16) becomes

$$v_\phi = \frac{\omega}{k} = c \sqrt{\frac{\omega^2}{\omega^2 - \omega_p^2}} = \frac{c}{\sqrt{1 - \frac{\omega_p^2}{\omega^2}}}$$

yielding

$$\eta(\omega) = \frac{c}{v_\phi} = \sqrt{1 - \frac{\omega_p^2}{\omega^2}}, \quad (1.18)$$

which can be written in terms of the electron density by replacing ω_p by its definition, and writing the resulting expression in terms of the critical plasma electron density defined above

$$\eta = \sqrt{1 - \frac{n_e}{n_c}} \quad (1.19)$$

This last equation expresses that a wave will be able to propagate through a plasma as long as the density of the plasma is lower than the critical density. It also shows that the index of refraction due to free electrons, for a wave propagating in a plasma, is always less than one. The expression (1.19) is the one commonly used to compute the index of refraction of multiply ionized plasmas.

The problem now is how to calculate the index of refraction including the effect of the bound electrons. The procedure is similar to what was done above but now the presence of the bound electrons will be taken into account by including source terms due to the induced current and the charge. Then a new wave equation

will be obtained, and the factor in front of the ∇^2 term will be identified as the speed factor of the wave, or the index of refraction of the medium. Many authors have discussed the problem of calculating the index of refraction in a plasma, the treatment discussed by Attwood [1.22] is followed here.

Starting with Faraday's law and taking the curl on both terms

$$\nabla \times (\nabla \times \mathbf{E}) = \nabla \times \left(-\frac{\partial \mathbf{B}}{\partial t} \right)$$

and using the vector identity $\nabla \times \nabla \times \mathbf{A} = \nabla(\nabla \cdot \mathbf{A}) - \nabla^2 \mathbf{A}$, the following expression is obtained

$$\nabla(\nabla \cdot \mathbf{E}) - \nabla^2 \mathbf{E} = -\mu_0 \frac{\partial}{\partial t} (\nabla \times \mathbf{H}).$$

This expression, after using Coulomb's ($\nabla \cdot \mathbf{E} = \frac{\rho}{\epsilon_0}$) and Ampere's ($\nabla \times \mathbf{H} = \frac{\partial \mathbf{D}}{\partial t} + \mathbf{J}$) laws, becomes

$$\nabla \left(\frac{\rho}{\epsilon_0} \right) - \nabla^2 \mathbf{E} = -\mu_0 \frac{\partial}{\partial t} \left(\frac{\partial \mathbf{D}}{\partial t} + \mathbf{J} \right),$$

that can also be written as

$$\nabla \left(\frac{\rho}{\epsilon_0} \right) - \nabla^2 \mathbf{E} = -\epsilon_0 \mu_0 \frac{\partial}{\partial t} \left(\frac{\partial \mathbf{E}}{\partial t} + \frac{\mathbf{J}}{\epsilon_0} \right).$$

Now, after rearranging the terms, the expression is recognized as the wave equation

$$\left(\frac{\partial^2}{\partial t^2} - c^2 \nabla^2 \right) \mathbf{E}(\mathbf{r}, t) = -\frac{1}{\epsilon_0} \left[\frac{\partial \mathbf{J}(\mathbf{r}, t)}{\partial t} + c^2 \nabla \rho(\mathbf{r}, t) \right] \quad (1.20)$$

where $(\epsilon_0 \mu_0)^{-1/2}$ is recognized as the speed of light in vacuum, c

$$c \equiv \frac{1}{\sqrt{\epsilon_0 \mu_0}}$$

It can be shown that when considering the propagation of transverse waves, the density term, $\nabla \rho$, can be combined with the current term, $\frac{\partial \mathbf{J}}{\partial t}$, by using the

continuity equation. The result is that only the transverse current contributions need to be taken into account,

$$\left(\frac{\partial^2}{\partial t^2} - c^2 \nabla^2\right) \mathbf{E}_T(\mathbf{r}, t) = \frac{-1}{\epsilon_0} \frac{\partial \mathbf{J}_T(\mathbf{r}, t)}{\partial t}. \quad (1.21)$$

Here, the subscript T indicates that it is the component transverse to the propagation direction \mathbf{k} . A simple semi-classical model can be used to calculate \mathbf{J}_T . In this model the passing electromagnetic wave induces a motion on the bound electrons in the atom. The model assumes that electrons are bound to the atom through a central field restoring force. The equation of motion ($F = m \cdot a$) can be written as follows

$$m \frac{d^2 \mathbf{x}}{dt^2} + m\gamma \frac{d\mathbf{x}}{dt} + mw_s^2 \mathbf{x} = -e(\mathbf{E} + \mathbf{v} \times \mathbf{B})$$

where the first term is the acceleration of the particle and the second, a dissipative force term that restores the electrons to their unperturbed state. The third term contains a restoring force corresponding to an oscillator of frequency w_s . The force term in the equation of motion is given by the Lorentz force due to the incident electro-magnetic field acting on a charged electron. The magnetic field can be ignored for the case of non-relativistic electrons, as was done before for the free electrons case (1.12). If the displacement is assumed to follow the time dependence of the incident electric field ($\mathbf{E} = \mathbf{E}e^{-i\omega t}$), the time derivatives contribute a $-i\omega$ factor and the equation of motion that, after cancelling the common exponential term, becomes

$$m(-i\omega)^2 \mathbf{x} + m\gamma(-i\omega) \mathbf{x} + mw_s^2 \mathbf{x} = -e\mathbf{E},$$

solving for the displacement vector $\mathbf{x}(\mathbf{r}, t)$

$$\mathbf{x}(\mathbf{r}, t) = \frac{e}{m} \frac{1}{(\omega^2 - w_s^2) + i\gamma\omega} \mathbf{E}(\mathbf{r}, t).$$

With this, the induced velocity of the electron can be calculated

$$\mathbf{v}(\mathbf{r}, t) = \frac{e}{m} \frac{1}{(w^2 - w_s^2) + i\gamma w} \frac{\partial \mathbf{E}(\mathbf{r}, t)}{\partial t}$$

Now, the current due to one electron would be $\mathbf{J} = -e\mathbf{v}$. But what is needed is the current induced in a group of many atoms, each containing many bound electrons. This is a very complicated problem to solve, since, to do it for the general case, it is necessary to take into account the relative position of each electron and each atom. But, it can be shown that if one is only interested in the forward scattering, that is, the scattered wave is in the same direction as the incident wave, then the relative positions of the electrons in the atom don't matter as all of them contribute with the same phase. This is indicated by the subindex 0 in the expressions. The current is then given by a sum over similar resonances

$$\mathbf{J}_0(\mathbf{r}, t) = -en_a \sum_{s=1}^Z g_s \mathbf{v}_s(\mathbf{r}, t). \quad (1.22)$$

Here n_a is the average density of atoms, and g_s is the oscillator strength for the electron with resonance frequency w_s . Semiclassically this indicates the number of electrons that have a resonant frequency w_s , so the sum of the oscillator strengths

$$\sum_s g_s = Z \quad (1.23)$$

has to be equal to the number of electrons in the atom. The oscillator strengths in the semiclassical model are empirical quantities but in the quantum mechanical treatment the oscillator strengths are the transition probabilities between stationary states of the atom. The total current is then

$$\mathbf{J}_0(\mathbf{r}, t) = -\frac{e^2 n_a}{m} \sum_s \frac{g_s}{(w^2 - w_s^2) + i\gamma_s w} \frac{\partial \mathbf{E}(\mathbf{r}, t)}{\partial t}. \quad (1.24)$$

Now, using (1.24) as the source terms for the transverse wave equation (1.21) the following is obtained

$$\left(\frac{\partial^2}{\partial t^2} - c^2 \nabla^2\right) \mathbf{E}_T(\mathbf{r}, t) = \frac{e^2 n_a}{\epsilon_0 m} \sum_s \frac{g_s}{(w^2 - w_s^2) + i\gamma_s w} \frac{\partial^2 \mathbf{E}_T(\mathbf{r}, t)}{\partial t^2}. \quad (1.25)$$

This last expression can be rewritten in a more familiar way by collecting the terms with the same operator

$$\left(\frac{\partial^2}{\partial t^2} - \frac{c^2}{\eta^2(w)} \nabla^2\right) \mathbf{E}_T(\mathbf{r}, t) = 0,$$

where the index of refraction η is given by

$$\eta(w) \equiv \left[1 - \frac{e^2 n_a}{\epsilon_0 m} \sum_s \frac{g_s}{(w^2 - w_s^2) + i\gamma_s w}\right]^{1/2}. \quad (1.26)$$

Using that $w = \frac{2\pi c}{\lambda}$ the equation can be written as

$$\eta(w) = \left[1 - \frac{e^2 n_a \lambda^2}{\epsilon_0 m 4\pi^2 c^2} \sum_s \frac{g_s w^2}{(w^2 - w_s^2) + i\gamma_s w}\right]^{1/2},$$

now, the classical electron radius r_e can be used to group the factors in front of the sum

$$\eta(w) = \left[1 - \frac{r_e n_a \lambda^2}{\pi} \sum_s \frac{g_s w^2}{(w^2 - w_s^2) + i\gamma_s w}\right]^{1/2}.$$

Finally, realizing that the critical density of a plasma can be written as $n_c = \frac{\pi}{r_e \lambda^2}$, the index of refraction of a plasma due to the bound electrons in the atoms is given by

$$\eta(w) = \left[1 - \frac{n_a}{n_c} \sum_s \frac{g_s w^2}{(w^2 - w_s^2) + i\gamma_s w}\right]^{1/2}. \quad (1.27)$$

From this equation it can be noted that the index of refraction has a strong dependence on the frequency, ω , in particular near the resonances, w_s . Figure 1.1 shows a sketch of the behavior of the real and imaginary parts of the index of refraction, computed using expression (1.27) with arbitrary resonances as an illustration. The

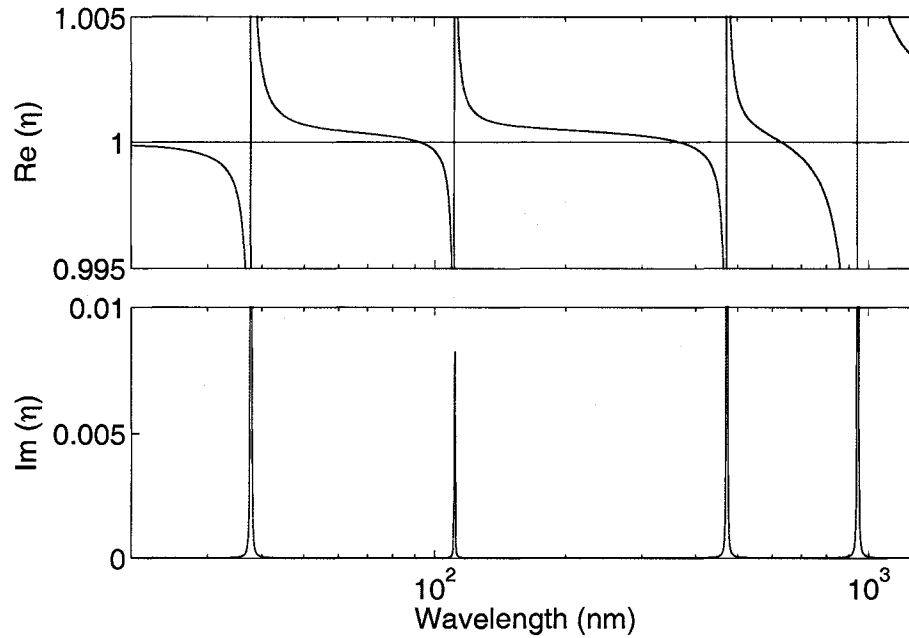


Figure 1.1: Real and imaginary parts of the index of refraction for a material showing resonances in the visible, ultraviolet and EUV regions of the spectrum.

strong variations near infrared, ultraviolet and extreme ultraviolet are observed, with a corresponding peak in absorption shown in the imaginary part of the index. The tendency is for the index to converge toward unity as the wavelength is reduced, as the frequency of the light becomes larger than most of the atomic resonances.

In the case of a plasma dominated by ions, where the weakest bound electrons have already been removed, the frequency of infrared and visible light is smaller than most resonances. In other words, the electrons are bound too tightly to the atoms for the light to affect them, and only the free electrons contribute to the index of refraction. For hard x-rays the frequency is higher (the photons are more energetic) than even the most tightly bound electrons, then all the electrons will act as free electrons to the field. The regime in between those two, where soft x-ray and EUV lies, can present the case where the bound electrons in ions contribute

as much as the free electrons in the plasma. This is the situation relevant to the experiments discussed in Chapter 4.

When expression (1.27) is used for the case of ions, the contribution to the index from the free electrons corresponding to those ions can be considered by realizing that since free electrons are not bound they have no associated resonance or damping constant. The part of the sum corresponding to the free electrons reduces to $\sum_s g_s = Z_{free}$, the number of free electrons that result from the difference between the atom's nuclear charge and the ionization stage of the atom. In the case of a plasma where each ion is fully ionized, the index of refraction is

$$\eta(w) = \left(1 - \frac{n_a Z}{n_c}\right)^{1/2}$$

and since $n_a Z$ is the number of free electrons n_e ,

$$\eta(w) = \left(1 - \frac{n_e}{n_c}\right)^{1/2},$$

then, the expression for the index of refraction obtained assuming only free electrons is recovered (1.19).

From (1.27), a complex scattering factor can be defined as

$$f^0(w) = \sum_s \frac{g_s \omega^2}{(\omega^2 - \omega_s^2) + i\gamma_s w}.$$

The scattering factor is the factor by which one needs to multiply the free electron scatter amplitude to get the total atomic scatter amplitude. It is usually written explicitly in terms of its real and imaginary parts

$$f^0(w) = f_1^0 - i f_2^0. \quad (1.28)$$

The index of refraction can then be written as follows,

$$\eta(w) = \left[1 - \frac{n_a}{n_c} (f_1^0 - i f_2^0)\right]^{1/2}. \quad (1.29)$$

The factor $\frac{n_a}{n_c}$ in (1.29) is usually very small for the experimental conditions that are normally encountered in the lab and especially for short wavelengths where n_c is of the order of solid densities or higher. In those cases the square root in the expression for the index can be approximated using $\sqrt{1 - \delta} \simeq 1 - \frac{\delta}{2}$. Then

$$\eta(\omega) \simeq 1 - \frac{n_a}{2n_c} [f_1^0 - i f_2^0] \quad (1.30)$$

and then, comparing expressions (1.4) and (1.29) yields expressions for δ and β in terms of the scattering factors,

$$\delta = \frac{n_a}{2n_c} f_1^0(\omega) \quad (1.31)$$

and

$$\beta = \frac{n_a}{2n_c} f_2^0(\omega). \quad (1.32)$$

So, in this way f_1^0 is associated with the change in phase of the wave as it propagates in a medium and f_2^0 is associated with the change in amplitude. Furthermore, the real and imaginary parts of the scattering factor are not independent of each other but are linked through the Kramers-Kronig relation [1.23]. Applied for the case of the scattering factors, it takes the following form:

$$f_1^0(\omega) = Z - \frac{2}{\pi} P.V. \int_0^\infty \frac{u f_2^0(u)}{u^2 - \omega^2} du \quad (1.33)$$

and

$$f_2^0(\omega) = \frac{2\omega}{\pi} P.V. \int_0^\infty \frac{f_1^0(u) - Z}{u^2 - \omega^2} du, \quad (1.34)$$

where Z is the number of electrons per atom and $P.V.$ indicates a principal value integral. Thanks to the Kramers-Kronig relation it is possible to obtain f_2^0 from absorption measurements and through the relation calculate f_1^0 performing an

integration for each ω . This is very convenient because it is easier to measure the amplitude of a wave than the phase. This was extensively done to produce the Henke tables [1.24] that are available from Lawrence Berkeley National Laboratory (www.cxro.lbl.gov), which tabulate the values of the optical constants f_1^0 and f_2^0 for neutral materials, for light in the energy range of 10 eV (30 for f_1^0) to 30 KeV. The problem of calculating the index of refraction of the plasma is thus translated into the problem of calculating (or measuring) the imaginary part (absorption) of the plasma and then using the Kramers-Kronig relation to convert it to the real part.

1.4 Soft X-Ray Lasers

In this work two lasers operating at 14.7 nm and 46.9 nm were combined with an amplitude division interferometer to probe large scale, high density plasmas. The wavelength region where these lasers operate is usually named in different ways depending on the history of each particular field. Soft x-rays, the chosen name in this work, and Extreme Ultra Violet (EUV) are frequently used. There is particular interest in the development of table-top lasers sources that can operate in the soft x-ray region of the spectrum. These coherent and bright sources can be used for many applications that include very high resolution metrology, studies in atomic physics, photochemistry and photophysics, biological imaging, and large scale, very high density plasmas diagnostics.

The first collisional soft x-ray laser was produced in a plasma created by NOVA, the fusion class laser at Lawrence Livermore National Laboratory. The optical laser completely ablated a selenium foil target and produced a spectrum with clear evidence of amplified emission at $\lambda= 20.6$ and 20.9 nm [1.25]. Simultaneously, amplification at $\lambda=18.2$ nm in hydrogen-like carbon was demonstrated at

Princeton using a 300 J CO₂ laser [1.26]. Since then, gain has been demonstrated for many different materials, in the soft x-ray region of the spectrum from 3.56 nm [1.27] to 60.8 nm [1.28].

Saturated emission from a soft x-ray laser was first observed at $\lambda = 23$ nm, from a line focus plasma created using germanium slab targets [1.29]. Saturation occurs when the stimulated emission process is significant and reduces the population inversion and gain to 1/2 its value at low intensities. A saturated output is desirable because in that case most of the energy stored in the population inverted plasma is being extracted, creating very intense beams.

There are several pumping mechanisms by which the necessary population inversion could in principle be produced in soft x-ray lasers. These are: collisional recombination, collisional and transient-collisional electron excitation, photoionization and resonant pumping. The most successful mechanism producing a saturated output is electron collisional excitation. As mentioned above, collisional recombination lasers have shown amplified output, but saturation has not been achieved.

Figure 1.2 shows a simplified energy level diagram of the electron impact collisional excitation pumping mechanism of typical neon-like or nickel-like ions. The upper level is directly populated from the ion ground state by large monopole electron excitation. Fast depletion of the lower laser level through a fast radiative decay allows to maintain population inversions in a quasi-steady state mode. This requires a plasma with large electron densities, from $n_e \sim 10^{18}$ to $\sim 3 \times 10^{20} \text{ cm}^{-3}$ and with temperatures that range from 60 to 1000 eV, depending on the lasing wavelength. As long as the density and temperature conditions are right, the population inversion process will continue to occur, in a quasi steady state mode.

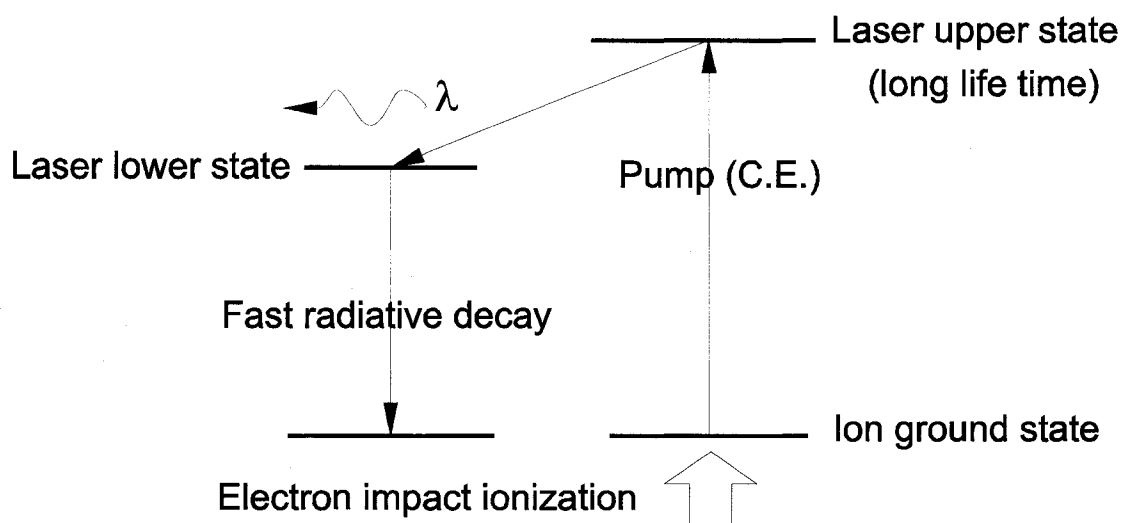


Figure 1.2: Schematic diagram of a four level lasing system for soft x-ray by collisional electron impact excitation.

To produce plasmas with the conditions described above, that allow the population inversion, the first soft x-ray lasers were produced at large facilities designed to pursue inertial confinement fusion. Since then, a large effort has been placed into producing amplification in plasmas created in smaller laboratory setups. Collisionally excited table-top lasers based on fast discharge excitation [1.30, 1.31] and short pulse laser excitation [1.32, 1.33] have both reached gain saturation. Two of these lasers used in this work to perform plasma interferometry studies and are described in the following sections. Specifically, these are a Ne-like capillary discharge laser operating at 46.9 nm and a transient collisionally excited Ni-like laser operating at 14.7 nm.

1.4.1 Ne-Like Ar soft x-ray laser

In the 46.9 nm Ne-like Ar discharge-pumped laser the amplification is generated by excitation of an Ar-filled capillary channel with a fast discharge current pulse [1.34]. Prior to the arrival of the fast current pulse the gas in the capillary channel is seeded with a significant density of free electrons and ions created by a pre-ionizing current pulse of $\sim 1 \mu\text{s}$ duration that reaches $\sim 50 \text{ A}$ amplitude. In this excitation scheme the magnetic force of the fast current pulse rapidly compresses the plasma to form a dense and hot column with a large density of Ne-like ions, a very high axial uniformity, and length to diameter ratio exceeding 1000:1. Collisional electron excitation of the ground state Ne-like ions produces a population inversion and gain in the 3p-3s J=0-1 line [1.34]. Lasing occurs at a time when the electron temperature is 60–80 eV [1.35], with the electron density peaking a few ns later, at a value exceeding $1 \times 10^{19} \text{ cm}^{-3}$. The very good axial uniformity of these plasma columns is evidenced by the excellent measured spatial coherence of the amplified beam [1.36].

The schematic diagram of the capillary discharge soft x-ray laser is shown in Fig. 1.3. In the laser used in the interferometry experiments, the discharge takes place in an aluminum oxide capillary channel, 3.2 mm in diameter and 18–36 cm in length, filled with pre-ionized Ar gas at a pressure of 490 mTorr. The interferometry experiments presented in this work used 27 cm long capillaries. The plasma columns are excited by current pulses of $\sim 26 \text{ kA}$ peak amplitude, with a 10% to 90% rise time of approximately 40 ns.

The excitation current pulse is produced by discharging a water capacitor through a spark gap switch connected in series with the capillary load. The water serves as a liquid dielectric for the capacitor and also is circulated to cool the

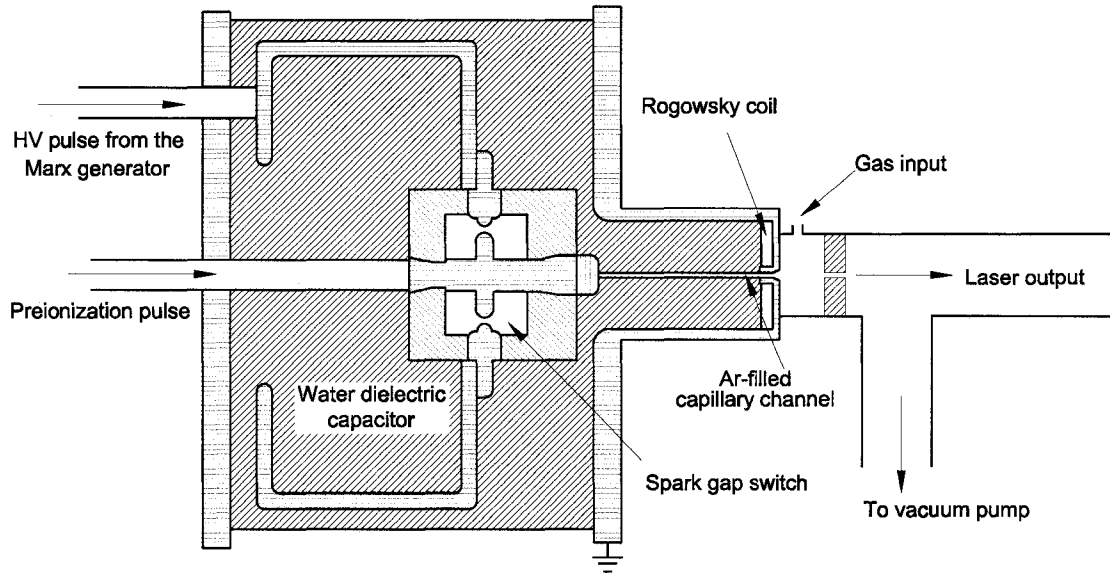


Figure 1.3: Schematic design of the capillary discharge soft x-ray laser.

capillary for repetitive operation. The capacitor is pulse-charged by a compact four-stage Marx generator. The compact typical size of such capillary discharge Ne-like Ar laser is illustrated in Fig. 1.4 with a multimeter included as a size reference.

The laser pulse energy was measured to increase linearly with length from 0.075 mJ for a plasma column 16 cm in length, to 0.88 mJ (2×10^{14} photons/pulse) for a plasma column length of 34.5 cm. The typical capillary lifetime is ~ 5000 laser shots. The measured full width at half maximum laser pulsewidth for an 18.2 cm long amplifier is ~ 1.2 ns [1.31]. Recent measurements demonstrated that full spatial coherence is approached with the longest capillaries and that the peak spectral brightness is about 2×10^{25} photons/(s $mm^2 mrad^2$ 0.01 % bandwidth) [1.36]. This value makes this table-top laser one of the brightest soft x-ray sources available. The temporal coherence length of the laser has been calculated from the Doppler broadened estimated line width to give a value of $\sim 400 \mu m$.

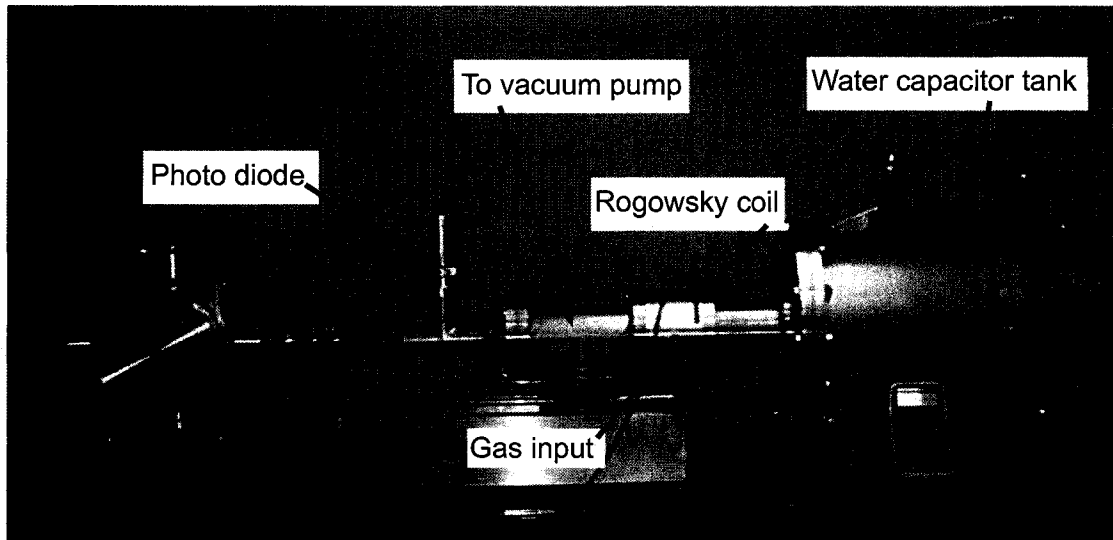


Figure 1.4: Photograph of the capillary discharge 46.9 nm soft x-ray laser. The multimeter is included as a size reference.

1.4.2 Ni-like Pd soft x-ray laser

The first laser-created plasmas for soft x-ray laser amplification were heated by a single optical laser pulse to temperatures and densities appropriate for electron collisional pumping to occur. It was soon realized that it was convenient to use a pre-pulse to form a plasma and then heat this plasma with a second pulse. The advantages of this scheme are a reduction in the refraction of the propagating soft x-ray laser beam and an increased volume where gain can be produced. They result from less steep plasma density profiles, and also from an enhancement in pump laser absorption through inverse bremsstrahlung.

In 1997 it was demonstrated that significantly increased gain could be obtained by a rapid transient excitation with laser pulses of a few picoseconds in duration [1.37]. Moreover, this scheme significantly reduced the pump energy required to produce gain and allowed shorter wavelength saturated soft x-ray lasers to be realized. In this scheme the plasma is heated faster than the relaxation time of the

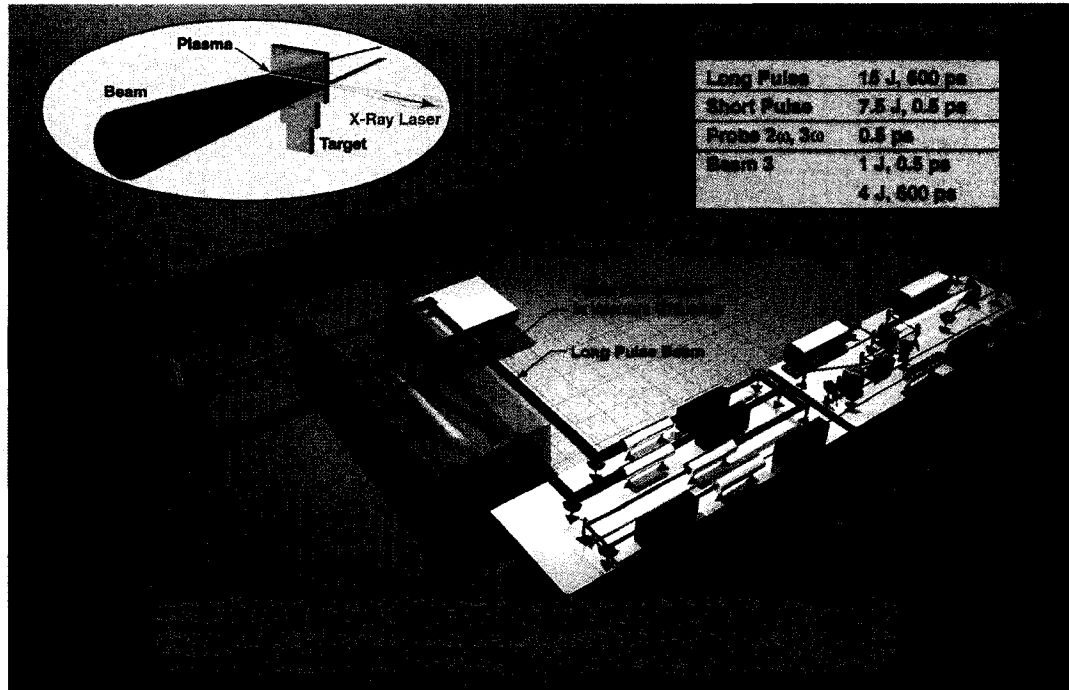


Figure 1.5: COMET laser at Lawrence Livermore National Laboratory.

upper laser states. Since the upper level state has a much larger electron impact excitation rate than the lower level it is possible to generate, for times of the order of 10 ps, population inversion and gains typically 1 order of magnitude larger than those obtained in the quasi steady state regime.

Utilizing this transient collisional excitation scheme, a 14.7 nm Ni-like Pd laser was demonstrated at the Lawrence Livermore National Laboratory, using the table-top Compact Multipulse Terawatt (COMET) laser. The COMET laser occupies two standard optical tables of dimensions 1.2 m \times 3.6 m, with a total area less than 10 m² plus a pulse compressor of 2 m \times 0.75 m, as displayed in schematically in Fig. 1.5. This system is a hybrid chirped-pulse amplification laser consisting of a Ti:sapphire oscillator and a regenerative amplifier tuned to 1053 nm, with a four-stage Nd:phosphate glass amplifier. The 100-fs oscillator pulse is chirped to 1 ns

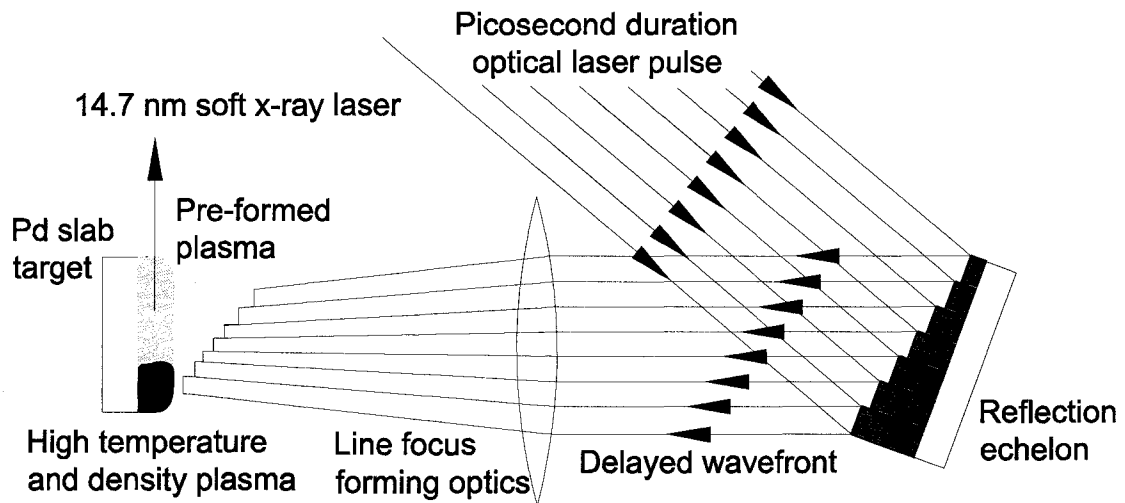


Figure 1.6: Focusing system used to create a traveling wave line focus for soft x-ray laser excitation, by using an echelon reflector.

in a folded single-grating stretcher. The pulse is amplified in 7-, 16-, and 25-mm-diameter rod amplifiers before being split to form two beams that are amplified in two final 50-mm-diameter amplifiers.

One arm is compressed in a vacuum grating compressor box for generation of a short pulse as short as 500-fs (FWHM) duration. The second, long-pulse arm, with a duration of 600 ps (FWHM), is sent through a delay line that can be adjusted to vary the arrival of the short-pulse beam from 0 to 3 ns after the peak of the long-pulse beam. This implementation allows jitter-free synchronization of the two pulses.

The soft x-ray laser used in the interferometry experiments is pumped by these two beams from the chirped pulse amplification laser, a 600 ps long pulse (2 J , $2 \times 10^{11}\text{ Wcm}^{-2}$) and a 5 J energy 6.7 ps or 13 ps (FWHM) short pulse at an

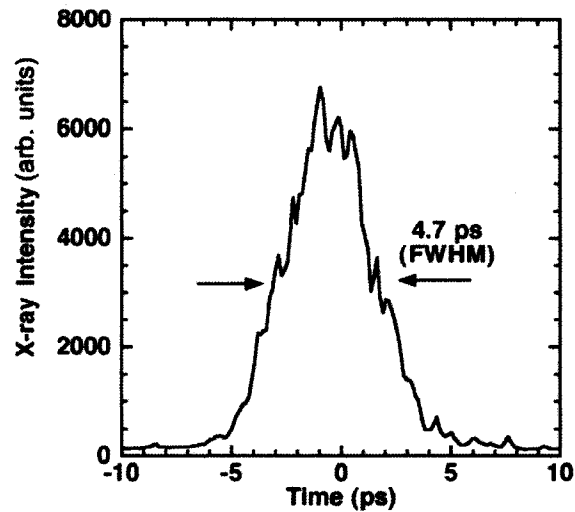


Figure 1.7: Temporal profile of the Ni-like Pd 14.7 nm x-ray laser probe emitted from a 1 cm target and pumped by a 6.7 ps short pulse [1.38].

incident intensity of $6 \times 10^{13} \text{ Wcm}^{-2}$ and $3 \times 10^{13} \text{ Wcm}^{-2}$ respectively. Since the gain duration is short in the transient pump regime (*e.g.* 10 ps), it is advantageous to match the excitation to the propagation of the amplifying x-ray laser beam. This traveling wave line focus excitation is achieved using a reflection echelon that consists of seven flat mirror segments placed before the focusing optics, as shown in Fig. 1.6. Each mirror segment is offset by 0.12 cm to introduce the traveling wave toward the output of the laser with a delay of 7.7 ps per step. This results in a phase velocity of c along the line focus length and ensures that peak gain conditions are experienced by the propagating x-ray laser photons along the entire length of the plasma. The horizontal angular divergence of the soft x-ray laser was measured to be 2.8 mrad. The near field and far field beam characteristics were studied and the laser parameters were optimized to obtain beam properties suitable to perform interferometry.

The temporal properties of the x-ray laser have been recently measured with a fast x-ray streak camera [1.38]. Figure 1.7 shows a sample streak lineout with an x-ray pulse duration of 4.7 ps (FWHM) with an approximately Gaussian shape for a 6.7 ps short pump pulse. For saturated x-ray laser output, obtained using a 13 ps pumping pulse, the measured x-ray duration is slightly longer at 5.9 ps [1.38]. The temporal coherence length of this laser was measured using a Michelson interferometer setup that yield a value of $\sim 400 \mu\text{m}$ [1.39]. While the spatial coherence of this laser was not measured, the interferometry experiments performed with it show that the spatial coherence is enough to perform amplitude division interferometry experiments.

Bibliography

- 1.1 A.A. Michelson and E.W. Morley. On the Relative Motion of the Earth and the Luminiferous Ether. *American Journal of Science*, 34(203):333–345, November 1887.
- 1.2 L Zehnder. Ein neuer Interferenzrefraktor. *Z. Instrumenten Kd*, 11:275, 1891.
- 1.3 L Mach. Ueber einen Interferenzrefraktor. *Z. Instrumentenkd*, 12:89, 1892.
- 1.4 R.A. Brossier, P. and Blanken. Interferometry at $337\ \mu\text{m}$ on a Tokamak Plasma. *IEEE Transactions on Microwave Theory and Techniques*, MTT-22(12):1053–1056, December 1974.
- 1.5 D. T. Attwood, D. W. Sweeney, J. M. Auerbach, and P.H.Y. Lee. Interferometric Confirmation of Radiation-Pressure Effects in Laser-Plasma Interactions. *Phys. Rev. Lett*, 40:184–187, 1978.
- 1.6 P. E. Young and P. R. Bolton. Propagation of subpicosecond laser pulses through a fully ionized plasma. *Phys. Rev. Lett.*, 77(22):4556–4559, Nov 1996.
- 1.7 M. D. Rosen, P. L. Hagelstein, D. L. Matthews, E. M. Campbell, A. U. Hazi, B. L. Whitten, B. Macgowan, R. E. Turner, R. W. Lee, G. Charatis,

- G. E. Busch, C. L. Shepard, and P. D. Rockett. Exploding-foil technique for achieving a soft-x-ray laser. *Physical Review Letters*, 54(2):106–109, 1985.
- 1.8 L. B. Da Silva, T. W. Barbee Jr., R. Cauble, P. Celliers, D. Ciarlo, S. Libby, R. A. London, D. Matthews, S. Mrowka, J. C. Moreno, D. Ressler, J.E. Trebes, A. S. Wan, and F. Weber. Electron density measurements of high density plasmas using soft x-ray laser interferometry. *Physical Review Letters*, 74(20):3991, 1995.
- 1.9 A. S. Wan, T. W. Barbee, R. Cauble, P. Celliers, L. B. Da Silva, J. C. Moreno, P. W. Rambo, G. F. Stone, J. E. Trebes, and F. Weber. Electron density measurement of a colliding plasma using soft-x-ray laser interferometry. *Physical Review E*, 55(5):6293–6296, 1997.
- 1.10 C. H. Moreno, M. C. Marconi, K. Kanizay, J. J. Rocca, Y. A. Uspenskii, A. V. Vinogradov, and Y. A. Pershin. Soft-x-ray laser interferometry of a pinch discharge using a tabletop laser. *Physical Review E*, 60(1):911–917, 1999.
- 1.11 Bridget Marx. Laser-produced-plasma sources shine brighter. *Laser Focus World*, 39(4):34,36,38, 2003.
- 1.12 Kathy Kincade. Extreme-UV sources are on track for next-generation chip manufacturing. *Laser Focus World*, 39(2):55, February 2003.
- 1.13 John Lindl. Development of the indirect-drive approach to inertial confinement fusion and the target physics basis for ignition and gain. *Physics of Plasmas*, 2(11):3933–4024, 1995.

- 1.14 R.W. Hockney and J.W. Eastwood. *Computer Simulations Using Particles*. McGraw-Hill, New York, 1981.
- 1.15 D. Attwood. *soft x-rays and extreme ultraviolet radiation*, chapter 6, page 211. Physics of hot dense plasmas. Cambridge University Press, Cambridge, 2000.
- 1.16 J Nuckolls, L Wood, A Thiessen, and G.B. Zimmerman. Laser Compression of Matter to Super-High Densities: Thermonuclear (CTR) Applications. *Nature*, 239(5386):139–142, 1972.
- 1.17 M. M. Marinak, B. A. Remington, S. V. Weber, R. E. Tipton, S. W. Haan, K. S. Budil, O. L. Landen, J. D. Kilkenny, and R. Wallace. Three-dimensional single mode rayleigh-taylor experiments on nova. *Phys. Rev. Lett.*, 75(20):3677–3680, Nov 1995.
- 1.18 I. H. Hutchinson. *Principle of Plasma Diagnostics*, chapter 5, page 201. Cambridge University Press, 2002.
- 1.19 I. H. Hutchinson. *Principle of Plasma Diagnostics*, chapter 6, page 253. Cambridge University Press, 2002.
- 1.20 D. H. Kalantar and D. A. Hammer. Observation of a stable dense core within an unstable coronal plasma in wire-initiated dense z-pinch experiments. *Phys. Rev. Lett.*, 71(23):3806–3809, Dec 1993.
- 1.21 R.S. Craxton, F.S. Turner, R. Hoefen, C. Darrow, E.F. Gabl, and G. E. Busch. Characterization of laser-produced plasma density profiles using grid image refractometry. *Physics of Fluids B*, 5(12), 1993.

- 1.22 D. Attwood. *Soft X-Rays and Extreme Ultraviolet Radiation. Principles and Applications*, chapter 3, pages 55–61. Cambridge University Press, 2000.
- 1.23 L.D. Landau, E.M. Lifshitz, and L.P. Pitaevskii. *Electrodynamics of Continuous Media*, chapter 8, pages 279–281. Pergamon Press, 1984.
- 1.24 B. L. Henke, E. M. Gullikson, and J. C. Davis. X-ray interactions : photoabsorption, scattering, transmission, and reflection at $E = 50\text{--}30000$ eV, $Z=1\text{--}92$. *Atomic Data and Nuclear Data Tables*, 54(2):181–342, 1993.
- 1.25 D. L. Matthews, P. L. Hagelstein, M. D. Rosen, M. J. Eckart, N. M. Ceglio, A. U. Hazi, H. Medeck, B. J. MacGowan, J. E. Trebes, B. L. Whitten, E. M. Campbell, C. W. Hatcher, A. M. Hawryluk, R. L. Kauffman, L. D. Pleasance, G. Rambach, J. H. Scofield, G. Stone, and T. A. Weaver. Demonstration of a soft x-ray amplifier. *Phys. Rev. Lett.*, 54(2):110–113, Jan 1985.
- 1.26 S. Suckewer, C. H. Skinner, H. Milchberg, C. Keane, and D. Voorhees. Amplification of stimulated soft x-ray emission in a confined plasma column. *Phys. Rev. Lett.*, 55(17):1753–1756, Oct 1985.
- 1.27 B. J. MacGowan, L. B. Da Silva, D. J. Fields, C. J. Keane, J. A. Koch, R. A. London, D. L. Matthews, S. Maxon, S. Mrowka, A. L. Osterheld, J. H. Scofield, G. Shimkaveg, J. E. Trebes, and R. S. Walling. Short wavelength x-ray laser research at the lawrence livermore national laboratory. *Physics of Fluids B: Plasma Physics*, 4(7):2326–2337, 1992.
- 1.28 F. G. Tomasel, J. J. Rocca, V. N. Shlyaptsev, and C. D. Macchietto. Lasing at 60.8 nm in ne-like sulfur ions in ablated material excited by a capillary discharge. *Phys. Rev. A*, 55(2):1437–1440, Feb 1997.

- 1.29 A. Carillon, H. Z. Chen, P. Dhez, L. Dwivedi, J. Jacoby, P. Jaegle, G. Jamelot, Jie. Zhang, M. H. Key, A. Kidd, A. Klisnick, R. Kodama, J. Krishnan, C. L. S. Lewis, D. Neely, P. Norreys, D. Ochar39Neill, G. J. Pert, S. A. Ramsden, J. P. Raucourt, G. J. Tallents, and J. Uhomoihi. Saturated and near-diffraction-limited operation of an xuv laser at 23.6 nm. *Phys. Rev. Lett.*, 68(19):2917–2920, May 1992.
- 1.30 B. R. Benware, C. D. Macchietto, C. H. Moreno, and J. J. Rocca. Demonstration of a high average power tabletop soft x-ray laser. *Physical Review Letters*, 81(26):5804–5807, 1998.
- 1.31 C. D. Macchietto, B. R. Benware, and J. J. Rocca. Generation of millijoule-level soft-x-ray laser pulses at a 4-Hz repetition rate in a highly saturated tabletop capillary discharge amplifier. *Optics Letters*, 24:1115–1117, August 1999.
- 1.32 J. Dunn, Y. Li, A. L. Osterheld, J. Nilsen, J. R. Hunter, and V. N. Shlyaptsev. Gain saturation regime for laser-driven tabletop, transient Ni-like ion x-ray lasers. *Physical Review Letters*, 84(21):4834–4837, 2000.
- 1.33 S. Sebban, R. Haroutunian, P. Balcou, G. Grillon, A. Rousse, S. Kazamias, T. Marin, J. P. Rousseau, L. Notebaert, M. Pittman, J. P. Chambaret, A. Antonetti, D. Hulin, D. Ros, A. Klisnick, A. Carillon, P. Jaegle, G. Jamelot, and J. F. Wyart. Saturated amplification of a collisionally pumped optical-field-ionization soft x-ray laser at 41.8 nm. *Physical Review Letters*, 86(14):3004–3007, 2001.
- 1.34 J. J. Rocca, V. Shlyaptsev, F. G. Tomasel, O. D. Cortazar, D. Hartshorn, and J. L. A. Chilla. Demonstration of a discharge pumped table-top soft-x-ray laser. *Physical Review Letters*, 73(16):2192–2195, 1994.

- 1.35 J. J. Rocca, D. P. Clark, J. L. A. Chilla, and V. N. Shlyaptsev. Energy extraction and achievement of the saturation limit in a discharge-pumped table-top soft x-ray amplifier. *Physical Review Letters*, 77(8):1476–1479, 1996.
- 1.36 Y. Liu, M. Seminario, F. G. Tomasel, C. Chang, J. J. Rocca, and D. T. Attwood. Achievement of essentially full spatial coherence in a high-average-power soft-x-ray laser. *Physical Review A*, 63(033802), 2001.
- 1.37 P. V. Nickles, V. N. Shlyaptsev, M. Kalachnikov, M. Schnürer, I. Will, and W. Sandner. Short pulse x-ray laser at 32.6 nm based on transient gain in ne-like titanium. *Phys. Rev. Lett.*, 78(14):2748–2751, Apr 1997.
- 1.38 J. Dunn, R. F. Smith, R. Shepherd, R. Booth, J. Nilsen, J. R. Hunter, and V. N. Shlyaptsev. Temporal characterization of a picosecond laser-pumped x-ray laser (for applications). In E. E. Fill and S. Suckewer, editors, *SPIE Int. Soc. Opt. Eng. Proc*, volume 5197, pages 51–59, 2003.
- 1.39 R. F. Smith, J. Dunn, J. R. Hunter, J. Nilsen, S. Hubert, S. Jacquemot, C. Remond, R. Marmoret, M. Fajardo, P. Zeitoun, and L. Vanbostal. Longitudinal coherence measurement of a transient collisional x-ray laser. *Optics Letters*, 28(22):2261–2263, 2003.

”in recognition of pioneering research and leadership in the use of lasers and ion particle beams to produce unique high-energy-density matter for scientific research and for controlled thermonuclear fission.”

Zimmerman, a group leader at Livermore, is responsible for development of advanced numerical models including the LASNEX code system. He is known internationally for his development of LASNEX and received the U.S. Department

of Energy's E. O. Lawrence Award for this work. He has made key contributions to the development of models for equations of state, charged-particle and photon transport, opacity, magnetic field generation, and hydrodynamics. LASNEX is the principal inertial confinement fusion design code at Livermore, Los Alamos, and Sandia national laboratories.

Chapter 2

**DIFFRACTION GRATING SOFT X-RAY
LASER INTERFEROMETRY**

Optical lasers have been used for decades to diagnose dense plasmas utilizing techniques that include interferometry, deflectometry, shadowgraphy and scattering [2.1, 2.2]. Of all these techniques, interferometry is the one that allows the most direct measurement without the need to rely on modelling or computations. This powerful technique, that has been widely used to study many types of plasmas [2.2], provides information in the form of two-dimensional maps of the electron density, and was extensively used with optical probe wavelengths. However, because the maximum density that can be probed is limited by plasma refraction, by the limited number of fringe shifts that can be detected experimentally, and by the absorption of the probe beam, optical interferometry cannot be used to successfully probe all plasmas. All these limitations are diminished by a reduction in the wavelength of the probe beam, so the use of shorter wavelength lasers can significantly extend the plasma parameter space that can be probed interferometrically. Soft x-ray lasers are suitable for plasma interferometry, their short wavelength amounts to a high critical plasma density for the probe beam reaching values well above solid densities¹. The short wavelength results in reduced diffraction that improves the resolution of the images obtained, and the high monochromaticity of the light sources allows for the use of multilayer-coated optics as filters to discriminate the probe beam from the strong self-emission of hot dense plasmas.

Being able to probe plasma conditions with very high densities and temperatures will make interferometry applicable to extreme cases like those present in inertial confinement fusion for example. This constitutes one of the main motivations

¹The critical density at 46.9 nm and 14.7 nm is $5.08 \times 10^{23} \text{ cm}^{-3}$ and $5.09 \times 10^{24} \text{ cm}^{-3}$ respectively.

for pursuing soft x-ray lasers as probe sources for dense plasma interferometry, and for extending the probe beam to shorter wavelengths and pulse durations.

The chapter starts with a description of the interferometry technique and its application to plasma diagnostics, then discusses the main factors that limit the density and density gradients that can be measured, and the dependence of these factors on the wavelength of the probe beam. This is followed by a review of interferometers that have been used in the soft x-ray region of the spectrum. The Diffraction Grating Interferometer is described next. This soft x-ray interferometer was initially designed to operate at a 46.9 nm probe wavelength. Subsequently a second version of the interferometer was designed to operate at a 14.7 nm probe wavelength. The first results obtained with the interferometer are presented in this chapter. Other experiments, performed with each of these interferometers are presented in the next two chapters.

2.1 Interferometry

Interferometry is a technique that permits the measurement of distances with sub-wavelength precision (*e.g.* $\lambda/10$ or better) by measuring the optical path difference between two light beams. This optical path difference can be produced, for example, by a difference in length due to a deformation of a reflective surface, or by a difference in the index of refraction of a material that the beam travels through. In a typical interferometer two waves interfere adding their electric fields. The resulting field will be modulated according to the phase difference between the two waves. In a monochromatic interferometer, the addition of $E_1(t) = E_1 e^{i\omega t}$ and $E_2(t) = E_2 e^{i(\omega t + \phi)}$ results in

$$E_T(t) = (E_1 + E_2 e^{i\phi}) e^{i\omega t}. \quad (2.1)$$

In a detector, the intensity measured will be given by the square of the field,

$$|E_T|^2 = E_1^2 + E_2^2 + 2E_1E_2\cos(\phi). \quad (2.2)$$

The intensity detected will thus have a constant component that depends on the intensity of each of the probe beams and a varying component that also depends on the phase between the two interfering waves. In imaging interferometry this information is obtained in the form of a phase map that, at each point in the image, gives the accumulated phase in the probe beam with respect to the reference beam. The phase shift is related to the number of fringe shifts, N_f , through $N_f = \frac{\Delta\phi}{2\pi}$.

The number of fringe shifts produced in an interferogram, due to a material of a certain index of refraction η , is given by the difference in optical path between a reference beam and the probe beam that traverses the material, in units of the probe wavelength(λ) and integrated over the material's length L:

$$N_f = \frac{1}{\lambda} \int_0^L (1 - \eta) dl, \quad (2.3)$$

which, for the case of a uniform material with a constant index of refraction along the probing path, becomes

$$N_f = \frac{L(1 - \eta)}{\lambda}. \quad (2.4)$$

By measuring the number of fringe shifts it is then possible to obtain a map of the index of refraction of the material probed. For cases in which the material is not uniform along the propagation direction of the probe beam, but another symmetry can be assumed, a mathematical transformation (for example an Abel inversion in the case of a plasma with cylindrical symmetry) can be used to deconvolve the information measured in the interferogram and obtain a three-dimensional map of the index of refraction.

In plasma interferometry the measured index of refraction data can be converted to electron density information, which is one of the most important plasma parameters. The index of refraction of a plasma was shown in chapter one (section 1.3) to have the following dependence on the electron density, n_e , when bound electrons are ignored:

$$\eta = \sqrt{1 - \frac{n_e}{n_c}}, \quad (2.5)$$

where $n_c = \frac{\pi}{r_e \lambda^2}$ is the critical density of the plasma, which is in general much larger than the density of the plasma probed, so to first order, the index of refraction is given by

$$\eta = 1 - \frac{n_e}{2n_c}. \quad (2.6)$$

Therefore, using this index of refraction expression together with (2.4), the number of fringe shifts can be written as the following simple expression,

$$N_f = \frac{Ln_e}{2\lambda n_c}. \quad (2.7)$$

Under these conditions, using interferometry to obtain the electron density of plasmas is a very direct measurement that doesn't require modeling or sophisticated analysis of the data. Laser interferometry of plasmas was implemented shortly after the invention of the laser [2.3]. Soon, the limitations of optical lasers to the study of dense plasmas became evident and shorter wavelengths, initially in the ultra violet region, were pursued. These limitations are described in the next section.

2.2 Advantages of shorter probe wavelengths in plasma interferometry

The limitations of interferometry to the study of dense plasmas are the refraction and absorption of the probe beam. An additional limitation is imposed

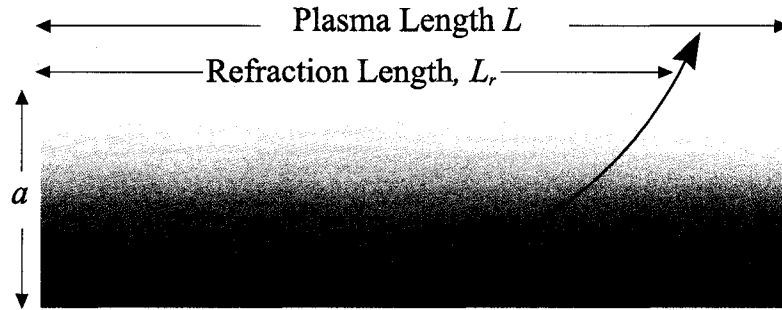


Figure 2.1: Ray propagating through a plasma, showing the refraction length L_r , that is shorter than the plasma length L

by the detector resolution, which limits the maximum number of fringe shifts that can be detected. It will be shown in this section that all these effects are reduced by reducing the wavelength of the probe beam. An added advantage is that the diffraction-limited resolution of the imaging system used to image the plasma and interference fringes improves as the wavelength is reduced.

2.2.1 Refraction of the probe beam

When light travels through a medium with a changing index of refraction it can be deflected off its straight trajectory by refraction. Some everyday examples of this phenomenon are the highway mirage, a pool of water seen on a road when driving in a hot summer day, or the distorted air behind a jet engine due to turbulence. In these examples, a gradient in the density of air becomes a gradient in the index of refraction that modifies the trajectory of the rays that travel through the air, distorting the observed image. This same phenomenon can occur in a plasma where the index of refraction depends on the plasma electron density as described by expression 2.5. A steep electron density gradient in the plasma translates into a steep gradient in the index of refraction that can deflect the probe beam out of its straight trajectory. Figure 2.1 illustrates a ray being refracted as it travels through

a long plasma of transverse size a . In this picture L_r is the refraction length, or the distance the probe beam travels through the plasma before it is deflected out of it, as defined by London [2.4]. To obtain a functional dependence of the refraction with the wavelength, London used the special case of a parabolic density profile. In that case, the refraction length L_r , is given by

$$L_r = a\sqrt{n_c/n_e}. \quad (2.8)$$

Since $n_c = \frac{\pi}{r_e\lambda^2}$, the length of refraction is inversely proportional to the wavelength of the probe beam. This means that reducing the probe wavelength will increase the length of plasma that can be transversed before the ray deviation is significant. In the general case, if the density gradients are large enough, the probe beam will be deflected completely off its trajectory. This can make it very difficult to accurately extract density information from the interferograms [2.5]. In the extreme case of large refraction angles the probe beam might not be collected by the imaging system, precluding measurements in the steep density regions. Moreover, the rays probing different regions of the plasma can intermix, making the analysis very complicated or impossible.

To illustrate the refraction effects of a density profile on different probe beam wavelengths, ray tracing simulations were performed and are shown in Fig. 2.2. Three different two-dimensional simulations (the rays are constrained to move in a plane) were performed: one for each of the two soft x-ray probe wavelengths used in this work (14.7 and 46.9 nm) and a comparison test using a 266 nm wavelength that corresponds to the 4th harmonic of a Nd:YAG laser, one of the shortest optical wavelengths readily available for use in plasma diagnostics. An exponential density profile, typical of plasmas created by laser ablation of solid targets, was used for

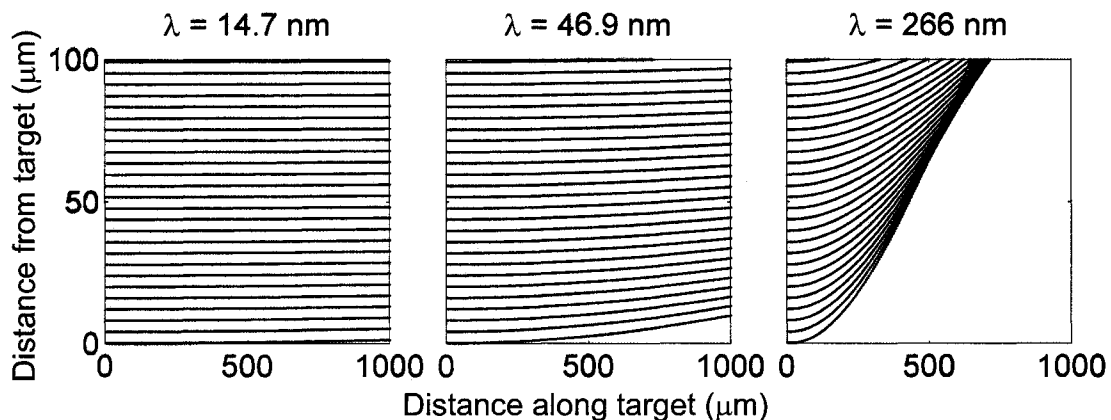


Figure 2.2: Numerical computations of the trajectories of rays traveling through a plasma with an exponential density profile given by equation 2.9. The plasma is assumed to be uniform along the direction of propagation. The shorter wavelength rays (46.9 nm and 14.7 nm) experience much less deflection than the 4th harmonic of a YAG laser (266 nm). Notice that the horizontal scale is 10 times larger than the vertical scale.

the ray tracing calculations

$$n(x) = 10^{21} e^{-x/50} (\text{cm}^{-3}), \quad (2.9)$$

with the distances measured in μm .

The beneficial effect of reducing the probe wavelength is evident from the comparison of the ray traces at different wavelengths. The 266 nm probe wavelength rays that start within the first 60 μm from the target surface are greatly refracted during the first 200 μm of travel through the plasma. This means that a 200 μm long plasma with this density profile would be too long to be studied with a 266 nm probe. It would be very difficult to obtain density information from an interferogram obtained at this wavelength and in this region. On top of this, a real density profile could be much steeper close to the target causing a crossover of the rays complicating the analysis even more. In contrast, the 46.9 nm calculation

shows rays that significantly curve away from the target only in the first few μm from the target surface. The first few μm from the target surface are still inaccessible to probing, but it is possible to obtain reliable density information everywhere else. The refraction is further reduced when the probe wavelength is reduced to 14.7 nm. The ray tracing calculations show that the rays are barely deflected, even after traveling the whole target length of 1 mm.

It is evident from this example that there is a definite advantage in reducing the wavelength of the probe beam to reduce refraction effects and to be able to probe steeper densities and longer plasmas. Longer wavelengths can only be used to probe small scale plasmas in which refraction is not strong enough to significantly deflect the beams.

Knowledge of the extent and effect of refraction in actual experimental settings is important for accurate analysis of the data. A grid refractometry study was performed in combination with the 14.7 nm wavelength probe [2.6]. That study showed that, for those experiments, the data obtained with the interferometer could be analyzed without the need of corrections due to refraction.

2.2.2 Absorption of the probe beam

Another effect that limits the maximum plasma density and size that can be measured is absorption of the probe beam. If the probe beam is completely absorbed as it travels through the plasma then no information will be obtained from that part of the plasma. There are three main processes through which photons can be absorbed as they traverse a plasma. These are line absorption, photoionization and inverse bremsstrahlung [2.7]. Resonant line absorption, or the absorption of a photon by an electron that experiences a discrete bound-bound transition, is possible, but in general it doesn't happen because of the narrow line

width of the soft x-ray lasers. Soft x-ray lasers have enough energy to photoionize several elements and some of its ions. For example, the 26.5 eV photon energy corresponding to 46.9 nm wavelength is larger than the first 2 ionization potentials for aluminum (6 and 18.8 eV). In many hot plasmas the level of ionization is high enough to eliminate any photoionization absorption, and the effect is only observed late in the plasma evolution when colder plasma is present.

Inverse bremsstrahlung, also known as free-free absorption, is a collisional process in which a free electron gains energy by absorbing a photon while interacting with an ion. The direct process, bremsstrahlung, is the emission of radiation due to the collisions of free electrons with an ion. In a plasma dominated by free-free absorption, the absorption coefficient α is given approximately by [2.8].

$$\alpha \approx 2.44 \times 10^{-37} \frac{\langle Z^2 \rangle n_e n_i}{\sqrt{kT} (h\nu)^3} [1 - \exp(\frac{-h\nu}{kT})] \text{cm}^{-1}, \quad (2.10)$$

where the electron temperature kT and the photon energy $h\nu$ are in eV and the electron and ion densities are in cm^{-3} . With the absorption coefficient α , it is possible to calculate the transmission through a plasma. The calculation was done assuming a 1 mm long plasma with a temperature of 100 eV, a mean ionization of 10 and three different electron densities: 10^{19} , 10^{20} and 10^{21}cm^{-3} . The results are shown in Fig. 2.3. It can be seen from this figure that the free-free absorption is greatly reduced when the wavelength of light is reduced. In general, absorption is not a limitation unless the plasma density approaches very high densities. The critical density of the probe beam is the cutoff density for propagation, but for soft x-ray wavelengths it can exceed the solid density of many materials. Therefore, absorption is usually not the main limitation for soft x-ray interferometry. Instead, refraction is usually a more limiting factor to the highest density that can be

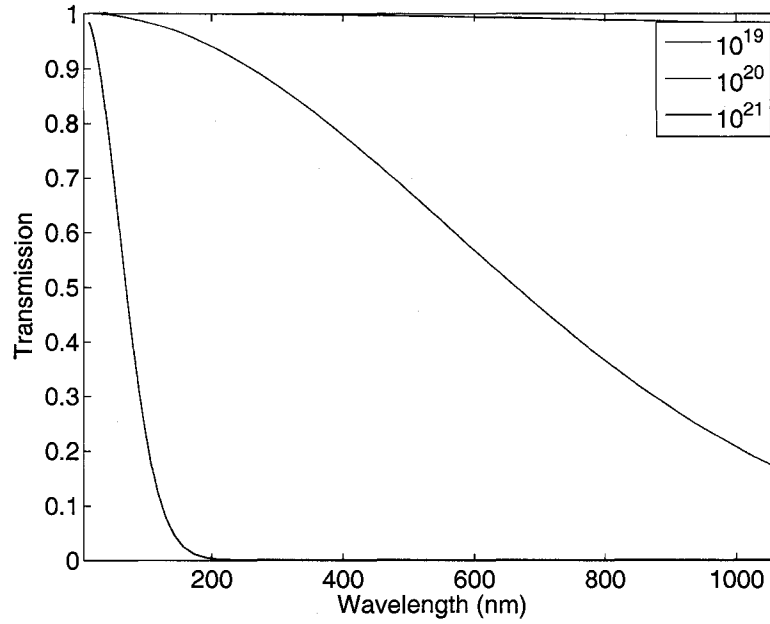


Figure 2.3: Transmission in a 1 mm long plasma due to free-free absorption as a function of the wavelength for a 100 eV plasma with a mean ionization of 10, for three different plasma electron densities.

probed. Figure 2.4 shows the plasma parameter space accessible with different probe wavelengths. As the wavelength is shortened, the density and plasma length that can be probed increase. The graph was constructed by plotting the $\alpha \cdot L_r = 1$ curve that, when written in terms of the electron density, becomes $n_e^2 \cdot L_r \cdot f(\lambda) = 1$, where $f(\lambda)$ is a function of the wavelength. The refraction curve was constructed using the refraction length L_r given by London [2.4]: $n_e \cdot L_r^2 \cdot g(\lambda) = 1$, in this case $g(\lambda)$ is a different function of the wavelength. This dependence results in the very high density part of the graph to be limited by free-free absorption while the lower density and long plasma length part to be limited by refraction. The plasmas probed in this work all lie in the refraction limited region of the graph.

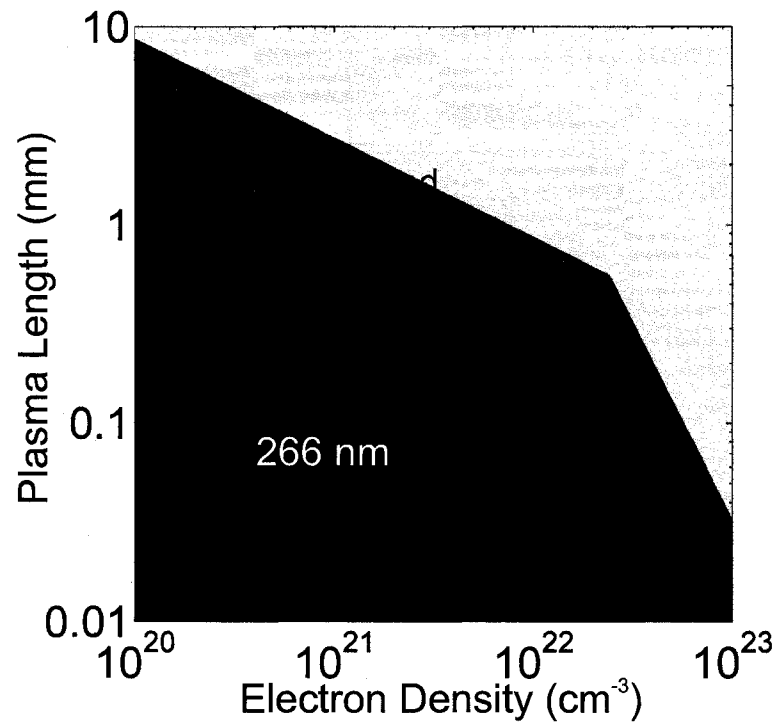


Figure 2.4: Parameter space accessible for different probe wavelength due to the limitations imposed by refraction and free-free absorption.

2.2.3 Detectable fringe density

A limitation to the maximum density that can be probed is given by the maximum number of fringe shifts that can be measured or the smallest fringes that can be resolved by the detector system. The number of fringe shifts observed in an interferogram due to a density n_e is given by equation 2.7. It can be written in terms of the wavelength λ by using the expression for the critical density $n_c = \frac{\pi}{r_e \lambda}$

$$N_f \approx \frac{n_e L}{2n_c \lambda} = \frac{n_e r_e \lambda L}{2\pi}, \quad (2.11)$$

so the number of fringe shifts in the interferogram is reduced when a shorter probe wavelength is used. For example, a 1 mm long plasma with a uniform density of 10^{20} cm^{-3} will produce 12 fringe shifts at 266 nm, but only 2.1 fringe shifts at 46.9 nm and 0.66 fringe shifts at 14.7 nm. This is exemplified in the synthesized interferograms of Fig. 2.5. The interferograms were constructed assuming a 1 mm long cylindrical density profile with an exponential decay in the radial distance, r :

$$n(r) = 10^{21} e^{-r/50} \text{ (cm}^{-3}\text{)} \quad (2.12)$$

with the distances measured in μm . The interferogram corresponding to the 266 nm probe wavelength shows many thin fringes that are impossible to resolve. No accurate fringe shift information can be obtained from the interferogram, especially after considering the effect of the finite size of the detector pixel. The interferograms corresponding to the probe wavelengths of 46.9 nm and 14.7 nm show interference fringes that can be well resolved. In particular, the shortest wavelength interferogram shows fringes that are wide and should be easy to analyze.

There are no experimental results reported in the literature where plasma density profiles have been determined from more than 20 fringe shifts [2.9]. It is

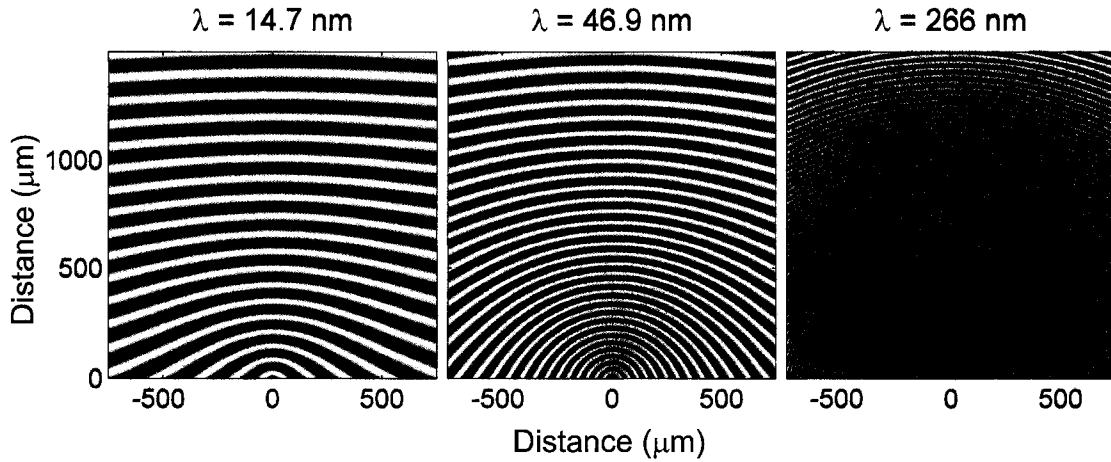


Figure 2.5: Simulated interferograms for different probe wavelengths show the effect of reducing the wavelength on the number of fringe shifts. All the interferograms were computed using the same density profile, a radially decreasing exponential given by equation 2.12. The peak density was 10^{21} cm^{-3}

then reasonable to set 20 as the maximum number of fringe shifts. For 266, 46.9 and 14.7 nm wavelength probes going through a 1 mm long plasma, this number of fringe shifts translates into maximum densities of $1.6 \times 10^{20} \text{ cm}^{-3}$, $9.5 \times 10^{20} \text{ cm}^{-3}$ and $3 \times 10^{21} \text{ cm}^{-3}$. On the other hand, the reduced number of fringe shifts comes with a reduced sensitivity for lower densities. For the case in which one tenth of a fringe shift is the lowest resolvable fringe displacement, the lowest densities that can be measured for a millimeter long plasma are $1.5 \times 10^{19} \text{ cm}^{-3}$ for the 14.7 nm laser, $4.8 \times 10^{18} \text{ cm}^{-3}$ for the 46.9 nm laser and $7.4 \times 10^{17} \text{ cm}^{-3}$ for the 266 nm laser. These are an upper bound values to the error of the determination of the electron density in plasma interferometry. The error, depending on the plasma density being measured, can be as low as 1 %, as compared to 20–30 % for other diagnostic techniques [2.1]. The typical errors in the determination of the electron density from the interferograms in this work were estimated to be always less than 5 %. All this indicates that the probe wavelength used for interferometry should

be selected according to the density and size of the plasma that will be probed and that to measure large scale, high density plasmas it is necessary to reduce the wavelength of the probe beam.

2.3 Review of previous soft x-ray laser interferometers

Performing interferometry in the soft-x ray region of the spectrum, implies overcoming some difficulties inherent to working with short wavelengths. The reflectivity at these wavelengths is greatly reduced, but it can be improved by using grazing incidence reflections or high reflectivity multilayer soft x-ray mirrors.

Interferometers can be built as wave front division or amplitude division. In the former, the beam is spatially divided into a probe arm, where the medium to be studied is placed, and a reference arm, that contains the original phase information of the beam. When these arms are recombined the interference pattern is formed. In the case of wavefront division interferometers, a good visibility of the interference fringes is going to depend on a good spatial coherence length of the probe laser wavefront, because the two arms of the interferometer are formed by different portions of the beam. The spacial coherence of the beam used in the interferometer can be improved by placing the laser source far away from the interferometer as, according to the Huyghens-Fresnel principle [2.10], the beam's transverse coherence increases with the distance from the source, however, this sacrifices photon fluence.

In amplitude division interferometers the two arms are formed using beam splitters that partially reflect and transmit the beam. The resulting interfering arms have the same spatial characteristics and are coherent so spatial coherence is not a limitation for the quality of the fringes. The beam splitters used to construct

amplitude division interferometers that work at soft x-ray wavelengths have been free standing thin film multilayer mirrors which are very fragile when exposed to plasma debris [2.11].

Several soft x-ray interferometers are discussed next, with either wavefront division or amplitude division configurations used.

2.3.1 Wavefront division soft x-ray interferometers

The simplest interferometer that can be constructed is based on the Lloyd's mirror configuration [2.12]. This interferometer was implemented in the soft x-ray region of the spectrum by Rocca *et al.* [2.13] and was used in the study of a pinch discharge plasma [2.14]. The Lloyd's mirror interferometer, shown schematically in Fig. 2.6, consists of a reflection in a grazing incidence mirror that intercepts a portion of the beam from the soft x-ray laser source. The fringe pattern arises from the superposition of this portion of the beam with the one that propagates directly from the source. Due to the single grazing reflection this interferometer has high throughput and is very suitable for its use with soft x-ray lasers. The fringe spacing is determined by the angle of incidence, δ , of the probe beam on the mirror, and by the distances from the point source to the mirror and from the mirror to the image plane, b and c respectively.

$$\Delta I = \frac{(b+c)\lambda}{2b \sin \delta}. \quad (2.13)$$

The plasma to be probed is placed in one portion of the beam, while the other portion is used as a reference. The maximum transverse plasma size that can be probed is determined by the mirror length and the angle of incidence on the mirror, and by the spatial and temporal coherence of the laser. The two overlapping portions of the beam originate from different parts in the wavefront,

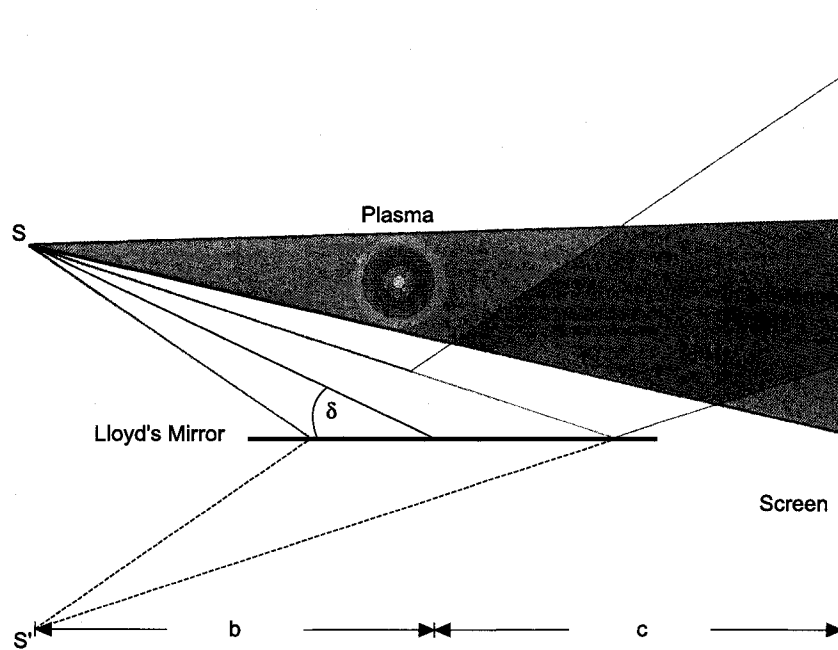


Figure 2.6: Schematic diagram of the Lloyd's mirror interferometer. The real source S and the virtual source S' (formed by a reflection on the mirror) interfere and fringes can be observed on the screen.

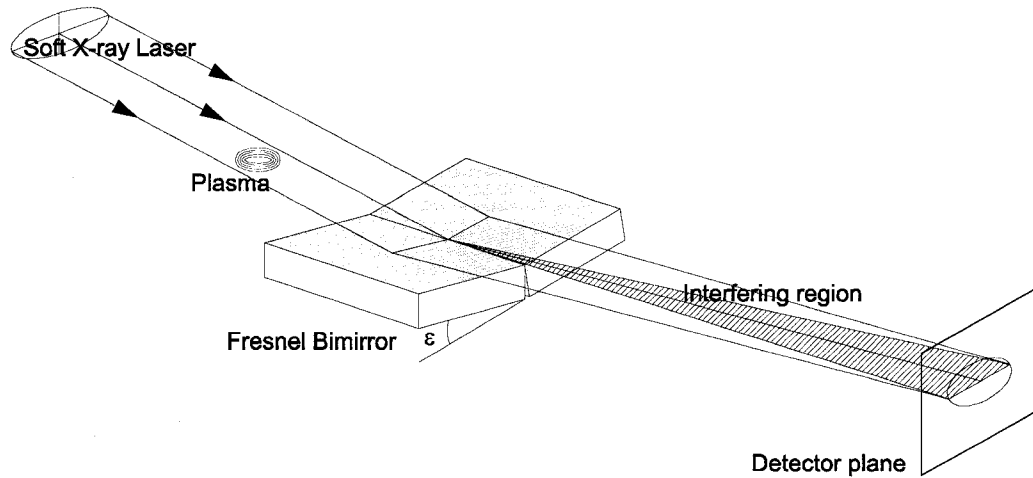


Figure 2.7: Schematic diagram of the Fresnel bi-mirror interferometer. The interference pattern is formed by the overlap of the two portions of the beam produced by the tilt of the mirrors.

which demands better spatial coherence on the source to produce good fringe visibility. Also the paths of the two arms of the interferometer are different, which requires a longer temporal coherence length. Furthermore, the plasma size that can be probed is not independent of the fringe spacing.

The Fresnel Bi-mirror Interferometer [2.12] is almost as simple as the Lloyd's Mirror. It consists of two flat mirrors joined together at one side with a slight tilt between them, as depicted in Fig. 2.7. The light incident at a grazing angle on the mirrors is reflected, and due to this tilt, overlapped, generating interference fringes that can be seen on the screen. The fringe spacing can, in this case, be controlled by the relative tilt of the two mirrors. This interferometer was adapted to soft x-ray wavelengths and used in combination with a 21.2 nm Ne-like Zn soft x-ray laser by Albert *et al.* [2.15], and was demonstrated in studying the effect of high

electric fields on Nb surfaces [2.16]. Another implementation of this interferometer was designed by Joyeux *et al.* [2.17] and used in combination with a 13.9 nm Ag laser to probe aluminum plasmas [2.18]. This interferometer still requires good spatial coherence of the source to produce high visibility interferograms but now the lengths of the two arms of the interferometer are compensated so the temporal coherence of the probe beam is not a limiting factor to the visibility.

2.3.2 Amplitude division soft x-ray interferometers

Amplitude division interferometers do not have the limitation on the spatial coherence of the laser source because in principle the two beams can be perfectly superposed, and there is no limitation on the size of the objects that can be probed except for the size of the beams and detectors and the available light. Also the two arms of the interferometer can be perfectly matched, something that doesn't happen in all wavefront division interferometers. The first amplitude division soft x-ray laser interferometry experiment was performed using a Ne-like yttrium 15.5 nm soft x-ray laser pumped by the laboratory size NOVA laser. Da Silva *et al.* demonstrated the technique for plasma diagnostics using an interferometer that utilized Mo-Si thin-film multilayer-coated beam splitters and mirrors mounted in a Mach-Zehnder configuration [2.19], schematically shown in Fig 2.8. The beam splitter's reflectivity and transmission were 15 % and 20 % respectively which, combined with a maximum mirror reflectivity of 60 % gives a throughput of 1.8 % for each arm of the interferometer.

This interferometer was used to probe millimeter scale plasmas at distances as close as $25\ \mu\text{m}$ from the initial target surface where the measured electron density reached $2 \times 10^{21}\ \text{cm}^{-3}$ [2.11]. It was also used to perform studies of the coherence

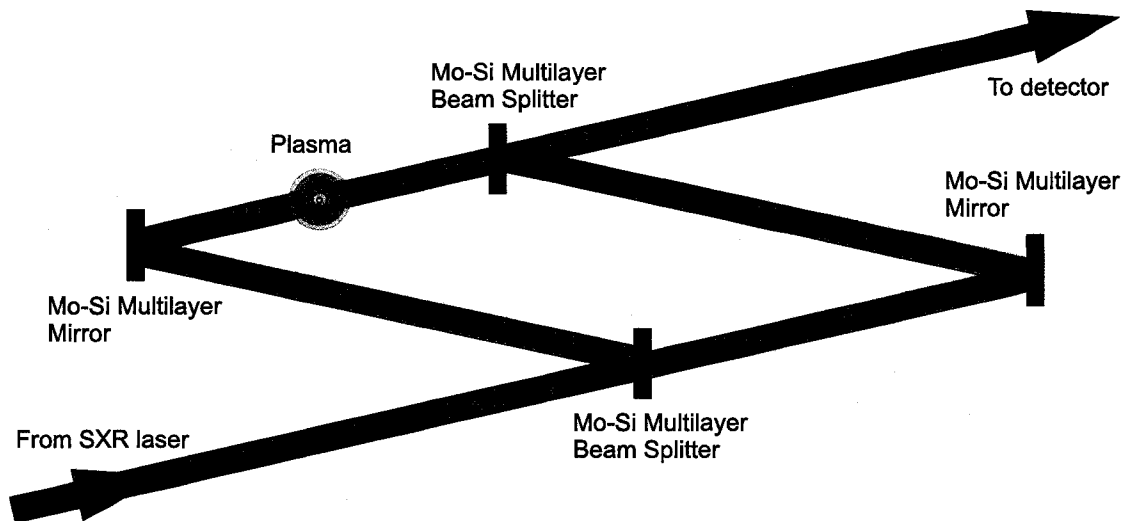


Figure 2.8: Schematic diagram of the Mach-Zehnder interferometer based on thin film beam splitters and used in combination with a neon-like yttrium x-ray laser ($\lambda = 15.5$ nm).

length of the soft x-ray laser [2.20] and of a colliding plasma [2.21]. These experiments were the first to realize soft x-ray interferometry of dense plasmas. However, the low repetition rate of the laboratory size x-ray lasers used and the fragile beam splitters that had to be replaced after every shot limited the amount of data that could be taken. Furthermore, the 200-300 ps pulse duration of the probe laser limits the types of plasmas that can be studied due to the possible blurring of the interference fringes. Another amplitude division interferometer recently developed is a Michelson interferometer based on multilayer foil beam-splitters that provided transmission and reflectivity of 15 % and 14 % respectively. The instrument was used to measure the longitudinal coherence length of the Ni-like Pd 14.7 nm soft x-ray laser [2.22]. The use of this type of instruments is limited to the wavelength range in which low absorption thin film multilayer beam splitters can be manufactured, in particular it is not possible at present time to manufacture thin film beam splitters for operation at 46.9 nm.

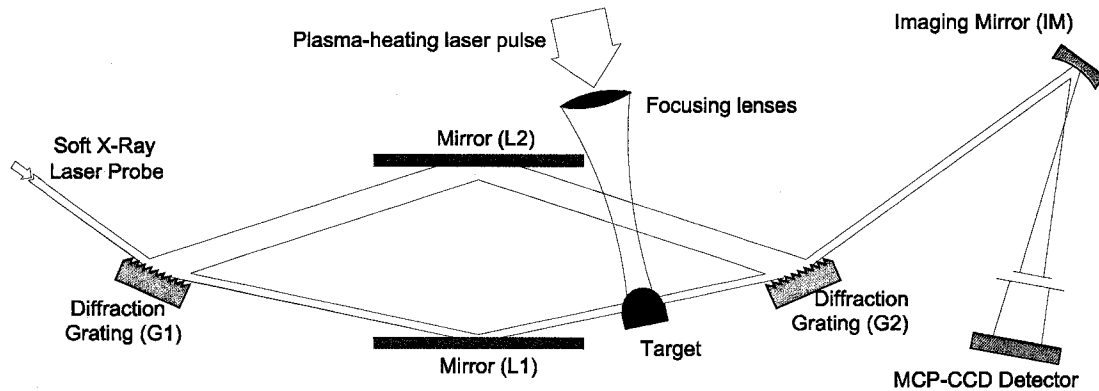


Figure 2.9: Schematic diagram of the Diffraction Grating Interferometer with the target position and the plasma forming beam indicated in the drawing.

2.4 Diffraction Grating Interferometer

The Diffraction Grating Interferometer (DGI) is the solution found for the problem of building an amplitude division soft x-ray interferometer that worked at 46.9 nm wavelength and that was also stable and robust. The interferometer was proposed by Juan Chilla *et al.* [2.23] in two configurations, the first one was designed to perform single shot measurements of the linewidth of soft x-ray lasers and the second one to conduct plasma diagnostics measurements. The narrow bandwidth typical of soft x-ray lasers is difficult to measure because a spectrometer with the required resolution would be very large [2.24], but the resolution can be achieved using interferometric techniques. The linewidth of the laser can be measured with a resolution that surpasses that of regular spectrometers, by measuring the visibility curve. The first configuration of this interferometer permits the measurement of such visibility curves in a single shot of the soft x-ray laser.

The second configuration is the DGI illustrated in Fig. 2.9. This high throughput amplitude division interferometer design can be adapted for operation with any of the presently available saturated soft x-ray lasers. The DGI is set in a skewed Mach-Zehnder configuration. The light incident on the first gold coated diffraction grating (G1) is diffracted with approximately equal intensity in the zeroth and first orders. These two beams that form the two arms of the interferometer are reflected at ~ 2 degrees grazing incidence angle toward a second diffraction grating (G2) using two 35 cm long gold coated mirrors (L1 and L2). Grating G2 recombines the two beams such that they exit the interferometer propagating with a small angular difference, selected to produce fringes of the spacing required by the particular experiment. Two versions of the interferometer were built [2.25, 2.26], the first one, designed to work at 46.9 nm wavelength used 300 l/mm gratings with a blaze angle of 1.33 degrees while the second version designed to work at 14.7 nm wavelength uses 900 l/mm gratings with a blaze angle of 2 degrees [2.27]. The finer ruling of the second interferometer was selected because it provides a more precise blaze angle needed to split the intensity evenly on the zeroth and first orders. The first grating diffracts the beam into zeroth and a first order components of approximately equal intensity when operating at a grazing incidence angle of 11 degrees for the 46.9 nm version and 6 degrees for the 14.7 nm version. For the selected ruling and angle of incidence, the resulting angle between the zeroth and first diffracted orders are 3.6 and 5.2 degrees respectively. This dispersion angle defines the geometry of the interferometer. Thus, with the two gratings separated by ~ 90 cm center-to-center, the resulting distance between the two arms of the interferometer at the target position indicated in Fig. 2.9 is ~ 1.5 cm. There, the phase object of interest, a plasma in the case of these experiments, is placed. The

reflectivity of the gold-coated diffraction gratings is maximized by the small grazing incidence angle used, resulting in an efficiency of 25 % per order on each grating. The long mirror's (L1 and L2) reflectivity is $\sim 90\%$, giving a total throughput for the instrument, excluding the imaging optics, of $\sim 12\%$.

Advantages of the DGI scheme over other amplitude-division soft x-ray interferometers based on thin film beam splitters [2.11, 2.22] include a higher throughput, $\sim 6\%$ per arm compared to $\sim 1.8\%$ or less for thin film beam splitter-based interferometers and a significantly increased resistance of the beam splitters (diffraction gratings) to plasma debris. Moreover, as mentioned above the DGI can also be designed to operate at different soft x-ray wavelengths by choosing gratings with the proper ruling and blaze angle. Two interferometers have produced extensive results both at 46.9 nm and 14.7 nm and a third one is being developed to operate at a shorter wavelength. In contrast, the operation of interferometers based on thin film beam splitters is limited to wavelengths where material absorption is low, which for example excludes their use with the 46.9 nm Ne-like Ar laser.

2.4.1 Alignment of the interferometer

Due to the wavelength-dependent dispersion of the gratings, the alignment of the interferometer cannot, in principle, be performed with an auxiliary optical laser. To overcome this difficulty in the alignment, the diffraction gratings were designed to have two different, vertically separated, ruled sections on the same substrate. The section associated with the alignment had a line spacing chosen to produce the same dispersion on a selected laser diode as the dispersion produced on the soft x-ray laser by its ruled section. From the grating equation, evaluated for the first order, $\sin(i) - \sin(r) = \xi\lambda$, the relation $\xi_{sxr}\lambda_{sxr} = \xi_{al}\lambda_{al}$ is obtained for the soft x-ray laser's and for the alignment laser diode's wavelengths and its

corresponding ruling densities, ξ . This relation is used to select the alignment ruling density, once the alignment wavelength is chosen, or to select the wavelength of the laser diode once the ruling density is chosen. The laser diode chosen [2.28], that works for both interferometers, has a central wavelength of ~ 827 nm and an estimated coherence length of ~ 300 μm . This wavelength determines the line density of the alignment ruling to be 16 lines/mm for the 14.7 nm version of the DGI and 17 lines/mm for the 46.9 nm version. The temporal coherence length of the laser diode was chosen to be similar or shorter than the coherence length of the soft x-ray laser used (200–400 μm 1/e half-width) [2.22, 2.25]. This ensures that, once aligned with the auxiliary laser diode, the arm lengths of the interferometer are matched with sufficient precision to warrant the observation of fringes with the soft x-ray lasers.

The 14.7 nm gratings have a central region with 900 lines/mm for the soft x-ray laser radiation, and two other regions situated on top and below with 16 lines/mm rulings to be used with the infrared laser diode. This 3-stripe ruling design allows to orient the second grating with a reversed blaze angle direction that is needed to recombine the two soft x-ray laser beams with equal intensities.

The gratings were ruled on a 58 mm \times 58 mm substrate for the 46.9 nm version of the interferometer and on an 85 mm long \times 76 mm tall substrate for the 14.7 nm version of the interferometer. The ruled gratings were then used to generate replicas that were gold coated. In this way many replicas can be generated from the same master grating, reducing the total cost. The region used for the soft x-ray laser was at least 20 mm tall, but only a small portion of this was used because of the small size of the soft x-ray beam. The gratings were manufactured by Hyperfine Inc. [2.27] and by Bach Research Inc. [2.29] respectively.

The initial alignment of the interferometer is done using a visible laser as a reference for the position of the soft x-ray laser beam. Because the method of generating the soft x-ray laser is completely different for the two probe lasers, different approaches have been used. To align the 46.9 nm capillary discharge laser through the interferometer, the alumina capillary is replaced with a red laser diode that is then aligned to follow the entrance path on the interferometer while to align the 14.7 nm laser, a He-Ne laser is aligned so it grazes the (soft x-ray laser) target through the output path of the laser and into the entrance path of the interferometer. Then, this visible beam is steered with G1, L1 and G2 along the zero order arm into the detector. To perform the first order alignment the coarser secondary ruling is used together with the ~ 827 nm IR laser diode. The vertical offset between the IR alignment laser diode and the soft x-ray laser is kept to a minimum (≤ 1 cm) to reduce differences in the path caused by the vertical tilt of the optics. The IR alignment beam is then steered along the zero order path using two Al-coated mirrors, to set the correct incidence angle on the first grating. Then, the first diffracted order beam is adjusted using L2, to follow the first order arm of the interferometer. Final corrections of L2 and G2 are made until the fringes are clearly observed at the output of the DGI and the output beams (zero and first orders) are collinear. At this stage of the alignment, the orientation (vertical or horizontal) of the fringes can be set. Also, for its use in plasma diagnosis, it is usually advantageous to assure that the angle between the output beams is such that a plasma set on the zero order beam will produce fringe shifts away from the target. This facilitates the interpretation of the fringe shifts for the determination of the electron density profile.

Because it is difficult to obtain a consistent blaze profile on very small groove densities, the IR ruling is effectively not blazed. As a result, most of the IR energy is

diffracted onto the zero order, creating a large intensity difference between the two arms of the DGI, when aligning. This prevents the fringes from the IR alignment laser to be observed at the output of the DGI. However the first diffracted order off the second grating can be used, instead, for this purpose. In this case, the intensity of both arms of the interferometer is similar because each undergoes a reflection (zeroth order) and a first order diffraction. As the optimum alignment can differ slightly from that obtained with the IR beam the final adjustments are conducted under vacuum with the soft x-ray laser beam, utilizing motorized actuators to control the position of the relevant optics. It was discovered that motorizing some of the components was more important than others and, since vacuum compatible actuators can be expensive, it is wise to only motorize the essential motions. For example, it was found that there is no need to motorize G1, the first diffraction grating. In case of discovering that the first grating needs readjustment it is a lot more time efficient to break vacuum and realign the whole setup using the auxiliary alignment beam than to try to correct the alignment of the whole setup with vacuum actuators. In contrast, the translations of L1 and L2 are important, and it is useful to have these axes encoded since they provide control of the overlap between the beams of the two arms, and also, they can be used to displace either the first or zero order beams out of the path to examine them independently. The horizontal and vertical tilt of L2 and G2 are used very frequently to orient the fringes and to select the desired fringe spacing. L1 vertical and horizontal tilts are used but not as often as those on L2. The translation of G2 is also used but less frequently. It is important to have the imaging mirror translation motorized to be able to adjust the focus and produce a sharp image of the target on the detector. The horizontal and vertical tilt of both this mirror and the relay mirror

(L3) are used to steer the beam onto the detector (see Fig. 2.10), but it is possible to operate with only adjusting the relay mirror tilt, if it is found that only small corrections are required and a very careful pre-alignment is performed.

For the case of the 14.7 nm interferometer, some extra tools were used to simplify the alignment procedure through feedback on the pointing of the soft x-ray laser into the interferometer. The combination of a CCD camera placed inside the DGI chamber with flip-in Mo-Si mirrors allowed the monitoring of the soft x-ray laser beam position at the input and at the output of the interferometer (see Fig. 2.10) to compare it with the preregistered position of the He-Ne laser used during the prealignment. The low magnification ($8.5 \times$) of the optics used to image the output of the interferometer allowed the simultaneous monitoring of the complete beams corresponding to the two arms of the interferometer. This is invaluable when trying to perform a final alignment of the DGI as it provides information on the overlap of the two beams and shows the intensity distribution with regions of different fringe quality.

2.4.2 Detector systems

Two similar detection systems were used to capture and digitize the interferograms in the two interferometers. The detector used in the 46.9 nm experiments employs a Multi-Channel-Plate (MCP) combined with an image intensifier and a Coupled Charge Device (CCD) camera. The MCP converts the incident photons to electrons that get multiplied as they traverse the plate. The electrons generate light, as they hit a P20 (ZnCdS:Ag) phosphorous screen, that is then imaged with the CCD detector. The use of a MCP in the detection setup has the advantage of not needing a CCD camera sensitive to soft x-ray radiation (more expensive back thinned CCD), since the light emitted by the phosphorous screen is in the

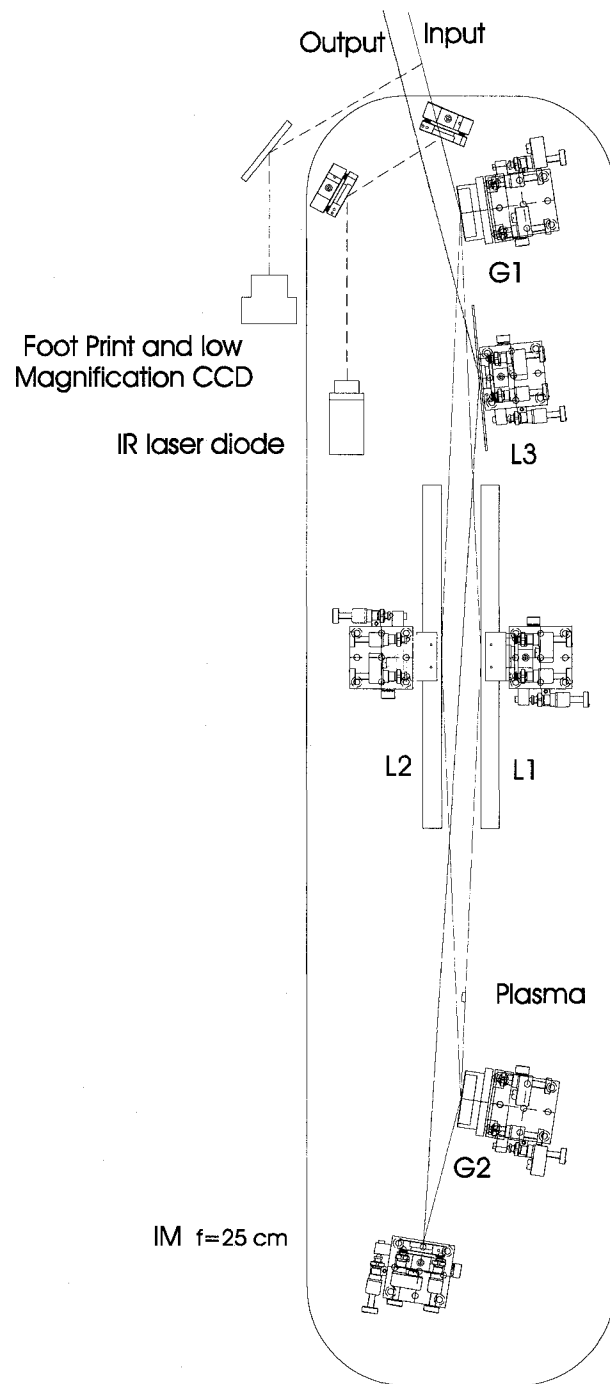


Figure 2.10: Position of the Low magnification and Foot print camera used to facilitate the alignment in the 14.7 nm version of the DGI. The flip mirrors were placed at the position where the output and input beams intercept the dashed line.

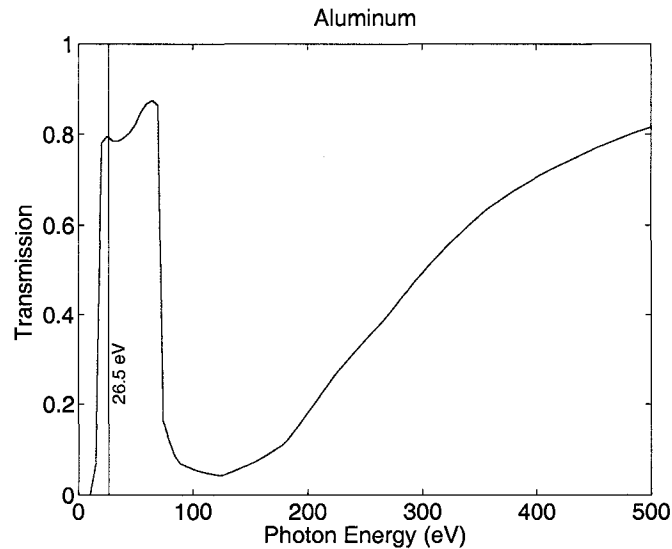


Figure 2.11: Transmission curve for 1000 Å Al filter that can be used to block the stray light and plasma self emission from reaching the CCD camera. The transmission was obtained from the Lawrence Berkely Laboratory tool available at: <http://www.cxro.lbl.gov>.

visible region of the spectrum. Another advantage is that the MCP can be used to discriminate the short laser probe pulse from the longer plasma background radiation. To do this, the MCP is biased using a ~ 4 ns pulse that limits the gain to those few ns effectively temporally filtering the detection. Also, the MCP's detection efficiency drops for longer wavelengths, effectively working as a filter of background light.

The MCP is an array of hexagonal channels, in this case $25 \mu\text{m}$ in size and separated from center to center by $32 \mu\text{m}$ with a 45% open area. For the case of this experiment, if the plate is biased to 1000 V, the light from the 1 ns laser pulse would generate a current that is too high, and would saturate the MCP. So the MCP were operated at lower voltages, < 700 V, in its linear range and below this saturation. To obtain enough light on the CCD camera, an image intensifier was needed to amplify the low light from the phosphorous screen. The image intensifier

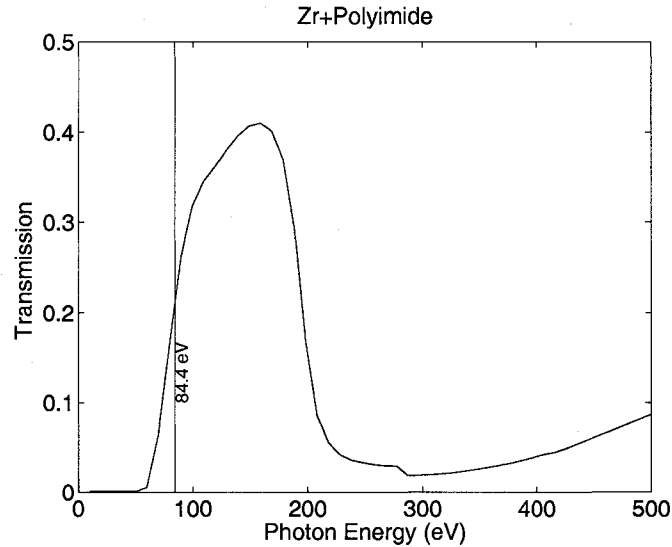


Figure 2.12: Transmission curve for \AA Zr + 1000 \AA polyimide ($C_{22}H_{10}N_2O_5$) filter used to block the stray light and plasma self emission from reaching the CCD camera. The transmission was obtained from the Lawrence Berkely Laboratory tool available at: <http://www.cxro.lbl.gov>.

doesn't saturate because the 1 ns pulse on the MCP is spread to milliseconds by the P20 phosphorous screen.

A disadvantage of this setup is an overall reduction in the resolution of the imaging system by the addition of the MCP and the image intensifier. It is possible to operate the system with a backthinned CCD that is sensitive to the 26.5 eV radiation. In this case a filter has to be used to reduce the amount of background radiation from the plasma and from the plasma heating pulse. An aluminum filter is suitable for this, as it has a bandpass around 26.5 eV, as show in Fig. 2.11. This was the mode of operation of the detector system for the 14.7 nm version of the interferometer. A Princeton Instruments CCD camera [2.30] was used straight in the path of the beam. The CCD has a $1.33 \times 1.33 \text{ cm}^2$ sensor with 1024×1024 pixels of $13 \times 13 \text{ }\mu\text{m}^2$ size. To limit the light coming from the plasma-forming

laser and from the plasma itself a 2000 Å Zr + 1000 Å polyimide ($C_{22}H_{10}N_2O_5$) filter was used with good transmission at 84.4 eV (Fig.2.12).

2.4.3 Proof of principle experiments

The first plasma probing experiments done with the interferometer studied a line focus laser-created copper plasma. The interferometer used is shown in Fig. 2.13. The probe laser was the 46.9 nm capillary discharge laser described in detail in section 1.4.1. The plasma was generated by focusing the beam of a $\lambda = 1064$ nm Nd:YAG laser (using a 30 cm focal length cylindrical lens and a 10 cm focal length spherical lens) in a 2.7 mm long and 30 μ m wide line focus onto a polished electrolytic copper target placed in the zero order arm of the interferometer.

The firing of the soft x-ray laser probe beam was synchronized with respect to the Nd:YAG laser by using a common master clock and appropriate delays. However, since the jitter in the firing of the soft x-ray laser was significant ($\sim 15 - 30$ ns) nearly 100 shots per series were required to completely map the ~ 35 ns long plasma evolution with ~ 1 ns resolution.

To reduce the plasma self-emission that affects the visibility of the fringes, the high degree of collimation of the soft x-ray laser beam was exploited by utilizing a set of pinholes ~ 1 mm in diameter, that significantly reduced the amount of plasma radiation collected by the detector. The pinhole farther from the target limits the plasma self emission collection angle while the slightly smaller one, closest to the target, limits the size of the coherent laser beam to prevent diffraction effects from the second pinhole. On top of this, the MCP was gated whenever it was necessary, with a ~ 4 ns pulse to collect only a fraction of the plasma light.

The imaging optics for this experiment consisted of a 25 cm focal length Si/Sc multilayer spherical mirror [2.31], set at 5 degrees off normal incidence, followed

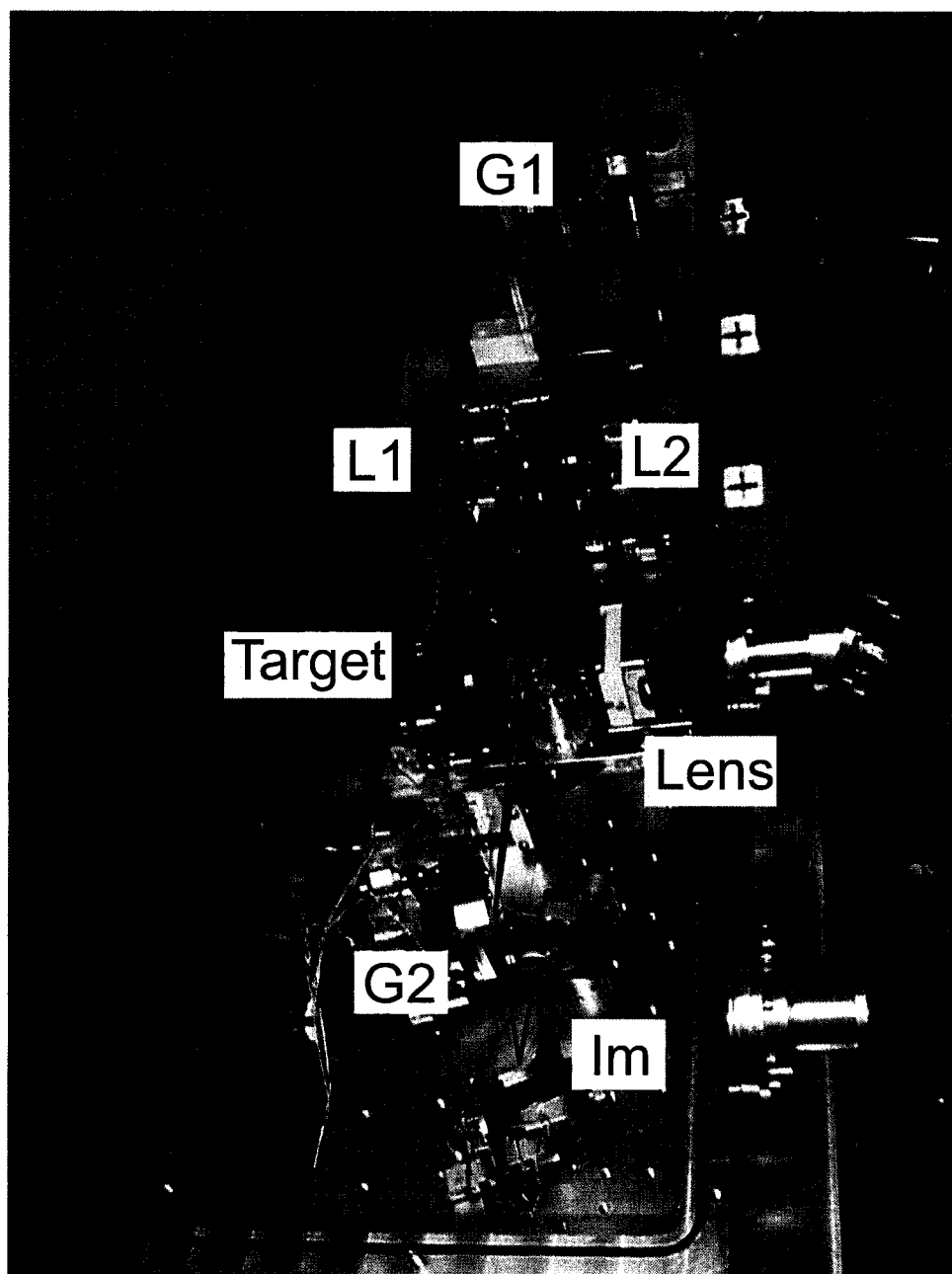


Figure 2.13: Photograph of the Diffraction Grating Interferometer used in the first experiments with the 46.9 nm probe laser.

by a flat Si/Sc multilayer mirror used to relay the laser beam to the MCP/CCD detector setup located ~ 6.5 meters away from the plasma. The CCD used was a Princeton Instruments SX-TE/TEK-1024-TKB with 1024×1024 pixels in a 1 inch square sensor. This imaging setup has a total magnification of $25 \times$ that was measured by imaging a calibrated mesh placed at the target plane position. This magnification includes the magnification produced by the image intensifier. This means that a single CCD pixel is equivalent to $1 \mu\text{m}$ at the object plane.

The plasma probing results obtained with the diffraction grating interferometer are shown in Fig. 2.14. The expected evolution of the plasma is observed in these interferograms, with a cylindrical expansion and a subsequent cooling down and recombination of the plasma, which is evident by the absorption of the probe beam close to the target. The maximum electron density measured in these experiments was $5 \times 10^{19} \text{ cm}^{-3}$ at locations about $25\text{-}30 \mu\text{m}$ from the target surface. Ray tracing calculations using the measured profile indicate that a 266 nm probe would be deviated completely outside of the plasma, preventing any density measurement.

The factors that contribute to limit the maximum density that can be measured in a plasma probing experiment are greatly reduced but still present in soft x-ray interferometry. Refraction in a 2.7 mm long plasma, close to the target surface, is the most probable cause for not being able to measure higher densities in the data of Fig. 2.14. This is addressed in the next chapter where different plasma geometries were probed.

2.5 Picosecond resolution plasma probing

Another factor that limits the density that can be measured is the temporal resolution due to the pulse duration of the probe beam. The first amplitude

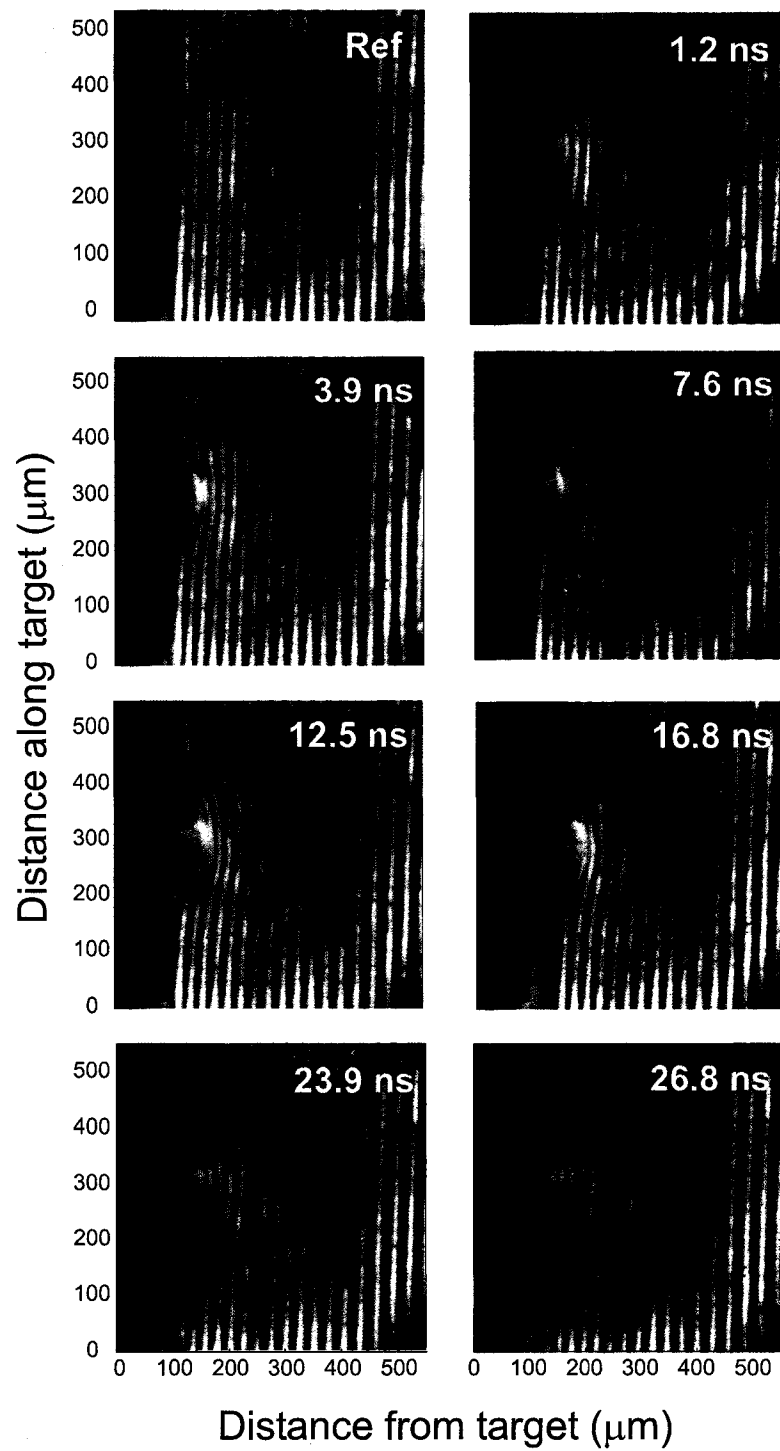


Figure 2.14: Sequence of interferograms depicting the evolution of a copper plasma.

division soft x-ray laser interferometer, demonstrated by Da Silva *et al.* [2.19], used 200–300 ps long probe pulses, while the first demonstration of the Diffraction Grating Interferometer used 1 ns pulses. These relatively long pulses make the interferograms susceptible to the blurring of the interference fringes which results from the rapid local variations of the electron density within a fast moving plasma, during the exposure time given by the probe beam. While these pulse widths are adequate for mapping the density of numerous slowly evolving dense plasmas, such as pulse-power plasmas and laser-created plasmas far from the target surface, it precludes their use in diagnosing plasmas where fast evolving steep density gradients lead to blurring of the fringes, as is the case for laser-created plasmas probed close to the target surface.

The problem arises when the plasma being probed varies significantly within the “integration time” of the probe beam, which can result in a blurring effect in those regions of the plasma. As an example of this effect, Fig. 2.15 shows two simulated interferograms, both using density maps obtained from LASNEX simulations, a hydrodynamic code used to model high density plasmas. The plasma simulated is similar to the ones studied with this interferometer and presented later in this work and was generated with an irradiation intensity of $\sim 10^{12} \text{ Wcm}^{-2}$. Two cases are shown for two different probe beam widths. The 500 ps probe beam interferogram clearly shows that the interference fringes are blurred in the region where dense plasma is present. The most notorious blurring occurs close to the target surface, near the heating beam’s critical density where the fringes get washed out and information is lost. But further away from the target, between $60 \mu\text{m}$ and $100 \mu\text{m}$, the presence of forking of the fringes, that at first glance seem to be only slightly affected, prevents density measurements where the dense plasma is present.

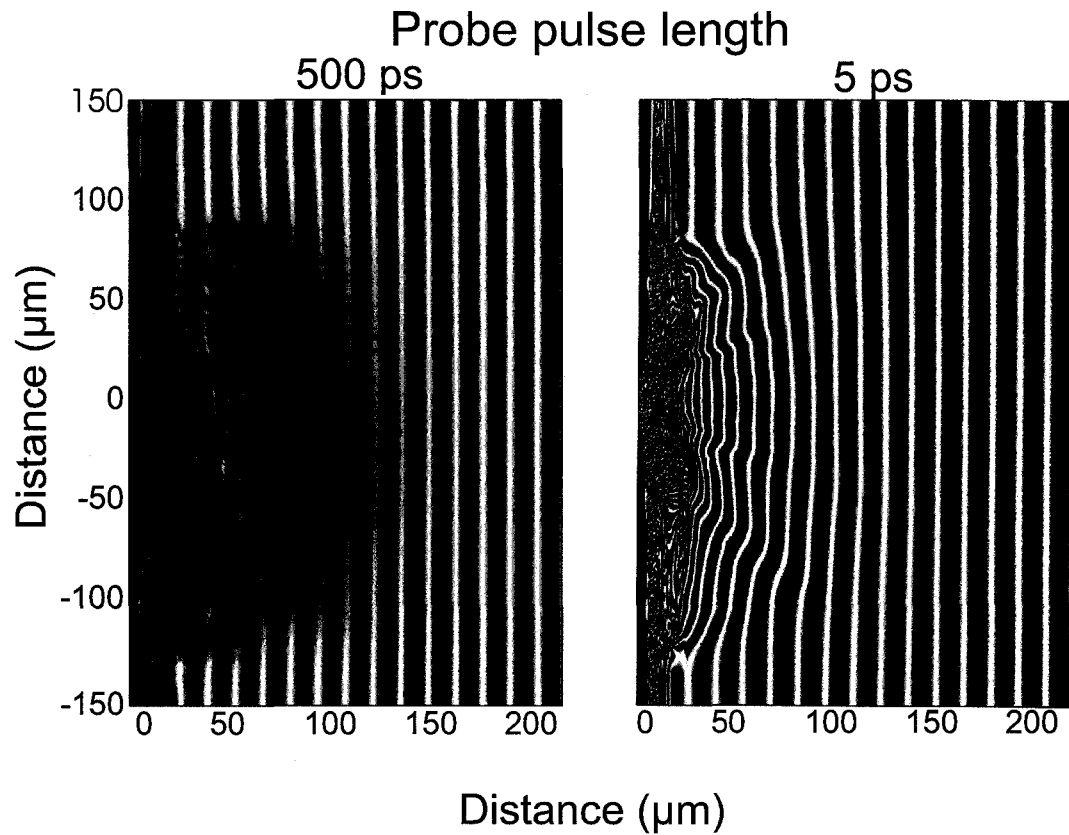


Figure 2.15: Two synthesized interferograms created by averaging a LASNEX simulated plasma evolving over 500 ps and 5 ps respectively. The structure observed on the 500 ps interferogram, for example fringes that bifurcate, is due to the averaging over a changing plasma.

On the other hand, the advantage of using a short probe beam is clearly evident from the 5 ps interferogram. Here the fringes are visible and distinguishable up to the region where the detector resolution plays a determinant role.

To demonstrate soft x-ray laser interferometry with picosecond resolution the DGI was combined with a transient 14.7 nm Ni-like Pd soft x-ray laser described in section 1.4.2. This setup combines the advantages of soft x-ray interferometry described earlier in this chapter with a reduced motion blurring due to the picosecond pulse. The 14.7 nm laser pulse duration has been measured to be between 4.5 ps and 5.9 ps [2.32], and a pulse profile is shown in Fig. 1.7 in the previous chapter. The combination of the DGI with this laser is capable of measuring plasmas with fast evolving and very steep density profiles very close to the target surface. Results obtained using this setup will be shown in the next two chapters and constitute the first picosecond resolution soft x-ray laser interferometry experiments.

2.6 Conclusions

The power of interferometry as a plasma diagnostic technique resides in its ability to generate detailed maps of the electron density without, in most cases, having to rely on modeling as other techniques do. To be able to do this the probe beam has to not be affected by refraction and absorption that would otherwise make the measurement less direct. Soft x-ray probe beams are suitable to probe plasmas because all these effects are greatly reduced with a reduction of wavelength and also their high brightness and narrow bandwidth help overcome the strong plasma self emission. Some interferometers that had been constructed either used wavefront division schemes, or relied on fragile thin film beam splitters to construct an amplitude division soft x-ray interferometer, that had a low total throughput.

The Diffraction Grating Interferometer design, that uses diffraction gratings as beam splitters, results in a robust setup that is very well suited for plasma diagnostics. Two versions of the interferometer were successfully constructed to work in combination with soft x-ray lasers operating at two different wavelengths (46.9 nm and 14.7 nm) and that have two different pulse durations (1 ns and 5 ps) and tested with excellent fringe visibility over a large area, that permit probing of large scale high density plasmas. These two interferometry setups have produced a large amount of data, probing plasma densities up to a few μm away from the target surface and to densities that are very close to the heating beam critical density: $\sim 1 \times 10^{21} \text{ cm}^{-3}$, as will be shown in the next 2 chapters.

Several hundred plasma shots were performed in one case (14.7 nm) with plasma heating laser energies of up to 150 J and thousands in the other (46.9 nm) with plasma heating laser pulses of the order of 1 J, without any serious damage or deterioration on the image quality. Densities up to $4.5 \times 10^{20} \text{ cm}^{-3}$ were measured at distances as short as $2 \mu\text{m}$ from the target in different types of millimeter size line focus laser-created plasmas.

The diffraction grating interferometer is scalable to significantly shorter wavelengths, and constitutes a promising scheme for extending interferometry to the study of very dense plasmas such as those investigated for inertial confinement fusion.

Bibliography

- 2.1 I. H. Hutchinson. *Principle of Plasma Diagnostics*. Cambridge University Press, 2002.
- 2.2 T.P. Hughes. *Plasma and Laser Light*. John Wiley and Sons, New York, 1975.
- 2.3 R. A. Jeffries. Two-wavelength holographic interferometry of partially ionized plasmas. *Physics of Fluids*, 13(1):210–212, 1970.
- 2.4 R. A. London. Beam optics of exploding foil plasma X-ray lasers. *Physics of Fluids*, 31:184–192, January 1988.
- 2.5 C.J. Tallents, M.D.J. Burgess, and B. Luther-Davies. The determination of electron density profiles from refraction measurements obtained using holographic interferometry. *Optics Communications*, 44(6):384–387, 15 February 1982.
- 2.6 R. F. Smith, J. Dunn, J. Nilsen, J. R. Hunter, V. N. Shlyaptsev, J. J. Rocca, J. Filevich, and M. C. Marconi. Refraction effects on x-ray and ultraviolet interferometric probing of laser-produced plasmas. *Journal of the Optical Society of America B: Optical Physics*, 20(1):254–259, 2003.

- 2.7 R.M. More. *Physics of Laser Plasmas*, volume 3, chapter 2, pages 91–100. North Holland.
- 2.8 C.W. Allen. *Astrophysical Quantities*, page 100. Oxford University Press, 1963.
- 2.9 R.S. Craxton, F.S. Turner, R. Hoefen, C. Darrow, E.F. Gabl, and G. E. Busch. Characterization of laser-produced plasma density profiles using grid image refractometry. *Physics of Fluids B*, 5(12), 1993.
- 2.10 M. Born and E. Wolf. *Principles of Optics*, chapter Elements of the theory of diffraction, pages 412–516. Cambridge University Press, Cambridge, UK. 7th edition.
- 2.11 L. B. Da Silva, T. W. Barbee Jr., R. Cauble, P. Celliers, D. Ciarlo, S. Libby, R. A. London, D. Matthews, S. Mrowka, J. C. Moreno, D. Ress, J.E. Trebes, A. S. Wan, and F. Weber. Electron density measurements of high density plasmas using soft x-ray laser interferometry. *Physical Review Letters*, 74(20):3991, 1995.
- 2.12 M. Born and E. Wolf. *Principles of Optics*, chapter Elements of the theory of interference and interferometers, pages 286–411. Cambridge University Press, Cambridge, UK. 7th edition.
- 2.13 J. J. Rocca, C. H. Moreno, M. C. Marconi, and K. Kanizay. Soft-x-ray laser interferometry of a plasma with a tabletop laser and a Lloyd’s mirror. *Optics Letters*, 24(6):420–422, 1999.
- 2.14 C. H. Moreno, M. C. Marconi, K. Kanizay, J. J. Rocca, Y. A. Uspenskii, A. V. Vinogradov, and Y. A. Pershin. Soft-x-ray laser interferometry of a

- pinch discharge using a tabletop laser. *Physical Review E*, 60(1):911–917, 1999.
- 2.15 F. Albert, D. Joyeux, P. Jaegle, A. Carillon, J. P. Chauvineau, G. Jamelot, A. Klisnick, J. C. Lagron, D. Phalippou, D. Ros, S. Sebban, and P. Zeitoun. Interferograms obtained with an x-ray laser by means of a wavefront division interferometer. *Optics Communications*, 142:184–188, 1997.
- 2.16 Ph. Zeitoun, F. Albert, P. Jaegl, D. Joyeux, M. boussoukaya, A. Carillon, S. Hubert, G. Jamelot, A. Klisnick, D. Phalippou, J.C. Lagron, D. Ros, S Sebban, and A. Zeitoun-Fakiris. Investigation of strong electric-field induced surface phenomena by xuv laser interferometry. *Nuclear Instruments and Methods in Physics Research A*, 416:189–191, 1998.
- 2.17 D. Joyeux, R. Mercier, D. Phalippou, M. Mullot, and M. Lamare. Design and realization of an interferometric microimaging system working in the EUV range. *J. Phys. IV France*, 11(2):511, 2001.
- 2.18 H. Tang, O. Guilbaud, G. Jamelot, D. Ros, A. Klisnick, D. Joyeux, D. Phalippou, M. Kado, M. Nishikino, M. Kishimoto, K. Sukegawa, M. Ishino, K. Nagashima, and H. Daido. Diagnostics of laser-induced plasma with soft X-ray (13.9 nm) bi-mirror interference microscopy. *Applied Physics B: Lasers and Optics*, 78:975–977, 2004.
- 2.19 L. B. Da Silva, T. W. Jr. Barbee, R. Cauble, P. Celliers, J. C. Moreno, J. E. Trebes, Wan A. S., and F. Weber. Extreme-ultraviolet interferometry at 15.5 nm using multilayer optics. *Applied Optics*, 34(28):6389, 1995.

- 2.20 P. Celliers, F. Weber, L. B. da Silva, T. W. Barbee, Jr., R. Cauble, A. S. Wan, and J. C. Moreno. Fringe formation and coherence of a soft-x-ray laser beam illuminating a Mach-Zehnder interferometer. *Optics Letters*, 20:1907–1909, September 1995.
- 2.21 A. S. Wan, T. W. Barbee, R. Cauble, P. Celliers, L. B. Da Silva, J. C. Moreno, P. W. Rambo, G. F. Stone, J. E. Trebes, and F. Weber. Electron density measurement of a colliding plasma using soft-x-ray laser interferometry. *Physical Review E*, 55(5):6293–6296, 1997.
- 2.22 R. F. Smith, J. Dunn, J. R. Hunter, J. Nilsen, S. Hubert, S. Jacquemot, C. Remond, R. Marmoret, M. Fajardo, P. Zeitoun, and L. Vanbostal. Longitudinal coherence measurement of a transient collisional x-ray laser. *Optics Letters*, 28(22):2261–2263, 2003.
- 2.23 J. L. A. Chilla, J. J. Rocca, O. E. Martinez, and M.C. Marconi. Soft x-ray interferometer for single-shot laser linewidth measurements. *Optics Letters*, 21(13):955–957, 1996.
- 2.24 M. C. Hettrick, J. H. Underwood, P. J. Batson, and M. J. Eckart. Resolving power of 35,000 (5 mA) in the extreme ultraviolet employing a grazing incidence spectrometer. *Applied Optics*, 27:200–203, January 1988.
- 2.25 J. Filevich, K. Kanizay, M. C. Marconi, J. L. A. Chilla, and J. J. Rocca. Dense plasma diagnostics with an amplitude-division soft-x-ray laser interferometer based on diffraction gratings. *Optics Letters*, 25(5):356–358, 2000.
- 2.26 J. Filevich, J. J. Rocca, M. C. Marconi, R. F. Smith, J. Dunn, R. Keenan, J.R. Hunter, S.J. Moon, J. Nilsen, A. Ng, V. N. Shlyaptsev, and T. W. Barbee.

Picosecond resolution soft x-ray laser plasma interferometry. *Applied Optics*, 43(19), July 2004.

2.27 Hyperfine Inc. 4946 North 63th St. Boulder, CO 80301.

2.28 Laser Diode SDL-5401-GL by SDL (JDS Uniphase) www.jdsu.com.

2.29 Bach Research Inc. 2200 Central Avenue Suit D. Boulder, CO 80301 - www.bachresearch.com.

2.30 Princeton Instruments PI-SX:1k. Roper Scientific, Inc. 3660 Quakerbridge Road. Trenton, NJ 08619.

2.31 Y. A. Uspenskii, V. E. Levashov, A. V. Vinogradov, A. I. Fedorenko, V. V. Kondratenko, Y. P. Pershin, E. N. Zubarev, and V. Y. Fedotov. High-reflectivity multilayer mirrors for a vacuum-ultraviolet interval of 35-50 nm. *Optics Letters*, 23:771, 1998.

2.32 J. Dunn, R. F. Smith, R. Shepherd, R. Booth, J. Nilsen, J. R. Hunter, and V. N. Shlyaptsev. Temporal characterization of a picosecond laser-pumped x-ray laser (for applications). In E. E. Fill and S. Suckewer, editors, *SPIE Int. Soc. Opt. Eng. Proc*, volume 5197, pages 51-59, 2003.

Chapter 3

**TWO DIMENSIONAL EFFECTS IN LASER
CREATED PLASMAS**

Shortly after their invention, lasers have been used to create plasmas by irradiating different target materials [3.1]. These plasmas permitted the study in the laboratory of dense plasma regimes and the conception of new applications. Some examples are the study of space plasmas and plasmas related to astrophysical phenomena in the laboratory [3.2], the use of laser-created plasmas for the generation of short wavelength light for applications like lithography [3.3], the generation of x-ray lasers from laser-created plasmas [3.4], the acceleration of charged particles [3.5] and the creation of plasma conditions in which thermo nuclear fusion occurs [3.6].

For the development and improvement of the applications listed above it is important to better understand the processes involved in the formation and evolution of laser-created plasmas. When the heating laser beam is wide relative to the plasma size, the evolution of the plasma can be considered to be one dimensional, and lateral expansion or lateral heat transport can be neglected. If the plasma is created with a narrow heating laser beam, the plasma will expand in a cylindrical two-dimensional way that in some cases can still be approximated as a radial one-dimensional expansion, but that in general is two-dimensional, and that is conventionally known to result in electron density distributions with maximum density along the axis of the irradiation beam. However, in plasmas generated with high irradiation intensities the ponderomotive force has been observed to cause a density depression or cavity in the electron density profile. For example Attwood *et al.* [3.7] showed this effect in plasmas created by irradiating 40 μm diameter SiO_2 glass microballoons and 50-300 μm diameter glass and Parylene disks with an intensity of $\sim 0.3 - 3 \times 10^{14} \text{ Wcm}^{-2}$. This 266 nm probe interferometry

experiments showed a change in concavity of the interference fringes in the sub-critical region that is indicative of a density depression, even more evident after the needed Abel inversion is performed to obtain the three dimensional electron density profile. Density depressions induced by the ponderomotive force have also been observed in numerous other high-intensity laser experiments, in agreement with simulations. Some of the most recent studies include the formation of plasma channels and laser-hole boring in underdense and overdense plasmas motivated by the fast ignitor concept in inertial confinement fusion [3.8,3.9]. These experiments involved laser intensities of $1.7 \times 10^{15} \text{ Wcm}^{-2}$ and $2 \times 10^{17} \text{ Wcm}^{-2}$ respectively. In addition, for several cases involving short laser pulses the saturation of the heat flux, refraction, or channeling of the laser radiation due to relativistic self-focusing at ultrahigh fluxes are found to be responsible for density suppression [3.10,3.11].

In experiments performed using the Diffraction Grating Interferometer together with the capillary discharge soft x-ray laser, an on-axis density depression was observed in a plasma generated at much lower intensity levels (as low as 10^{11} Wcm^{-2}) than those in previous publications. The observed two-dimensional effects cannot be explained by the ponderomotive force, the effects of laser radiation refraction, electron heat saturation, nor the influence of plasma instabilities. The case observed is different, yet universal enough to exist in a wide parameter space. Hydrodynamic model simulations show that this strong two-dimensional behavior is essentially a universal phenomenon that is the result of plasma radiation induced mass ablation and cooling in the areas surrounding the focal spot. In fact, in retrospect, evidence of these effects may be inferred from published visible laser plasma interferograms mapping plasmas with much smaller electron densities, of the order of $\sim 10^{18} \text{ cm}^{-3}$ [3.12–3.14]. However, this kind of two-dimensional

plasma behavior was not clearly revealed from the data nor was it understood. One reason for this is that the effect was not as evident in these previous studies as it is in the results presented in this work. In the results presented in this chapter this two-dimensional effect is distinctively uncovered by the advantages of a reduced refraction, absorption and number of fringe shifts that a soft x-ray laser probe provides when probing dense, large scale laser-created plasmas.

The next section describes results of a study of line focus laser-created plasmas irradiated using a 13 ns long laser pulse and their interpretation using hydrodynamic simulations. The simulations predict that the effect should be present in plasmas irradiated by tightly focused laser beams. In fact, the next three sections describe experiments where two-dimensional effects are observed under different conditions. They correspond to a line focus laser-created plasma irradiated by both a long laser pulse (~ 13 ns) and a short laser pulse (600 ps) and the other to a point focus laser-created plasma irradiated by a long pulse (~ 13 ns).

3.1 Two Dimensional effects in copper line-focus plasmas

The proof of principle experiments that demonstrated the feasibility of the combination of the Diffraction Grating Interferometer with the capillary discharge soft x-ray laser to perform plasma diagnostic experiments is described in section 2.4.3. These experiments probed laser-created plasmas produced by focusing a 360 mJ, $\lambda=1064$ nm laser beam onto a copper slab target . The $30 \mu\text{m}$ wide \times 2.7 mm long line focus resulted in an intensity of $3.4 \times 10^{10} \text{ Wcm}^{-2}$). The results of these experiments (Fig. 2.14) demonstrated that this setup was capable of exploring plasma conditions inaccessible to longer probe wavelengths [3.15]. The expected evolution of the plasma is observed in these interferograms, with a cylindrical

expansion and a subsequent cooling and recombination of the plasma, which is evident by the absorption of the probe beam close to the target. The maximum electron densities measured in these experiments ($5 \times 10^{19} \text{ cm}^{-3}$ about 25-30 μm from the target surface.) are lower than the theoretical limit of the plasma density that can be probed using a 46.9 nm probe. Higher electron densities were not measured most likely because very steep plasma density gradients in a 2.7 mm long plasma causes excessive refraction for the 46.9 nm probe to travel unaltered in the region very close to the target. Steep density gradients are present in the plasma since at the target surface the plasma has a density that is very close to the solid density ($9 \times 10^{24} \text{ cm}^{-3}$ for the case of copper) with the density rapidly falling with distance away from the target. In the case of the copper plasma investigated, the plasma density falls ~ 3 orders of magnitude in the first $\sim 30 \mu\text{m}$. This can also be seen from the simple model of a freely expanding plasma [3.16], that yields an exponential density profile $n(x)$.

$$n(x) = n_0 e^{(-\frac{x}{C_s t})} \quad (3.1)$$

where n_0 , is the density at the wall, $C_s = (\frac{Z T_e}{M})^{\frac{1}{2}}$ is the ion sound velocity, T_e is the electron temperature, Z the ion charge and M the ion mass.

To be able to successfully probe plasmas with higher electron densities the length of the line focus was reduced from 2.7 mm to 1.8 mm while keeping the same width of 30 μm . At the same time the energy of the heating laser beam was increased to 630 mJ with the intention of ablating more material from the target and creating an overall denser plasma further away from the target surface where the gradients are smaller. This corresponds to an increase in the intensity of the laser beam on target to $\sim 9 \times 10^{10} \text{ Wcm}^{-2}$.

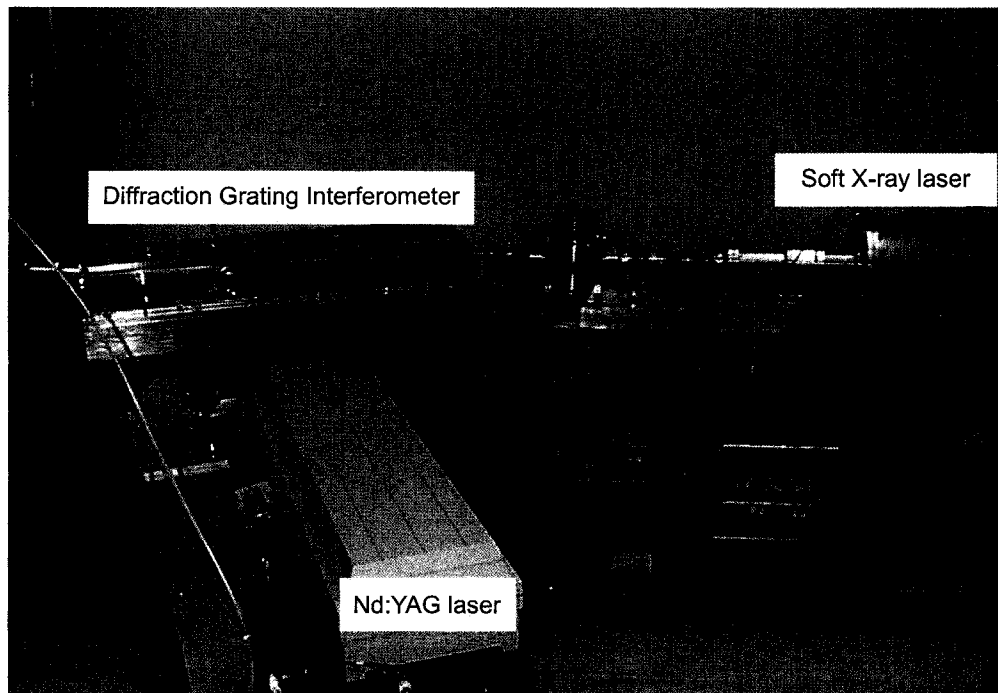


Figure 3.1: Picture of the experimental setup used, that includes the Diffraction Grating Interferometer, the capillary discharge soft x-ray laser and the plasma forming Nd:YAG laser.

The experimental setup consisting of the Diffraction Grating interferometer, the probe Capillary Discharge Soft X-Ray Laser, and a commercial $\lambda=1064$ nm YAG laser (Quanta Ray GCR-190) is shown in Fig. 3.1. The target was a polished solid electrolytic copper slab 4 mm long. The heating and probe lasers were synchronized by running the whole experiment from a master clock. The inherent jitter of the soft x-ray laser (up to 50 ns) was used to change the delay between the pump and probe beams. The timing was measured by simultaneously recording the signal of a photodiode that captured a reflection of the YAG laser before it entered the interferometer and the current signal produced by a Rogowsky coil at the output of the soft x-ray laser. Figure 3.2 shows a series of interferograms that depict the evolution of the copper laser-created plasmas. The interferograms correspond to successive shots all performed under the same conditions. The times shown are measured from the beginning of the 13 ns pump beam. Up to 4 shots were performed in each target location before moving to a new region in the target surface.

The earlier interferograms (i.e. the 3 ns frame) show an expanding plasma with a density distribution that presents a maximum on-axis. However, as time evolves and the pump laser intensity increases, the plasma density profile acquires a concave shape with a density minimum on-axis. This is already clearly developed at 6 ns after the initiation of the current pulse, and it becomes more pronounced in the subsequent several nanoseconds. At times after the termination of the Nd:YAG laser pulse, the decreasing degree of ionization of the plasma causes significant absorption of the probe beam by photo-ionization. The absorption is more significant on the side lobes than on the axis of the plasma, indicating that the central part of the plasma is probably hotter, significantly less dense, or both. The asymmetry

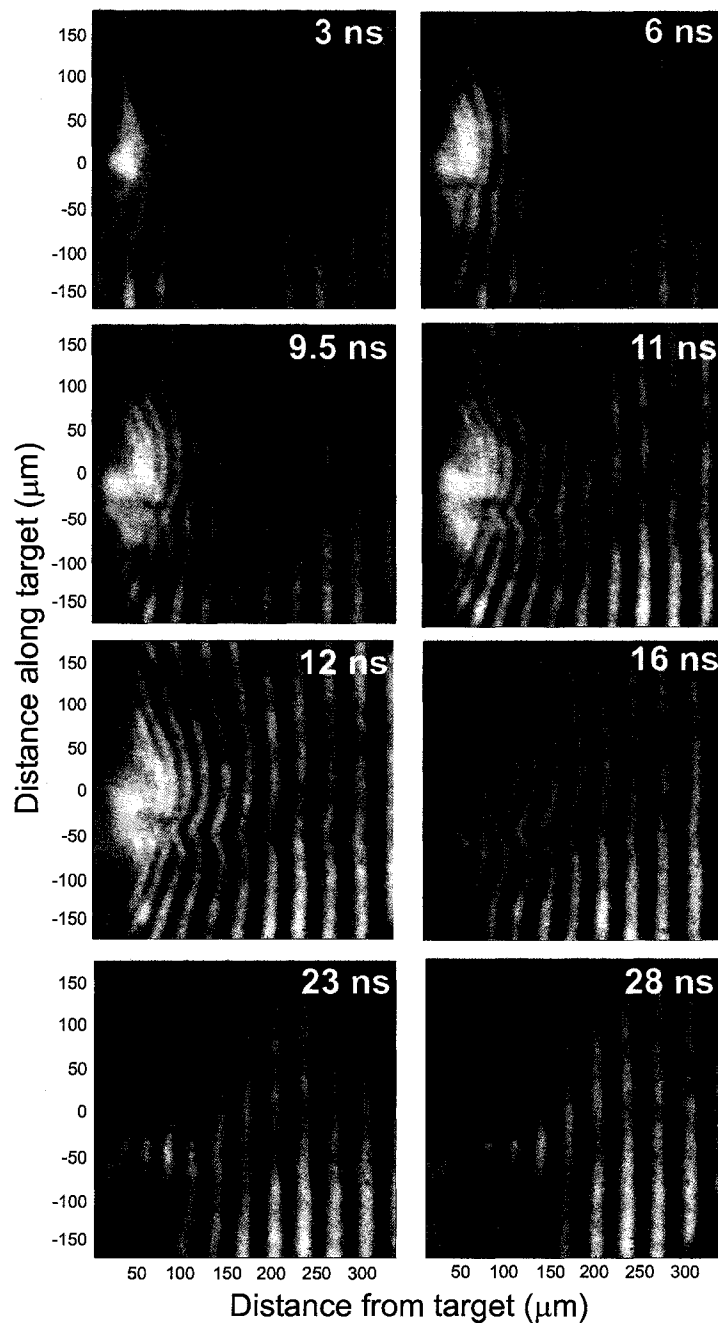


Figure 3.2: Sequence of soft x-ray interferograms describing the evolution of 1.8 mm long plasma generated by focusing a 13 ns FWHM Nd:YAG laser pulses with 0.6 J energy onto a $\sim 30 \mu\text{m}$ wide line on a copper target. The time delays are measured with respect to the beginning of the laser pulse. A very noticeable change in the curvature of the fringes is seen starting in the 6 ns frame.

observed in some of the interferograms is due to a slight misalignment of the tilt of the target.

Figure 3.3 shows the corresponding density maps obtained from the fringe shifts assuming the plasma is uniform along the probe beam axis. To calculate the density from the interferograms a reference interferogram was used to determine the original position of the fringes. The measured density reaches a value of 10^{20} cm^{-3} . Again, the maximum density measured is most likely limited by refraction of the probe beam. The density depression is very clearly seen in the electron density maps, in the frames corresponding to times between 6 ns and 23 ns. The last frame shows very small densities that are comparable with the minimum sensitivity of the interferometer. This is evidenced by the noisy aspect of the density map in this region.

To make sure that this unexpected plasma behavior was not a consequence of structure on the plasma heating beam, the intensity profile of the pump laser beam was imaged at the target plane using a CCD. The resulting beam profile, shown in Fig. 3.4 has very little structure, and it cannot cause the observed plasma density profile.

Plasma structure with high density flanks was observed by Rus *et al.* [3.17] in experiments that used a much wider line focus with similar heating laser intensity in copper and Zinc plasmas. Those high density flanks were attributed to the guiding of the expanding plasma by the groove created by the plasma ablation. The tight focus of the experiments described here and the fact that the sidelobes observed extend almost $200 \mu\text{m}$ away from the axis of the heating laser beam rules out this as a cause for the sidelobe formation. The craters left on the target in these experiments are very narrow lines with a surrounding large and shallow ablation area.

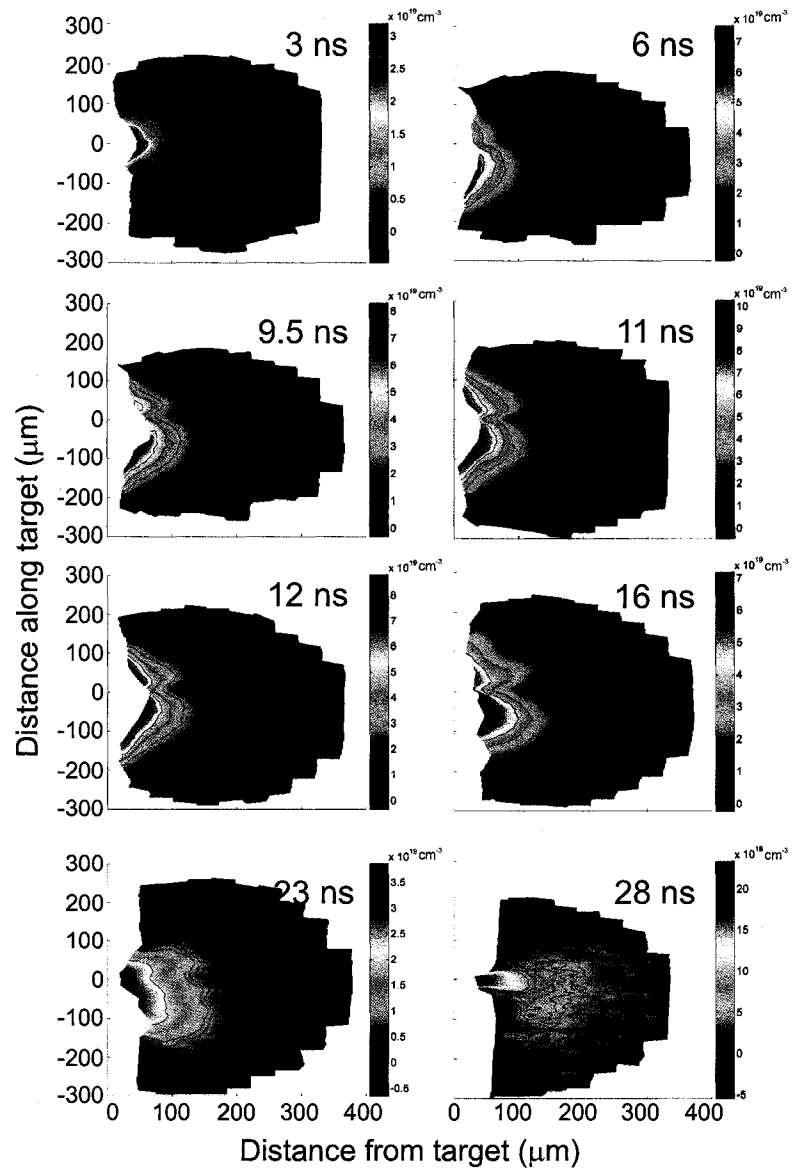


Figure 3.3: Sequence of two-dimensional density maps depicting the evolution of the electron density of a copper plasma, extracted from the interferograms in Fig. 3.2.

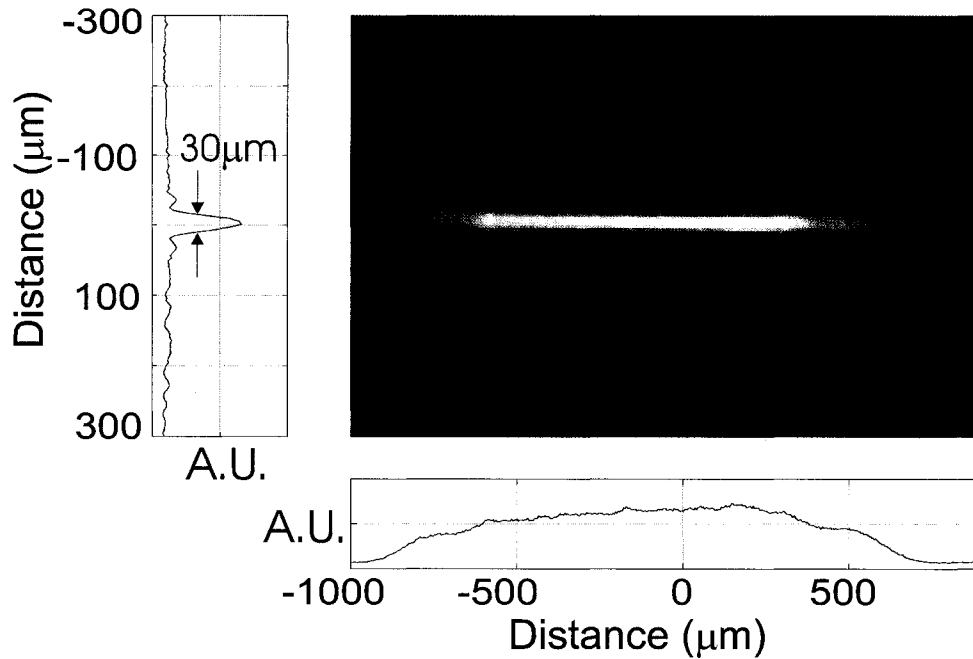


Figure 3.4: Image of the line focus used to generate the plasma of figure 3.2. The lineouts show very small structure on the beam.

To understand this unusual electron density profile the plasma was modeled with the hydrodynamic code LASNEX [3.18]. The simulations were performed by Steve Moon at Lawrence Livermore National Laboratory. The description of the phenomena requires two-dimensional simulations. Both single-dimension and two-dimensional modeling rule out the possibility that the ponderomotive force might be the primary cause of the observed plasma behavior, as it is known to take place for larger irradiation fluxes [3.7] or with long wavelength laser-irradiation [3.19]. The radiation pressure can be estimated by considering that the photons from the plasma-heating beam can be absorbed or reflected by the plasma, resulting in a transfer of momentum of $\hbar k$ or $2\hbar k$ respectively. Then, the radiation pressure P_r [3.20] is given by

$$P_r = \frac{F_{abs} I}{c}, \quad (3.2)$$

where F_{abs} is a factor that depends on the absorption of the beam and can take values between 1 and 2. This radiation pressure can be compared with the electron thermal pressure that expands the plasma, and that is given by $P_e = n_e \kappa T_e$ where κ is Boltzmann constant. For the highest intensities used in this work, the radiation pressure reaches only 5 % of the electron thermal pressure. The experiments that have shown the effect of radiation pressure used heating beam intensities of $3 \times 10^{14} \text{ Wcm}^{-2}$ and above [3.7].

The computed plasma electron density profiles are shown in Fig. 3.5 The resulting physical picture consists of a relatively high temperature ($\sim 36 \text{ eV}$) central region surrounded by a lower temperature ($\sim 10 \text{ eV}$) plasma on either side. The on-axis density and velocity distributions fit well the results of both 1D cylindrical expansion and two-dimensional simulations of a laser-irradiated plasma. Instead, the side-lobes are entirely two-dimensional formations created outside the laser-irradiated target region by the build-up of new cold material resulting mainly from extreme ultra violet (XUV) plasma radiation induced evaporation. In addition, two-dimensional simulations show that radiation cooling contributes to substantially lowering the temperature of the sidelobes. The sidelobes have slower axial expansion ($< 1 \times 10^6 \text{ cm/s}$) as compared to the hotter central plasma region ($5 - 6 \times 10^6 \text{ cm/s}$). After several nanoseconds the pressure balances in the lateral direction within a distance of $\sim 100 \mu\text{m}$ from the axis, as dictated by the sound speed ($\sim 10^6 \text{ cm/s}$) and plasma lifetime ($\sim 10^{-8} \text{ s}$), hence forming a density depression on-axis and sidelobes in the colder areas.

To illustrate that the sidelobes are mainly caused by outside spot ablation, simulations were performed in which the target ablation outside the area illuminated by the laser was constrained while maintaining otherwise identical physics.

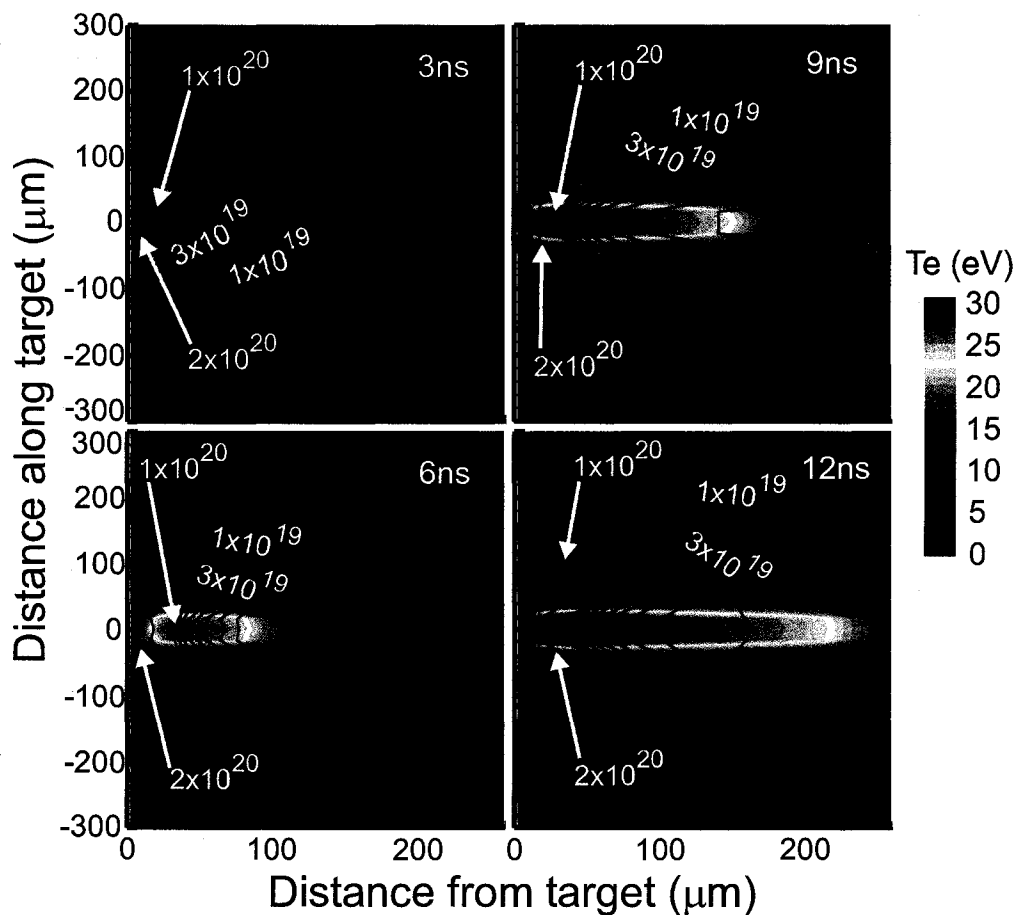


Figure 3.5: Simulated electron density (line contours) and temperature (filled contour) profiles of the line focus plasma of figure 3 computed using LASNEX. The heating laser is incident from the right. The calculations were done for a 10^{11} Wcm^{-2} , 13 ns FWHM laser pulse.

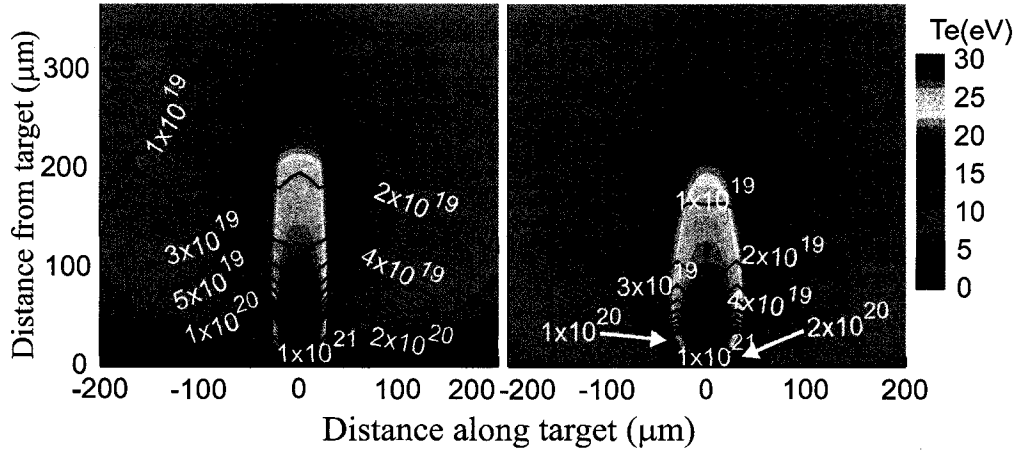


Figure 3.6: Simulated density (line contours) and electron temperature (filled contour) profiles for the line focus plasma at 12 ns (left), and with the motion of the ablated material from the target outside the spot constrained (right). Otherwise the conditions for the two simulations are identical. The heating laser is incident from the top. Both figures are calculated at the peak of the 10^{11} Wcm^{-2} , 13 ns FWHM laser pulse.

The result of this simulation in Fig. 3.6(right) shows that in this case the expansion is closer to the classical case and presents significantly smaller density inhomogeneities than the simulation computed with ablation permitted Fig. 3.6(left). Furthermore an additional simulation shows that if all radiation effects are excluded from the computation the expansion becomes classical and the sidelobes disappear, in which case the temperature in the conical expansion does not drop as dramatically along the surface. This indicates that the energy transport in the plasma by radiation is a key factor in the creation of the sidelobes.

The modeling also shows that this two-dimensional density behavior is essentially a universal effect. It will be present in the case of larger focal spots, but in this case it is not as pronounced. Some indications to this effect can be found in the experiment by Bolshov *et al.* and Zakharenkov *et al.* [3.12–3.14]. Due to the fact that dense plasmas are very efficient sources of XUV radiation even at low plasma

temperatures, this kind of plasma behavior should be seen in many experiments. However, because it takes a relatively long time $\sim 4\text{-}10$ ns for the off-spot material to evaporate and the colder plasma to expand, this effect was not previously clearly identified in shorter pulse experiments. The longer pulse duration in the present experimental situation allows the establishment of the pressure balance, such that the hotter central plasma corresponds to a lower density.

After having understood the mechanism that forms the two-dimensional structure in the plasmas it is possible to recognize the same structure in the first sequence of interferograms obtained as a proof of principle of the DGI and shown in Fig. 2.14. Some of the interferograms of this sequence present a very small density depression that is more evident later in time when the plasma presents more absorption on the sidelobes, indicating either a denser or colder plasma.

3.2 Density depression in aluminum plasmas with a 600 ps heating pulse

The plasma studied in the previous section was created using a 13 ns (FWHM) laser pulse that heats the plasma for a relatively long time. The simulations suggested that this is a general phenomenon that should be present in other cases, even in plasmas created using shorter laser pulses. In this section, experiments performed in aluminum plasmas heated with a 600 ps (FWHM) pulse are shown to have a similar density depression very close to the target and early in time.

The experiments were conducted on the COMET laser (Compact Multipulse Terawatt laser) at the Lawrence Livermore National Laboratory using the 14.7 nm Ni-like Pd soft x-ray laser as a probe beam that has been described in section 1.4.2. The soft x-ray laser pulse duration of ~ 5 ps gives the time-resolution for the interferograms, that, combined with the short wavelength, allows measurements

a few μm from the target surface. The interferometer used is the DGI described in section 2.4, especially constructed to work at this wavelength. It was decided to relay image the x-ray laser exit pattern from the end of the Pd target to the target plane inside the interferometer. This made the x-ray laser beam alignment insensitive to shot-to-shot variation in deflection angle exiting the Pd plasma. The soft x-ray laser pump laser and the plasma-forming laser were originated from the same oscillator so they were synchronized. The delay between the pump and the probe beams was adjusted by means of an optical delay line on the plasma-forming beam. The timing between the two laser beams was measured using fast photodiodes giving a precision of ~ 100 ps. The plasma forming beam used had a pulse width of 600 ps (FWHM), a wavelength of 1054 nm and 3.1 J of energy. A line focus 12 μm wide and 3.1 mm long was generated with a combination of a spherical and a cylindrical lens. This laser beam was incident on a 1 mm long flat (mirror polished) aluminum target. The x-ray laser probed the axis of the 1 mm plasma longitudinally and the end of the plasma was imaged by a Mo-Si multilayer-coated 25 cm focal length spherical mirror onto a back-thinned charge-coupled device (CCD) with 1024×1024 pixels (pixel size $13 \times 13 \mu\text{m}^2$), resulting in a total magnification of $22 \times$.

Figure 3.7 shows the interferograms obtained at the times 0, 0.2, 0.8 and 0.9 ns after the peak of the plasma-heating laser pulse. The interferograms depict a cylindrically expanding plasma, characterized by a convex density profile, at distances further than 50 μm from the target surface. However closer to the target surface, typically within 25 μm , there is a pronounced on-axis density depression centered at the peak intensity of the plasma heating laser. This feature is well established at these times and is observed to form during the rising edge of the

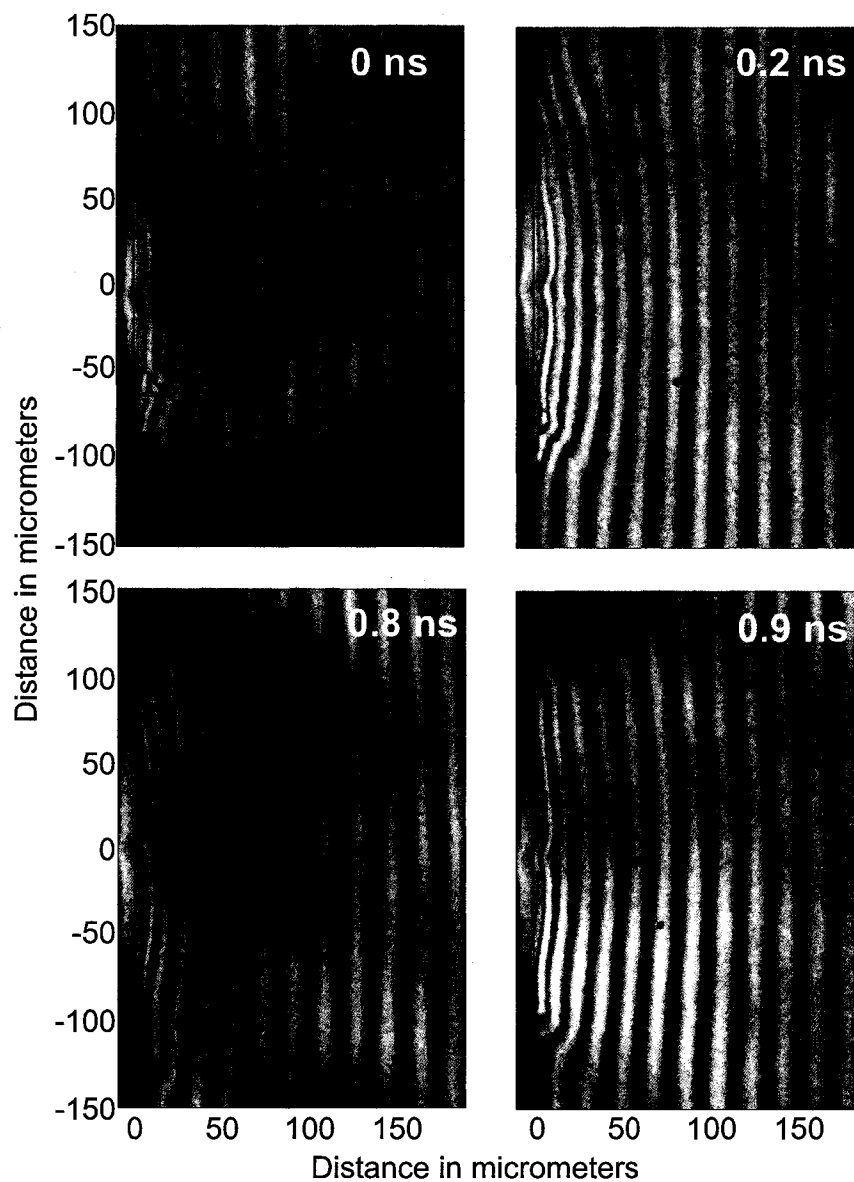


Figure 3.7: 14.7 nm x-ray laser interferogram measured at 0.3 ns after the peak of the laser pulse of aluminum plasma heated at 10^{13} Wcm^{-2} in $12 \mu\text{m}$ (FWHM) focus. The laser is incident from right side. A density depression is observed on-axis

laser pulse. The side lobes adjacent to the depression are observed to expand laterally in time.

At times greater than 1 ns (not shown in Fig. 3.7), as the plasma cools down, the assumption that only free electrons contribute to the index of refraction is not valid because the bound electron contribution is similar or even greater sometimes than that of the free electrons in the plasma. The index of refraction dependence on the free and bound electrons is discussed in section 1.3, and experimental results that unveil this effect in multiply ionized plasmas (where it was considered to be negligible) are shown in the next chapter. The late times of the sequence in Fig. 3.7 are shown in Fig. 4.2

From the interferograms of Fig. 3.7, electron density maps were computed by assuming an uniform plasma along the line of sight of the probe beam. Figure 3.8 shows these electron density profiles calculated assuming that the reference fringes were straight extensions of the fringes on the periphery of the field of view, far away from the influence of the plasma. The field of view of the interferograms, which is significantly larger than shown ($400 \mu\text{m} \times 600 \mu\text{m}$), allows the position of these reference fringes to be determined reliably.

To understand the physical phenomena driving the early stages of the evolution of these aluminum plasmas, hydrodynamic simulations of the experimental laser plasma conditions were performed using the 2-D LASNEX code [3.18]. The experimental spatial and temporal profiles were used in the simulations for comparison with the measured density profiles at various times. Three dimensional laser ray-tracing and deposition packages were included with inverse Bremsstrahlung as the main absorption mechanism. Radiation transport utilized flux limited multi-group diffusion with a flux limiter $f = 0.1$. The flat aluminum target was zoned

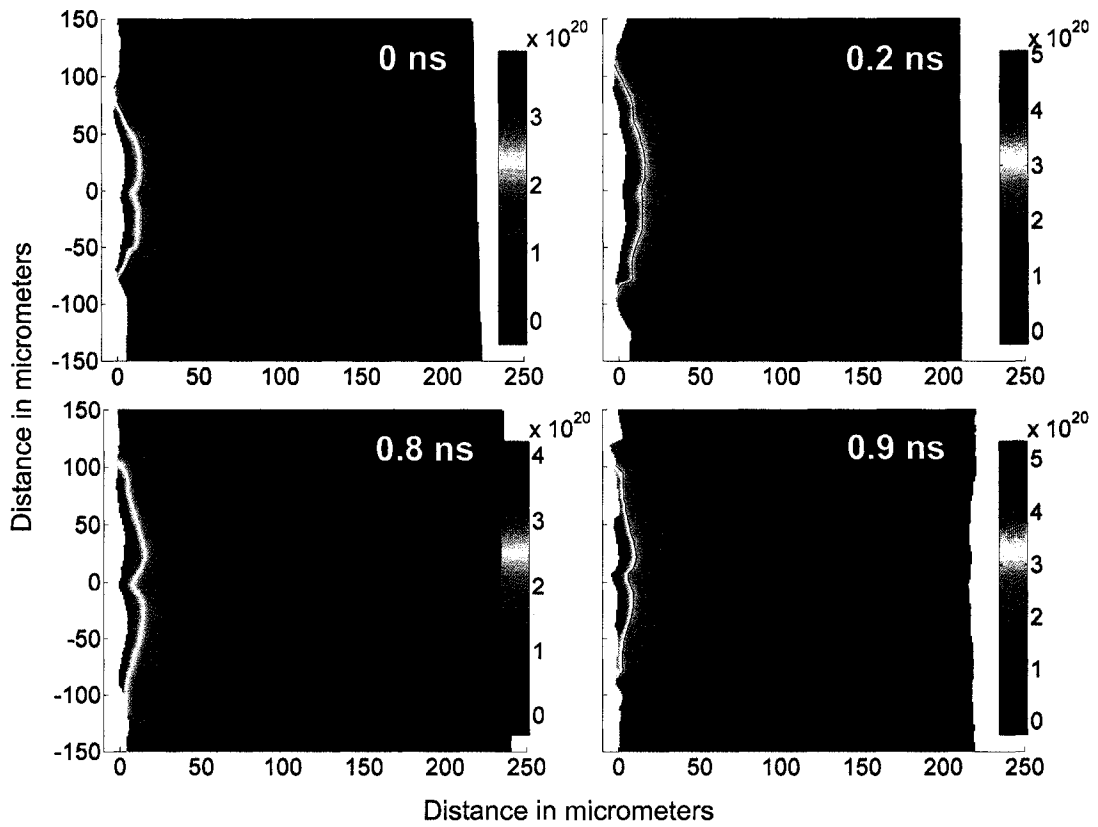


Figure 3.8: Density profile extracted from the interferograms in Fig. 3.7.

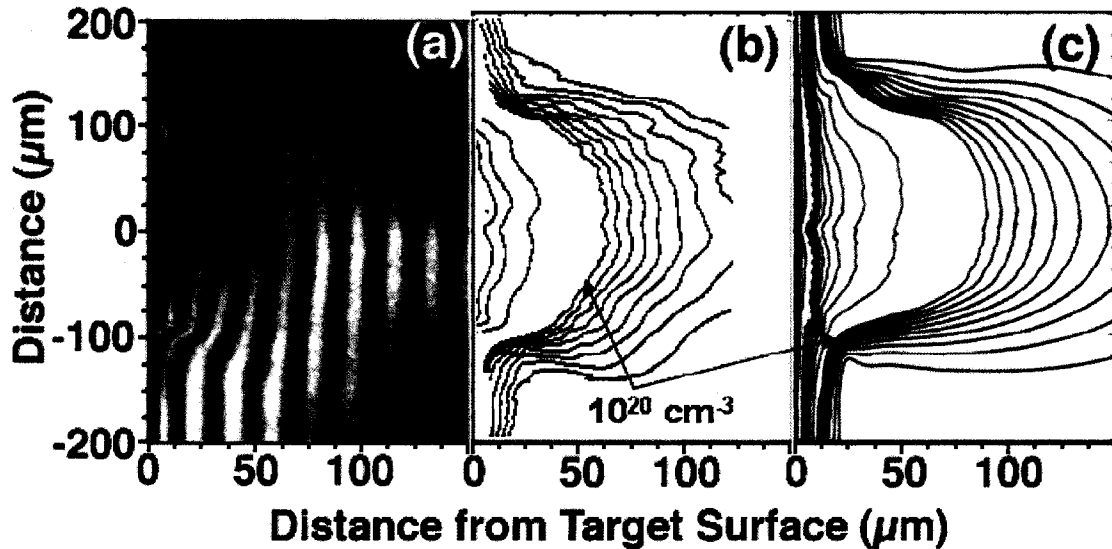


Figure 3.9: (a) 14.7 nm x-ray laser interferogram of an aluminum plasma heated with 10^{13} Wcm^{-2} in $12 \mu\text{m}$ (FWHM) focus, measured at 0.3 ns after the peak of the laser pulse. (b) Density contours extracted from the interferogram. (c) 2-D LASNEX simulations corresponding to the same plasma at the same time. The extended sequence is shown in Fig. 3.7.

with $1\text{-}\mu\text{m}$ steps laterally with finer steps inside the target. Thermal conductivity and electron-ion coupling were from the Lee-More model [3.21] and the Livermore Equation of State (LEOS) was used.

Figure 3.9 shows the density profile from a 2-D hydrodynamic simulation from LASNEX for the time of 0.3 ns after the peak of the heating laser pulse. There is excellent agreement showing the formation of the main features at various times.

To study the basic energy transport mechanisms in the plasma, additional hydrodynamic simulations were performed using a square spatial heating beam profile with a $10 \mu\text{m}$ wide focus irradiated with an intensity of 10^{13} Wcm^{-2} . This prevents direct heating of the side walls of the target. Figure 3.10 shows two density profiles, at -0.5 ns and 0.3 ns relative to the heating laser peak, corresponding to before and after the formation of the on-axis density depression. The early time,

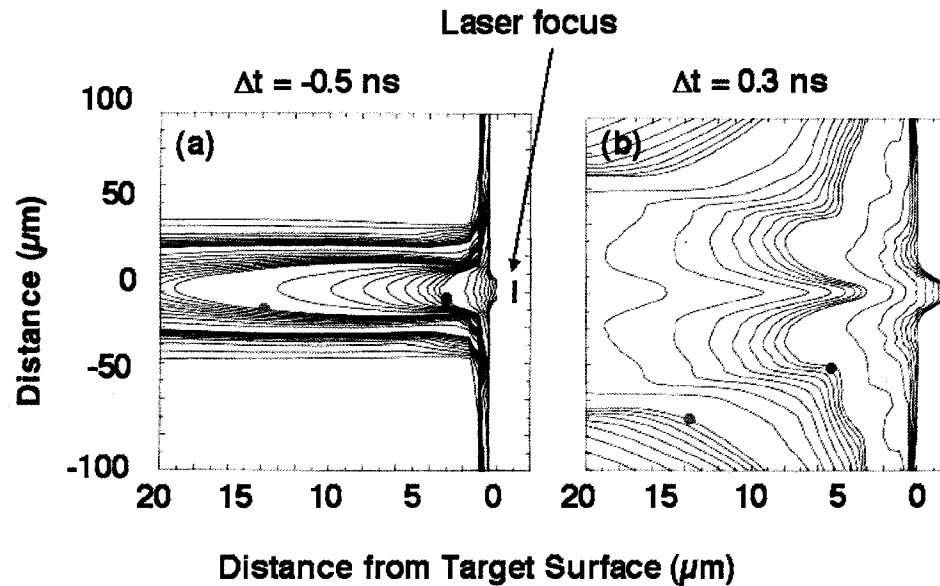


Figure 3.10: 2-D LASNEX simulations corresponding to an aluminum target heated by a 600 ps pulse at 10^{13} Wcm^{-2} in a $10 \mu\text{m}$ square spatial focus. The laser is incident from the left. The 10^{20} and 10^{21} cm^{-3} contours are indicated by the gray and black filled circles.

Fig. 3.10(a), has the classic convex 2-D density profile expected from a small laser focus. Approximately 200 ps later as the plasma corona is rapidly heated by the laser, mass is ablated outside the laser spot from a combination of x-rays and thermal electron conduction. The critical surface becomes concave due to the rapid expansion of the directly heated material while the cooler surrounding material beside the corona experiences thermal pressure from the hotter material. The result is the formation of denser side lobes that remain part of the density profile late in time, Fig. 3.10(b). Low temperature ionized material outside the laser spot continues to be generated by soft x-rays and is further heated by thermal electron conduction. This plasma moves perpendicular to the target surface in a larger area surrounding the central region, giving rise to the extended plasma along the target.

A comparison of the results presented in Fig. 3.7 with those presented in the previous section (Fig. 3.2) reveals that while the underlying energy transport mechanisms are similar, there are differences between the two experiments. The pulse duration (600 ps) in these experiments is twenty times shorter than the pulses used to heat the copper plasmas (13 ns). The irradiance is two orders of magnitude higher in the aluminum experiments. Although the non-local radiative heating is shorter in duration, the higher temperatures ($T_e \sim 200$ eV versus ~ 30 eV) produce strong ablation outside of the laser focal spot. The copper plasma sidelobes were heated by less energetic photons and for longer times, establishing a more steady-state condition. This may explain the reason for the observation of the lobes extending further away and beyond $100 \mu\text{m}$ from the target surface. The density lobes in the aluminum plasma, shown in Fig. 3.7, are visible only up to $40 \mu\text{m}$ from the target. The physical picture of the evolution of the aluminum plasmas is that there is a lateral transport of energy via electron conduction and most importantly, soft x-ray radiation. The energy is transported out of the central hot spot and then down to the surface where it ablates cold dense material. This plasma then expands and also interacts with the hot plasma jet originating from the ablation region. All this results in the formation of the observed density profiles with a central depression in the center.

3.3 Density depression in point-focus laser-created plasmas

Experiments were performed in which a plasma created using a $30 \mu\text{m}$ spot-focused laser were studied using the 46.9 nm laser probe. This type of plasmas are inherently two-dimensional, with a revolution symmetry around the heating beam axis. The presence of a crater, formed by previous shots, limits the expansion

of the plasma redirecting it in the direction away from the target surface. This geometry provides unique plasma dynamics that makes it interesting to study and to compare with results from hydrodynamic simulations. Also, by concentrating the pump laser in a smaller area, a higher irradiance is obtained.

The main disadvantage of using a spot focus is that the analysis of the interferograms is no longer straight forward and it now requires a deconvolution of the measured information through the use of an Abel inversion technique ¹ to recover the three-dimensional profile of the plasma.

The setup was very similar to that used in section 3.1, except that now the magnification was changed to 51 ×. The target consisted of a 99.99% pure copper disk that could be rotated around its axis using a motorized stage, allowing access to approximately 200 target locations without having to break vacuum. The plasmas were created by focusing 0.62 J pulses from a Nd:YAG laser ($\lambda=1.06 \mu\text{m}$, 13 ns FWHM duration) with an $f = 15 \text{ cm}$ aspheric lens into a $\sim 30 \mu\text{m}$ diameter spot to generate laser intensities of $\sim 7 \times 10^{12} \text{ Wcm}^{-2}$.

Interferograms of plasmas created by firing a first, second or fifth laser shot in the same target location were recorded. The interferograms corresponding to a first shot show the high density plasma region extends only a few tens of micrometers away from the target. In contrast, the plasmas produced firing multiple laser shots in the same target location are observed to cover a significantly larger volume, with

¹The Abel inversion or transform is a technique commonly used to calculate the emission function given a projection of that emission function. The transform, applied to the case of interferometry, gives the radial dependent index of refraction ($\eta(r)$) from the measured number of fringe shifts (N_f) and takes the following form: $\eta(r) = -\frac{\lambda}{\pi} \int_r^R \frac{dN_f(y)}{dy} \frac{dy}{\sqrt{y^2-r^2}}$. Where R is the maximum extension of the observed fringe shifts. For more details on this calculation see Ref. [3.22].

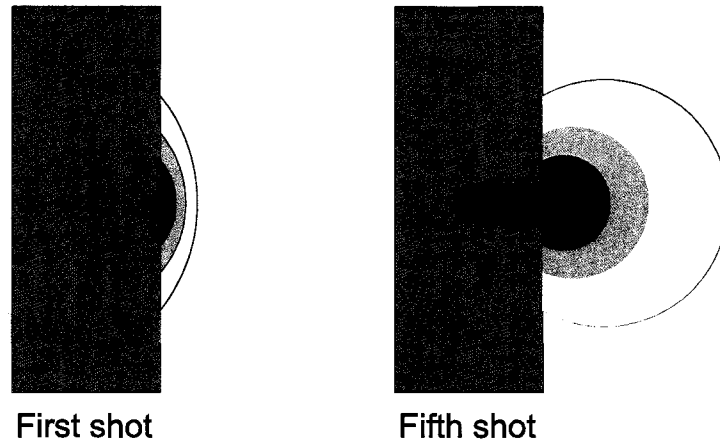


Figure 3.11: Schematic representation of the plasmas formed inside the target in first and fifth shots and how much the plasma is extended.

large electron densities at distances more than a hundred micrometers from the target surface. This is illustrated in Fig. 3.11. The larger extent of the plasmas results from the fact that they emanate from the crater created by the previous shots (a single pre-shot on target for the 2nd shot series, or 4 pre-shots for the 5th shot series). The crater constrains the lateral expansion and guides the plasma motion into the direction normal to the target. The crater formed on the target after the fifth shot is observed to have relatively vertical walls, depth of $\sim 300 \mu\text{m}$, and a diameter of $\sim 200 \mu\text{m}$. Previous studies of laser-created plasmas have recognized that plasma characteristics can be influenced by the presence of a crater [3.17, 3.23].

Figure 3.12 shows a sequence of interferograms corresponding to plasmas generated by firing the laser a fifth time on the same target location. The time relative to the initiation of the heating laser pulse is indicated. In all the cases (for 1st, 2nd and 5th shot on target) the interferograms present a flattening or reversal of the curvature of the interference fringes near the irradiation axis. In this axisymmetric geometry such fringe patterns are indicative of a concave electron density

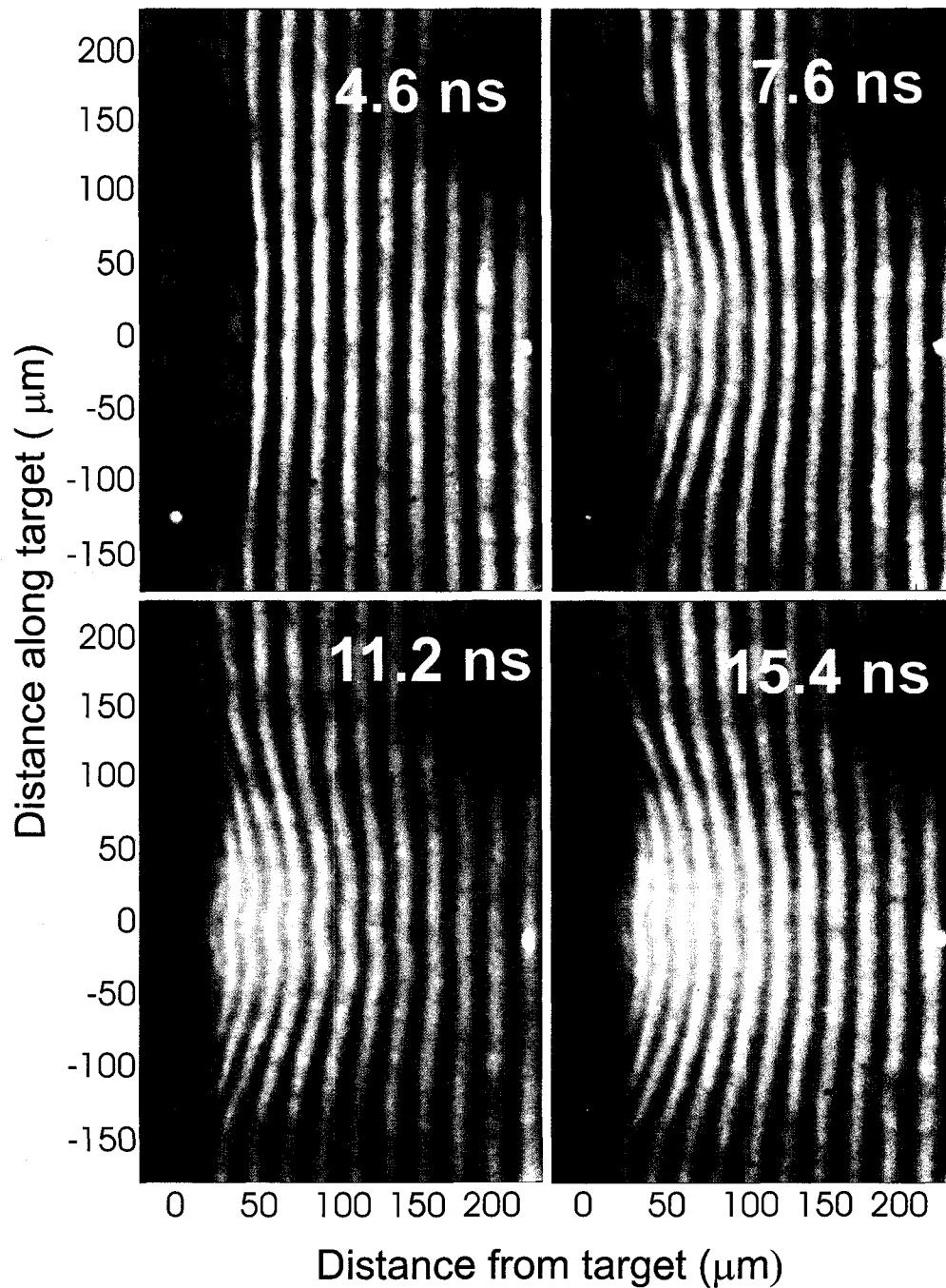


Figure 3.12: Sequence of interferograms corresponding to spot-focus plasmas generated firing a 5th shot in the same location on a copper target. The spot diameter was $\sim 30 \mu\text{m}$ and the beam intensity was $7 \times 10^{12} \text{ cm}^{-3}$. The times indicated are measured with respect to the beginning of the laser pulse.

profile with a minimum on-axis (a probe ray intercepting the axis transverses a maximum length of plasma, undergoing a maximum phase shift unless there is a density depression or cavity). At the time of the maximum laser intensity this central minimum in the density profile is observed to extend through a significant part of the sub-critical region of the plasma. It should be noticed that this concave electron density profile was observed in the 1st shot in spot focus and is therefore not a direct result of the crater created by previous shots on target. This density cavity becomes more pronounced as time progresses towards the maximum of the heating laser pulse. The electron density distributions derived from Abel Inversion of the interferograms of Fig. 3.12 are shown in Fig. 3.13. The formation of a concave electron density profile with a pronounced plasma sidelobe and a density cavity on the irradiation axis is observed. A series of interferograms obtained for plasmas generated by firing a second shot in the same target location shows qualitatively similar density profiles and temporal evolution. In that case the electron density in the sidelobes was observed to increase as a function of time, to reach a maximum density $\sim 9 \times 10^{20} \text{ cm}^{-3}$ (90% of the critical density of the heating laser beam) at a distance of $27 \mu\text{m}$ from the target surface near the time of maximum laser irradiation intensity.

Again, the hydrodynamic code LASNEX [3.18] was used to simulate the plasmas studied by soft x-ray laser interferometry. Figure 3.14 shows the computed evolution of the electron density and temperature profiles for the spot-focus plasma of Figs. 3.12 and 3.13. The simulations were performed for a 0.65 J and 13 ns FWHM 1ω Gaussian light pulse, with a spot size of $30 \mu\text{m}$ diameter focused at the origin ($z=0$). The interaction was treated using geometrical optics propagation with inverse Bremsstrahlung absorption along the path of propagation. In agreement with the experiment, dense plasma sidelobe and a density minimum on-axis

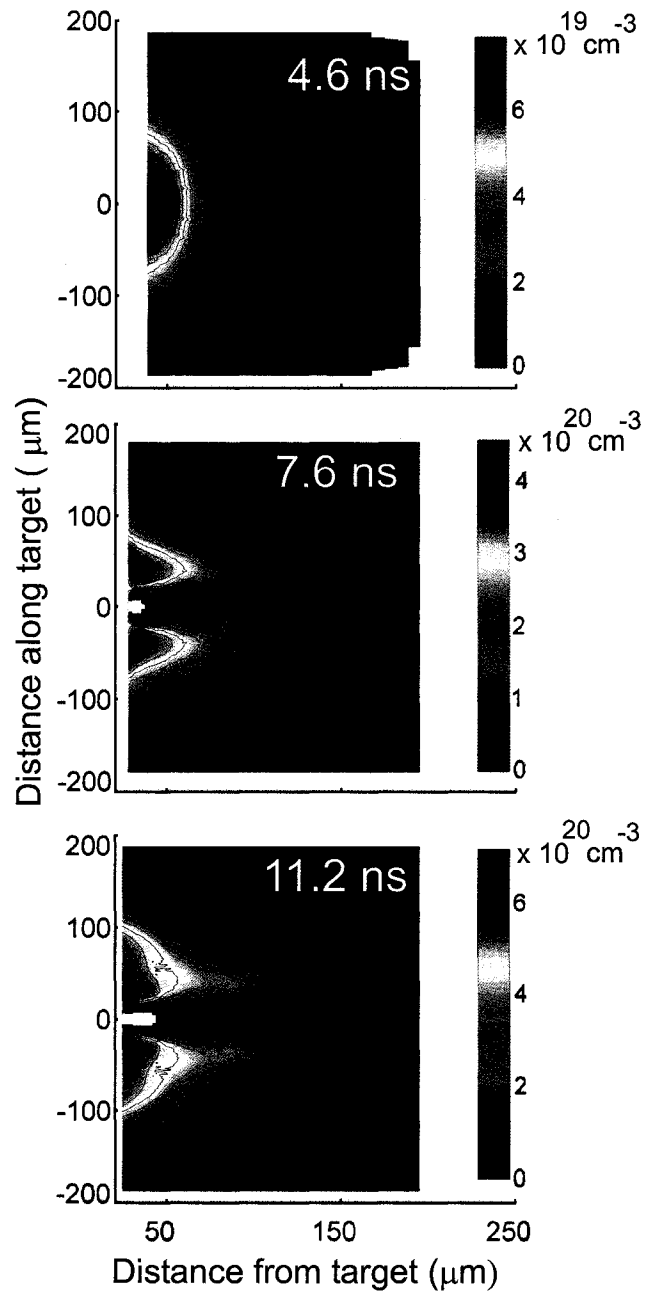


Figure 3.13: Plasma density profiles corresponding to the interferograms of Fig. 3.12

are seen to develop. At 11.2 ns after the initiation of the laser pulse the density in the sidelobe reaches $\sim 5 - 6 \times 10^{20} \text{ cm}^{-3}$ at $50 \mu\text{m}$ from the target and $50 \mu\text{m}$ from the axis, and in comparison is $\sim 1 \times 10^{20} \text{ cm}^{-3}$ on-axis at the same distance from the target. At $100 \mu\text{m}$ from the target the sidelobe density still has a maximum of $3 \times 10^{20} \text{ cm}^{-3}$. The electron temperature in the axial region irradiated by the laser is computed to increase as a function of time, reaching 150 eV near the time of the peak laser intensity. The plasma in the sidelobe is much colder, with an electron temperature of about 25 eV due to effective radiation cooling. The calculations show that here, as in the case of the previous line focus experiments, radiation pressure effects do not play a significant role in the formation of the observed density profile. The simulations also show that the 1ω laser beam is not strongly refracted, and due to the relatively low laser intensity and small plasma size, laser plasma instabilities are not expected to play a significant role (the stimulated Brillouin scattering growth factor is small), and the plasma structure is not caused by filamentation. Instead the “inverted” density profile is a consequence of hydrodynamic and plasma radiation effects.

As is also the case for the line focus experiments, the simulation shows that the density of the sidelobe is significantly increased by plasma radiation-induced ablation of target material from the area surrounding the laser-irradiated spot. Plasma radiation is also a major cooling mechanism for the sidelobe plasma. Pressure balance between the two concentric regions contributes to the development of a density depression on-axis, as with the previously studied case of a line-focus plasma. However, in this case, the absence of radiation induced ablation does not stop the “hole formation” in the case of deep crater-based plasmas. Across such a relatively narrow crater, pressure balance easily takes place, hence creating a

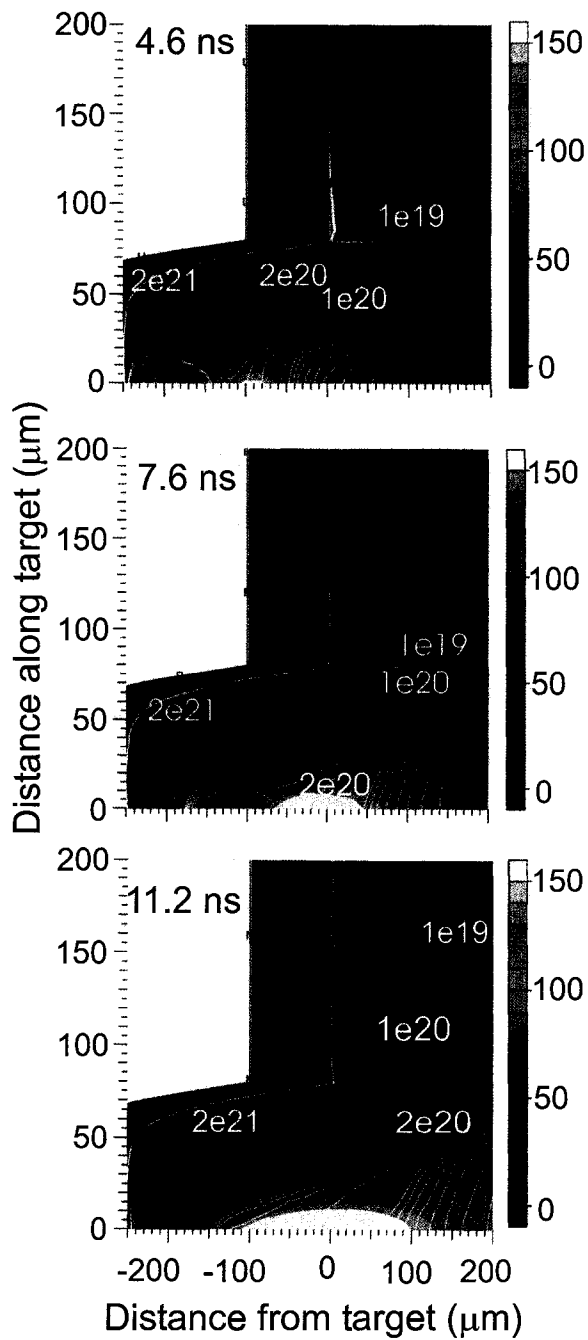


Figure 3.14: Sequence of simulated electron density (line contours) and temperature (filled contour) profiles for the spot-focus plasma of Fig. 3.12 computed using LASNEX. The heating laser is incident from the right

density depression in the hot part along the irradiation laser axis. In other words, the laser pulse is sufficiently long for the interior of the crater to be filled with plasma ablated from the focal spot at the crater's bottom and for sound waves to transverse the crater dimension multiple times. In addition, in the present case the crater constrains the plasma expansion in the lateral direction and guides the motion in the direction perpendicular to the target, enhancing the density at large distances from the surface. Plasma radiation adds additional ablated mass, significantly enhancing the magnitude of the plasma density and the depression outside the cavity, which makes it easier to probe. The role of plasma radiation was studied by conducting simulations in which the radiation induced ablation outside the $30\ \mu\text{m}$ diameter central region or the radiation transport were turned off. It is observed that in the absence of plasma radiation induced ablation the electron density in the sidelobe is diminished by nearly an order of magnitude at $50\ \mu\text{m}$ from the target (from $\sim 5 - 6 \times 10^{20}\ \text{cm}^{-3}$ at $50\ \mu\text{m}$ from the axis to about $5 \times 10^{19}\ \text{cm}^{-3}$ in the same location for the case without plasma radiation-induced ablation). In the case without radiation transport the plasma temperature in the sidelobe is significantly higher, and both the density in the sidelobe and the magnitude of the density depression is significantly reduced.

3.4 Conclusions

The experimental results presented in this chapter show a very clear two-dimensional hydrodynamic effect of large magnitude in laser-created plasmas generated at relatively low irradiation intensities in narrow laser foci. A very noticeable density depression is observed in plasmas that were generated under a variety of conditions: a 13 ns long pulse in both a $30\ \mu\text{m}$ wide line focus and a

point focus geometries impinging on solid copper targets, with irradiation intensities of $\sim 10^{11} \text{ Wcm}^{-2}$ and $\sim 10^{12} \text{ Wcm}^{-2}$ respectively, and a short, 600 ps pulse in a $12 \mu\text{m}$ wide line focus geometry impinging on solid aluminum targets with an irradiation of $\sim 10^{13} \text{ Wcm}^{-2}$. The onset of the density depression changes in time and distance from the target, but the general physical picture is the same in all cases. For all the cases the main mechanism responsible for the density depression is the build-up of cold material generated by an increased ablated area caused mainly by XUV plasma radiation emitted from the central hot region in the plasma, combined with pressure balance.

By combining the experimental results with two-dimensional hydrodynamic LASNEX simulations the effect was understood. The simulations indicate that this is essentially a general effect that should be observed over a relatively wide range of plasma parameters.

For the case of the spot-focus plasma experiment, the use of soft x-ray wavelengths allowed the mapping of the density profile up to nearly $9 \times 10^{20} \text{ cm}^{-3}$, a value that is close to the critical density for the plasma heating beam. The results constitute the first demonstration of the use of table-top soft x-ray laser interferometry in the study of complex high density plasma phenomena, and also the first demonstration of soft x-ray laser interferometry with picosecond resolution.

Bibliography

- 3.1 T.P. Hughes. *Plasma and Laser Light*. John Wiley and Sons, New York, 1975.
- 3.2 Mordecai D. Rosen. The science applications of the high-energy density plasmas created on the nova laser. *Physics of Plasmas*, 3(5):1803–1812, 1996.
- 3.3 Paddy Hayden, Anthony Cummings, Nicola Murphy, Gerry O’Sullivan, Paul Sheridan, John White, and Padraig Dunne. 13.5 nm extreme ultraviolet emission from tin based laser produced plasma sources. *Journal of Applied Physics*, 99(9):093302, 2006.
- 3.4 D. L. Matthews, P. L. Hagelstein, M. D. Rosen, M. J. Eckart, N. M. Ceglio, A. U. Hazi, H. Medeck, B. J. MacGowan, J. E. Trebes, B. L. Whitten, E. M. Campbell, C. W. Hatcher, A. M. Hawryluk, R. L. Kauffman, L. D. Pleasance, G. Rambach, J. H. Scofield, G. Stone, and T. A. Weaver. Demonstration of a soft x-ray amplifier. *Phys. Rev. Lett.*, 54(2):110–113, Jan 1985.
- 3.5 T. Tajima and J. M. Dawson. Laser electron accelerator. *Phys. Rev. Lett.*, 43(4):267–270, Jul 1979.

- 3.6 John Lindl. Development of the indirect-drive approach to inertial confinement fusion and the target physics basis for ignition and gain. *Physics of Plasmas*, 2(11):3933–4024, 1995.
- 3.7 D. T. Attwood, D. W. Sweeney, J. M. Auerbach, and P.H.Y. Lee. Interferometric Confirmation of Radiation-Pressure Effects in Laser-Plasma Interactions. *Phys. Rev. Lett*, 40:184–187, 1978.
- 3.8 S. Wilks, P. E. Young, J. Hammer, M. Tabak, and W. L. Kruer. Spreading of intense laser-beams due to filamentation. *Physical Review Letters*, 73(22):2994–2997, 1994.
- 3.9 K. Takahashi, R. Kodama, K. A. Tanaka, H. Hashimoto, Y. Kato, K. Mima, F. A. Weber, T. W. Barbee, and L. B. Da Silva. Laser-hole boring into overdense plasmas measured with soft x-ray laser probing. *Physical Review Letters*, 84(11):2405–2408, 2000.
- 3.10 Claire Ellen Max, Christopher F. McKee, and W. C. Mead. Scaling of Ablative Laser-Fusion Implosions. *Phys. Rev. Lett.*, 45:28–31, 7 July 1980.
- 3.11 G. S. Sarkisov, V. Yu. Bychenkov, V. N. Novikov, V. T. Tikhonchuk, A. Maksimchuk, S.-Y. Chen, R. Wagner, G. Mourou, and D. Umstadter. Self-focusing, channel formation, and high-energy ion generation in interaction of an intense short laser pulse with a He jet. *Phys. Rev. E*, 59(6):7042–7054, June 1999.
- 3.12 Bol'shov et al. *Sov. Phys. JETP*, 65(1160), 1987.
- 3.13 I. A. Zakharenkov, N. N. Zorev, O. N. Krokhin, I. A. Mikhailov, A. A. Rupasov, G. V. Sklizkov, and A. S. Shikanov. Study of the interaction between

- laser radiation and a plasma corona at flux densities of 10 to the 14 th power to 10 to the 15 th power $W/sq\text{ cm}$. *Zhurnal Eksperimental noi i Teoreticheskoi Fiziki*, 70:547–559, February 1976.
- 3.14 Zakharenkov. Private communication. 2002.
- 3.15 J. Filevich, K. Kanizay, M. C. Marconi, J. L. A. Chilla, and J. J. Rocca. Dense plasma diagnostics with an amplitude-division soft-x-ray laser interferometer based on diffraction gratings. *Optics Letters*, 25(5):356–358, 2000.
- 3.16 W.L. Kruer. *The Physics of Laser Plasma Interactions*, chapter 10, pages 116–117. West View Press, 2003.
- 3.17 B. Rus, P. Zeitoun, T. Mocek, S. Sebban, M. Kálal, A. Demir, G. Jamelot, A. Klisnick, B. Králiková, J. Skála, and G. J. Tallents. Investigation of zn and cu prepulse plasmas relevant to collisional excitation x-ray lasers. *Phys. Rev. A*, 56(5):4229–4241, Nov 1997.
- 3.18 G. D. Zimmerman and W. L. Kruer. Numerical simulation of laser-initiated fusion. *Comments Plasma Phys. Controlled Fusion*, 2:51, 1975.
- 3.19 V. Y. Baranov, K. N. Makarov, V. C. Roerich, Y. A. Satov, A. N. Starostin, A. E. Stepanov, B. Y. Sharkov, K. Langbein, and T. R. Sherwood. Study of multicharged heavy ion generation from CO 2 laser-produced plasma. *LASER AND PARTICLE BEAMS*, 14(3):347–368, 1996.
- 3.20 D. Attwood. *soft x-rays and extreme ultraviolet radiation*, chapter 6, page 238. Physics of hot dense plasmas. Cambridge University Press, Cambridge, 2000.

- 3.21 Y. T. Lee and R. M. More. An electron conductivity model for dense plasmas. *Physics of Fluids*, 27:1273–1286, May 1984.
- 3.22 Eric C. Hammarsten. Dense plasma diagnostics with a table top soft x-ray laser. Master's thesis, Colorado State University, 7 November 2003.
- 3.23 V. A. Boiko, S. A. Pikuz, and A. I. Faenov. Study of the three-dimensional structure of a laser plasma in the electron-density range from 10 to the 18th power to 10 to the 21st power by X-ray spectroscopic methods. *Soviet Journal of Quantum Electronics*, 2:1216–1224, June 1975.

Chapter 4

**MULTIPLY IONIZED PLASMA WITH INDEX
OF REFRACTION GREATER THAN ONE**

For many decades optical interferometers have been used to measure the electron density of plasmas using the assumption that only free electrons contribute to the index of refraction of these plasmas [4.1–4.3]. This assumption neglects the possible contribution that the ions could have either through the bound electrons or through the heavy nucleus. Under this assumption the index of refraction of the plasma is given by

$$\eta = \sqrt{1 - \frac{n_e}{n_c}}$$

and is always less than one¹.

This assumption is easy to justify when optical lasers are used to probe multiply ionized plasmas because in such cases the energy of the photons is much smaller than the binding energy of the outermost electrons in the ions. However, as the wavelength of the probe beam is decreased to the soft x-ray region of the spectrum, the energy of the probe photons increases and the approximation is no longer obviously valid. Over the last decade several interferometers [4.4–4.14] have been built and used to perform dense plasma diagnostics using probe wavelengths in the soft x-ray range of 14 to 72 nm (89 to 17 eV). Since the first plasmas that were studied were highly ionized, the natural (and easiest) approach was to extend the assumption of negligible ion contribution to the shorter probe wavelengths. So the analysis of the experiments done with these sources assumed that only the free electrons contributed significantly to the index of refraction.

¹For n_e greater than n_c the index is imaginary leading to a fast decay of the wave as shown in chapter 2 (1.8).

Recently, in interferometry experiments of laser-produced Al plasmas conducted using a probe wavelength of 14.7 nm combined with the Diffraction Grating Interferometer at Lawrence Livermore National Laboratory [4.13], interference fringes that bent in the opposite direction than was expected were observed, indicating that the index of refraction was greater than one. In this experiment, the interferometer was aligned in a way that an increase in density bends the fringes away from the target.

The interferograms show that the fringes, late in the plasma evolution, in the periphery of the plasma and close to the target surface, bend toward the target. This direction of the fringe shifts is indicative of an index of refraction greater than 1 (hereafter referred as negative or anomalous fringe shifts). The observation of similar negative fringe shifts was also reported from an independently realized aluminum laser-created plasma soft x-ray laser interferometry experiment at 13.9 nm [4.14]. The advantage of the data obtained with the 14.7 nm probe beam and presented herein is that it clearly shows the effect without the need for any processing of the fringes. The analysis of the data, done with the assistance of atomic physics calculations [4.15] and hydrodynamic model simulations [4.16], indicates that late in the plasma evolution the contribution of bound electrons dominates the index of refraction, causing the observed negative fringe shifts in the periphery regions of the plasma.

A significant result of the atomic computations motivated by these experiments is that the influence of the bound electrons on the index of refraction extends far from the absorption edges and resonance lines, affecting a broad range of wavelengths. Then, the effect should also be present in many other cases where a probe beam is close in energy to a resonant line or absorption edge [4.13,4.17–4.19].

An exploration of other plasma materials and another wavelength was conducted to find conditions in which the influence of bound electrons is important. This is the case for the 46.9 nm laser probing tin, silver and carbon plasmas when the plasmas are only a few times ionized.

The chapter continues with a description of the experiments that unveiled interferograms with negative fringe shifts and with the first results obtained in aluminum plasmas probed with a 14.7 nm wavelength laser. Then these first results will be analyzed in detail to show that the contribution of the few lower aluminum ions are responsible for the observed fringe shifts. A brief overview is presented of the Average Atom method developed by W. Johnson [4.20] that was used to calculate the index of refraction in a variety of plasmas and to predicted cases where negative fringe shifts would be observed. Finally the chapter will close with the experimental confirmation of these predictions, by probing silver, tin and carbon plasmas at a wavelength of 46.9 nm.

4.1 Setup for the experiments

The plasmas studied with soft x-ray interferometry presented in this chapter were created by illuminating solid targets with high-power pulsed-laser beams. Flat aluminum slab targets were heated using the Lawrence Livermore National Laboratory's Compact Multipulse Terawatt (COMET) chirped pulse amplification laser with an intensity $10^{13} \text{ W cm}^{-2}$, and semi-cylindrical grooves were illuminated with an intensity of $10^{11} \text{ W cm}^{-2}$ from a Ti:Sapphire laser at Colorado State University. Two different soft x-ray lasers were used to probe the plasmas in two separate sets of experiments. The probe lasers were described previously in sections 1.4.1 and 1.4.2. The flat aluminum slab targets were probed using the 14.7

nm Ni-Like Pd SXRL and the semi-cylindrical grooves were probed with the 46.9 nm Ne-Like Ar SXRL. Each laser was used in combination with a specially tailored Diffraction Grating Interferometer. These interferometers, which were described in great detail in section 2.4, were designed around the idea of using diffraction gratings as beam splitters [4.21]. The gratings, that send equal energy to the zero and first diffracted orders thanks to a blaze angle on its grooves, are arranged in the interferometer in a skewed Mach-Zehnder configuration [4.7, 4.22].

The version of the interferometer used in the experiments conducted at Lawrence Livermore National Laboratory with a 14.7 nm probe is depicted in Figure 4.1. In this version of the instrument, the output beam exits the interferometer parallel to the input beam to adapt to spatial constraints. This allows a CCD camera to be placed ~ 5 meters away to obtain a $22 \times$ magnification. This output geometry was achieved by replacing the multilayer relay mirror with a long grazing incidence gold coated mirror (L3). This has the added advantage of an improved throughput of the imaging system by the larger reflectivity on the grazing incidence optics as compared to multilayer optics.

The plasmas were created by focusing a laser beam on a solid slab target of aluminum. The heating beam was produced by the COMET laser. The plasmas were heated at an irradiance of 10^{13} Wcm^{-2} by focusing a 600 ps, 3 J, 1054 nm laser into a 3.1 mm long \times 12 μm wide line focus. The aluminum slabs were 1 mm long and were overfilled by the heating beam, ensuring a uniform illumination. The plasma heating beam was focused onto the target using an off-axis paraboloid mirror, and the line focus was formed by the addition of a cylindrical lens. The line focus was diagnosed by lowering the target to allow imaging the beam with an aspheric lens onto a CCD detector.

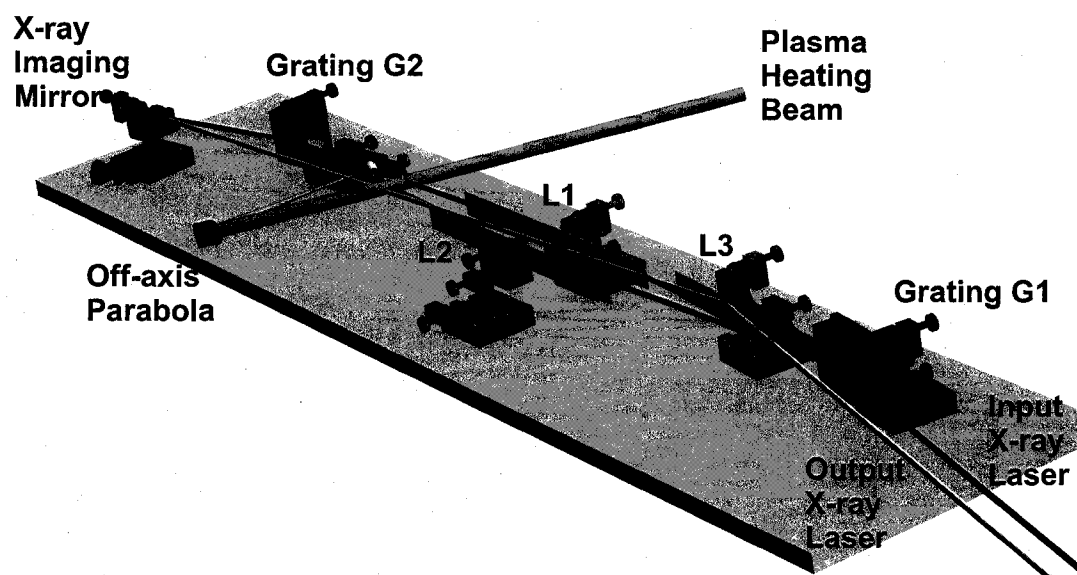


Figure 4.1: Schematic illustration of the Diffraction Grating Interferometer tailored to work at $\lambda = 14.7$ nm.

The Ni-like Pd soft x-ray laser probe used in this experiment produced laser pulses of few 10's of μJ with a typical duration in the range of 4.5 - 5.2 ps [4.23]. It was pumped by a sequence of a 600 ps FWHM, 1 J long pulse and a traveling wave, 13 ps FWHM, 5 J short pulse generated by the COMET laser [4.24]. The short duration of the soft x-ray laser pulse permits the acquisition of "snap-shots" of rapidly evolving plasmas, greatly reducing the blurring of interference fringes that occurs when the electron density profile changes significantly during the sampling period of the probe pulse, as discussed in section 2.5. This allows measurements to be performed close to the target surface as seen in the data presented in section 3.2 that showed the on-axis density depression for the case of the short heating laser pulse. The aluminum results presented in this chapter are the late times in the plasma evolution presented in that section. The synchronization of the heating and probe laser beams was possible because the two lasers originate from the same oscillator. An optical delay line was used to adjust the probing time with respect to the peak of the heating pulse.

4.2 Observation of anomalous fringe shifts in aluminum plasmas

The aluminum plasma was generated within the path of the zeroth order arm of the interferometer and the timing between the heating and probe beams was measured using fast photodiodes giving a precision of ~ 100 ps. By repeating the experiment with different time delays between the heating and probe laser beams, a sequence of interferograms that depict the plasma evolution were obtained. Figure 4.2 shows the late interferograms in the evolution of an aluminum laser-produced plasma. The large field of view of the interferograms, which is significantly larger than shown ($400 \mu\text{m} \times 600 \mu\text{m}$), allows the position of the reference fringes to

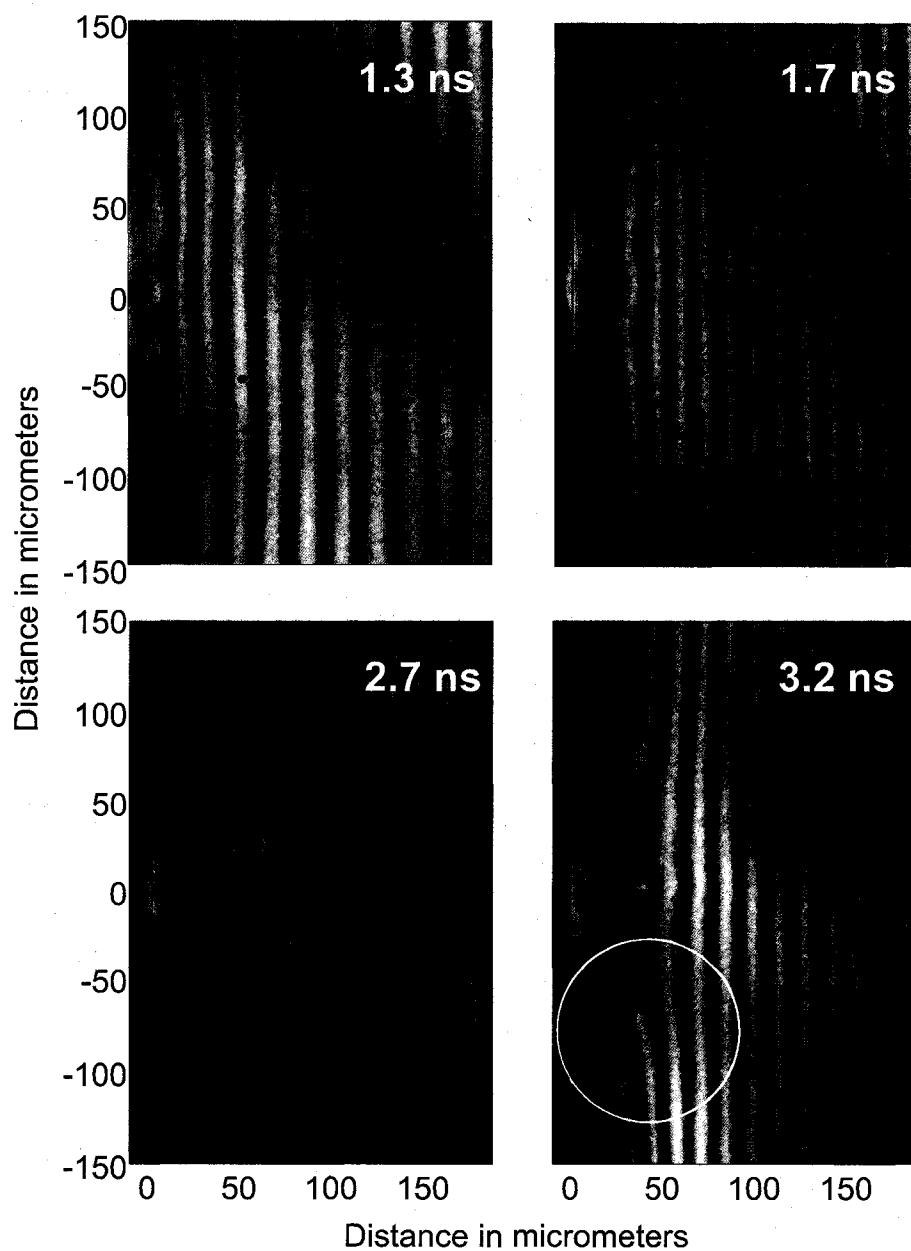


Figure 4.2: Sequence of soft x-ray laser interferograms ($\lambda = 14.7 \text{ nm}$) of Al line focus plasmas. The plasmas were generated by a 3.1 J heating beam focused into a $12 \mu\text{m} \times 3.1 \text{ mm}$ line focus. The times are measured respect to the peak of the 600 ps heating pulse. Fringes that bend toward the target are clearly observed in the last two frames in the periphery of the plasma and close to the target surface (yellow circle).

be determined reliably, by assuming that they follow straight lines connecting the fringes in the unperturbed regions where no plasma is present. The frames corresponding to the earlier times of the evolution (0–0.9 ns, Fig. 3.7) show a rapid lateral expansion of the plasma together with the formation of the on-axis density depression. At these times the fringes shift away from the target, even in the central region of the plasma where the on-axis depression is observed. In contrast, the four frames in Fig. 4.2 show interferograms with fringes that at the periphery of the plasma shift toward the target instead of away from the target. This phenomenon is indicative of an index of refraction greater than 1. Also, the region close to the target presents increased absorption, an indication of a colder plasma.

The fringe shift maps shown in figure 4.3 were calculated by measuring the displacement of the fringes relative to the fringe separation. At these late times, the interferograms do not show fringes in the first 25 μm closest to the target due to absorption. Three different cases can be distinguished in the fringe shift maps. Even though the shape of the fringe close to the target is remarkably different from the earlier shots shown in Fig. 3.7, with flatter fringes, the 1.3 ns map still shows positive fringe shifts that reach a maximum value of ~ 0.75 close to the axis of the heating laser beam. At this time the double-lobed shape of the plasma is still maintained very close to the target surface. At 1.7 ns the fringes are flattened even more and the fringe shift map shows maximums just above ~ 0.25 located in separate pockets close to the target and near the center of the plasma. Finally, the frame taken 1 ns later shows that the central region now has negative fringe shifts, reaching a value of -1. The Fringe shifts have now recovered the double-lobed shape, but this time in the opposite direction. The region with negative fringe shifts expands, becoming larger in the 3.2 ns frame where the fringe shift reaches a value of -1.5.

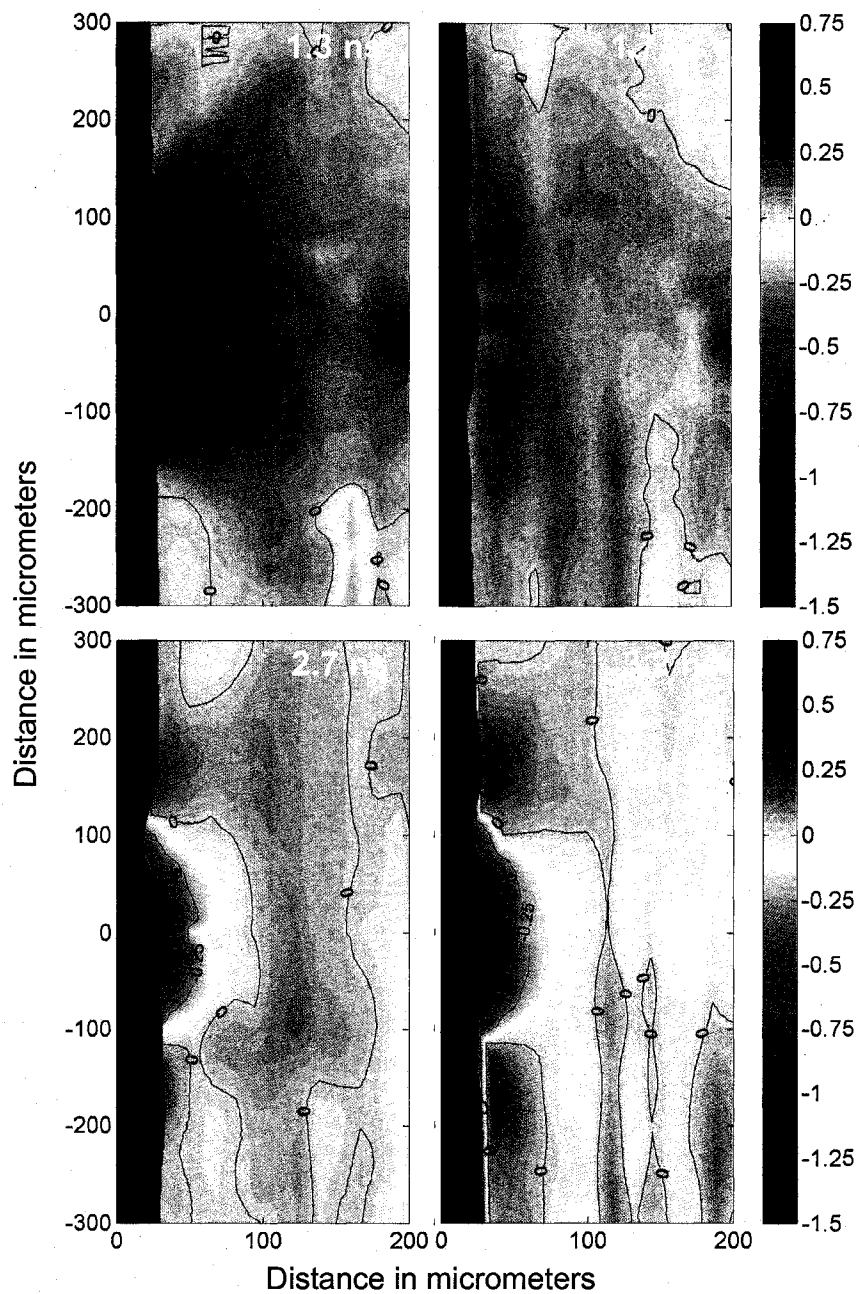


Figure 4.3: Fringe shift maps obtained from the interferograms in Fig. 4.2. The maps show that the regions where the largest densities were present now have negative fringe shifts. It is not possible to compute an electron density map from the fringe shift information because the assumption that only free electrons contribute is not valid.

In phase shift interferometry the number of fringe shifts, given by the difference in optical path length between the two arms of the interferometer,

$$N_f = \frac{1}{\lambda} \int_0^L (1 - \eta) dl \quad (4.1)$$

is negative when the index of refraction (η) of the plasma is greater than 1. The contribution of the free electrons to the plasma index of refraction is always less than 1, as determined by the formula

$$\eta = \sqrt{1 - \frac{n_e}{n_{crit}}} \quad (4.2)$$

where $n_{crit} = \frac{\pi}{r_e \lambda^2} = 5 \times 10^{24} cm^{-3}$ is the critical density for $\lambda = 14.7$ nm. An unrealistic negative electron density would be required to produce an index of refraction greater than one in plasmas where only free electrons contribute to the index of refraction. This suggests that to explain an index of refraction greater than one other contributions have to be considered. The contribution of the ions in the plasma has to be dominant and greater than one, in the region where negative fringe shifts are observed.

4.3 Interpretation of the anomalous fringe shifts in aluminum

The appearance of anomalous fringe shifts in the interferograms of aluminum plasmas (Figures 4.2 and 4.3) probed at 14.7 nm cannot be explained under the assumption of negligible bound electron contribution to the index of refraction. Under this assumption all the fringes in the interferogram can only shift in the same direction as dictated by Exp. (4.2) The negative fringe shifts were not observed in interferograms of plasmas generated with similar plasma heating beam conditions using several other target materials (Ti, Cr, Pd, Mo, Au). As an example, Fig. 4.4 shows 3 interferograms obtained from different target materials and all at the

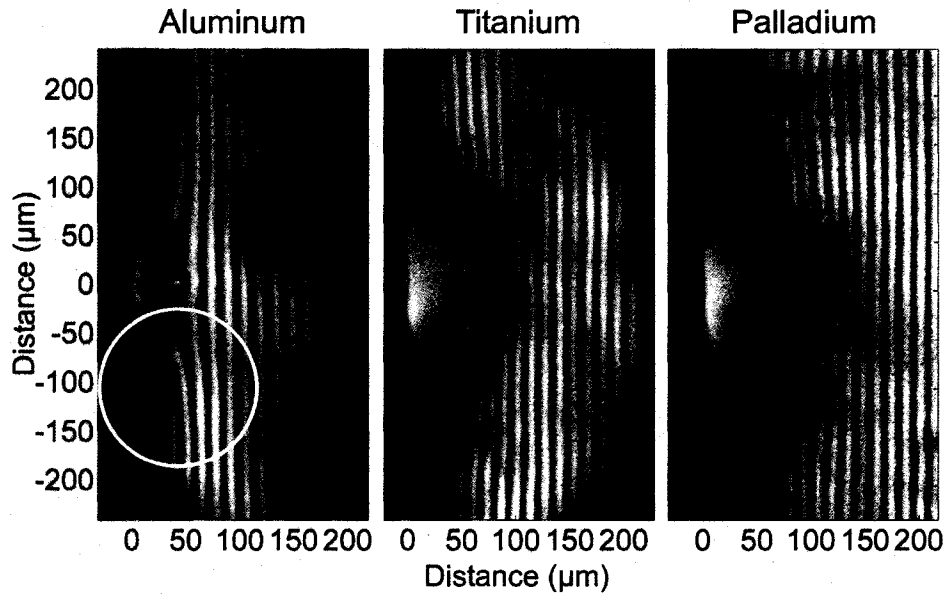


Figure 4.4: Comparison of interferograms obtained 3.2 ns after the peak of the heating laser pulse for Al, Ti and Pd targets. All the interferograms were created using the same heating conditions as the one used to create the Al interferogram sequence in Fig. 4.2. The striking difference in behavior is most noticeable in the circled area.

same time in the plasma evolution. The aluminum interferogram is the 3.2 ns shot taken from Fig. 4.2 and the titanium and palladium interferograms were obtained using the same irradiation conditions as that used for that aluminum sequence of interferograms. The titanium and palladium interferograms show only positive fringe shifts, and a relatively large region where the probe beam was absorbed near the target surface while the corresponding aluminum interferogram shows clear negative fringe shifts that must be caused by bound electrons contributing to the index of refraction.

The first bound electrons to be considered are those bound to neutral aluminum atoms. The index of refraction of materials at soft x-ray wavelengths are tabulated through the use of the scattering factors, as was explained in section 1.3.

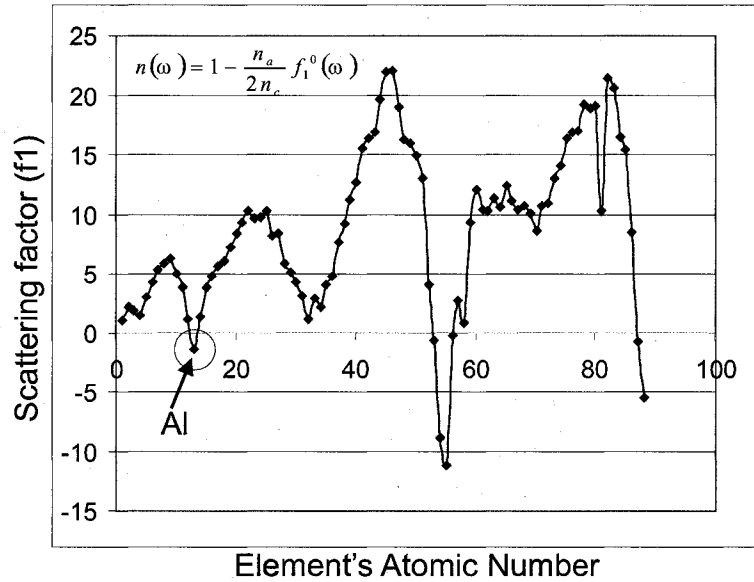


Figure 4.5: Scattering factor f_1^0 for the neutral atoms of the elements with atomic number ranging from 1 to 86. aluminum is the only in the region with $Z < 50$ that has $f_1^0 < 1$.

These tables [4.25, 4.26] give f_0^1 and f_0^2 for a wide range of photon energies starting at 30 eV. From the scattering factors it is easy to obtain the index of refraction through

$$\eta \simeq 1 - \frac{n_a}{2n_{crit}} f_1^0 \quad (4.3)$$

that indicates that a negative f_1^0 will result in an index of refraction greater than one. The values of the real part (f_1^0) of the scattering factors at 14.7 nm are plotted versus Z , the atomic number of the element in figure 4.5. From all elements with atomic number less than 54, aluminum is the only one that has a f_1^0 with a negative value [4.25, 4.26] due to the close proximity of the 84.4 eV photon energy to the Al L-shell absorption edge. Some elements with $Z \geq 54$, including I, Xe, Cs, Ba, Fr, Ra, Ac, also have a negative scattering factor at this wavelength. This suggests that the presence of significant densities of neutral Al

atoms will cause negative fringe shifts at 14.7 nm probe wavelengths. However, a significant density of neutral atoms would completely absorb the probe beam, due to their high photoionization cross section (f_2^0 is ~ 5 , and considering a density of $5 \times 10^{19} \text{cm}^{-3}$ gives an absorption length of $\sim 50 \mu\text{m}$ through $l_{abs} = \frac{\lambda n_c}{2\pi n_a f_2^0}$). The fact that the probe beam is not completely absorbed in the regions where the anomalous fringe shifts are observed indicates that the density of neutral atoms in this regions of the plasma should be very small and that the negative fringe shifts are instead caused by bound electrons in ions.

Therefore, to evaluate the contributions of bound electrons to the index of refraction, the real component of the index of refraction, f_1^0 is needed for the different ions present in the plasma. The following index of refraction calculation was performed by J. Scofield. For each ionization stage the continuum absorption cross sections were calculated using a Hartree-Slater code. The potentials were adjusted to make sure the L3 edges agreed with the experimentally measured edges [4.27, 4.28]. The absorption for the lines below the L3 edges were subsequently added to the continuum absorption. For Al II and AlIII the measured line positions and oscillator strengths from Aguilar *et al.* [4.27] were used. For AlIV the n=2 to n=3 and 2p to 4s line positions and line strengths were from Savukov *et al.* [4.28]. Using the absorption coefficient, f_2^0 , the real part of the index, f_1^0 , is then derived using the Kramers-Kronig dispersion relation, as discussed in section 1.3. This part of the index is the bound electron contribution, so then the number of free electrons was added to determine the total f_1^0 , as discussed by Henke *et al.* [4.25]. The “effective” f_Z^* value is defined as $f_Z^{bound} + f_Z^{free}$ where f_Z^{bound} is calculated as described above and f_Z^{free} is the number of free electrons corresponding to the ion of charge Z. The forward scattering supraindex (0) and real part (1) subindex are

omitted for clarity. The calculated values [4.29] for AlI - AlX are shown in table 4.1. The f_Z^* for AlXI-AlXIV are assumed to just be the value given by the number of free electrons.

Ion species	Species	f_Z^*
Neutral	AlI	-0.85
Ion Al1+	AlII	-4.19
Ion Al2+	AlIII	-3.54
Ion Al3+	AlIV	-1.80
Ion Al4+	AlV	0.84
Ion Al5+	AlVI	3.54
Ion Al6+	AlVII	5.30
Ion Al7+	AlVIII	6.73
Ion Al8+	AlIX	8
Ion Al9+	AlX	9.18
Ions Al10-13+	AlXI-AlXIV	10-13

Table 4.1: Calculated f_Z^* for free and bound electrons for aluminum atoms at 14.7 nm. The bound electrons in the first 5 ion species were found to significantly contribute to the index of refraction.

When the f_Z^* values differ from Z (the number of free electrons corresponding to the ion of charge Z) the contribution of the bound electrons is significant, and all ions with charge up to $Z=5$ are seen to make a significant contribution. These f_Z^* values were used to calculate the total plasma index of refraction through $\eta = (1 - \sum_Z \frac{n_Z f_Z^*}{n_{crit}})^{\frac{1}{2}}$, where n_Z is the density of ions with charge Z . If f_Z^* is negative, the combination of the bound electrons with the free electrons corresponding to this ion (Z) contributes to an index with a value greater than one. The computed negative values of f_Z^* for Al I-Al IV suggest that the negative fringe shifts observed at the late times are due to the presence of a relatively high density of these low charge ions. Moreover, all the ions up to AlVII make a significant contribution to the index of refraction. It should be noted that this phenomenon does not require a close resonance and affects a broad range of wavelengths due to numerous

bound-bound and bound-free transitions in many ionization stages, and so this effect should be present in plasmas created using different materials and probed at different wavelengths. This conclusion is supported by the observation of negative fringe shifts in Al plasmas at two different probe beam wavelengths: 13.9 nm [4.14] and 14.7 nm (the results presented herein).

To confirm this interpretation of the data, the 2-dimensional (2-D) ion and electron density distributions for the plasmas of Fig. 4.2 was computed with the hydro code LASNEX [4.16]. The simulations were performed by Steve Moon of Lawrence Livermore National Laboratory, using flux-limited heat transport, multi-group radiation diffusion, and a detailed hydrogenic configuration atomic model with non local thermodynamic equilibrium physics for temperatures above 50 eV. The simulations were conducted using the measured temporal and spatial profiles of the laser beam used to heat the plasma. Figure 4.6 shows 2-D maps of the computed electron density (contours) and the corresponding average ion charge distributions (colormaps).

The electron density distributions measured during the early times of the expansion are well reproduced by the code. The agreement includes the lateral expansion and the on-axis depression that have been discussed in section 3.2. The good agreement between the simulations and the experimental data gives confidence that the simulation reproduces well the plasma evolution and at the same time, from the simulations it is possible to check that at early times the plasma is hot and only highly ionized species are present whose bound electrons have a small contribution to the index of refraction. In contrast, at later times, corresponding to the frames of Fig. 4.2, the simulations show that the degree of ionization in the plasma periphery decreases as the plasma cools, resulting in the presence of significant concentrations of AlII-AlIV ions.

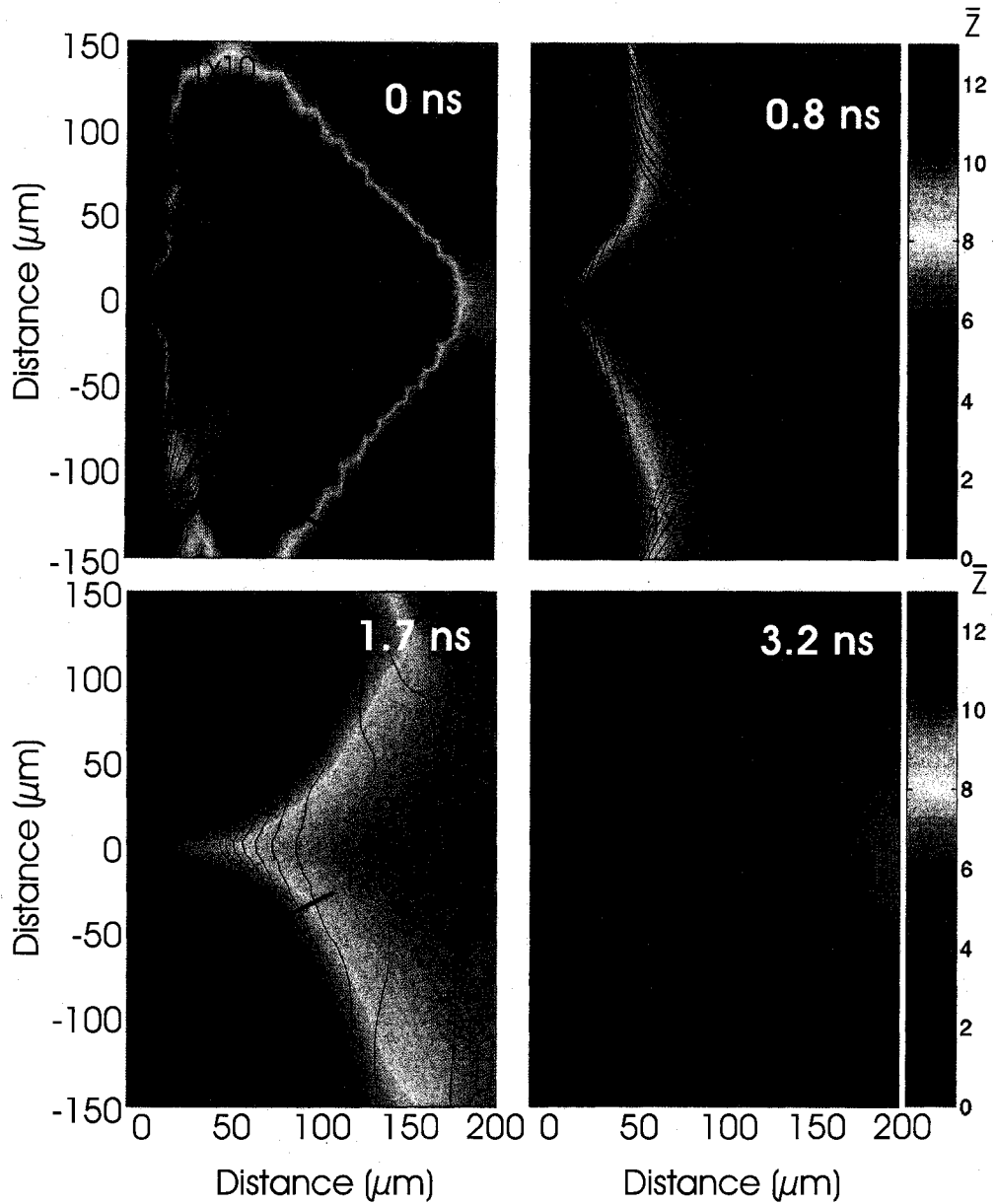


Figure 4.6: Sequence of simulated electron density contours and mean ionization distribution maps computed using the LASNEX code for an Al plasma created with the irradiation conditions of Fig. 4.2.

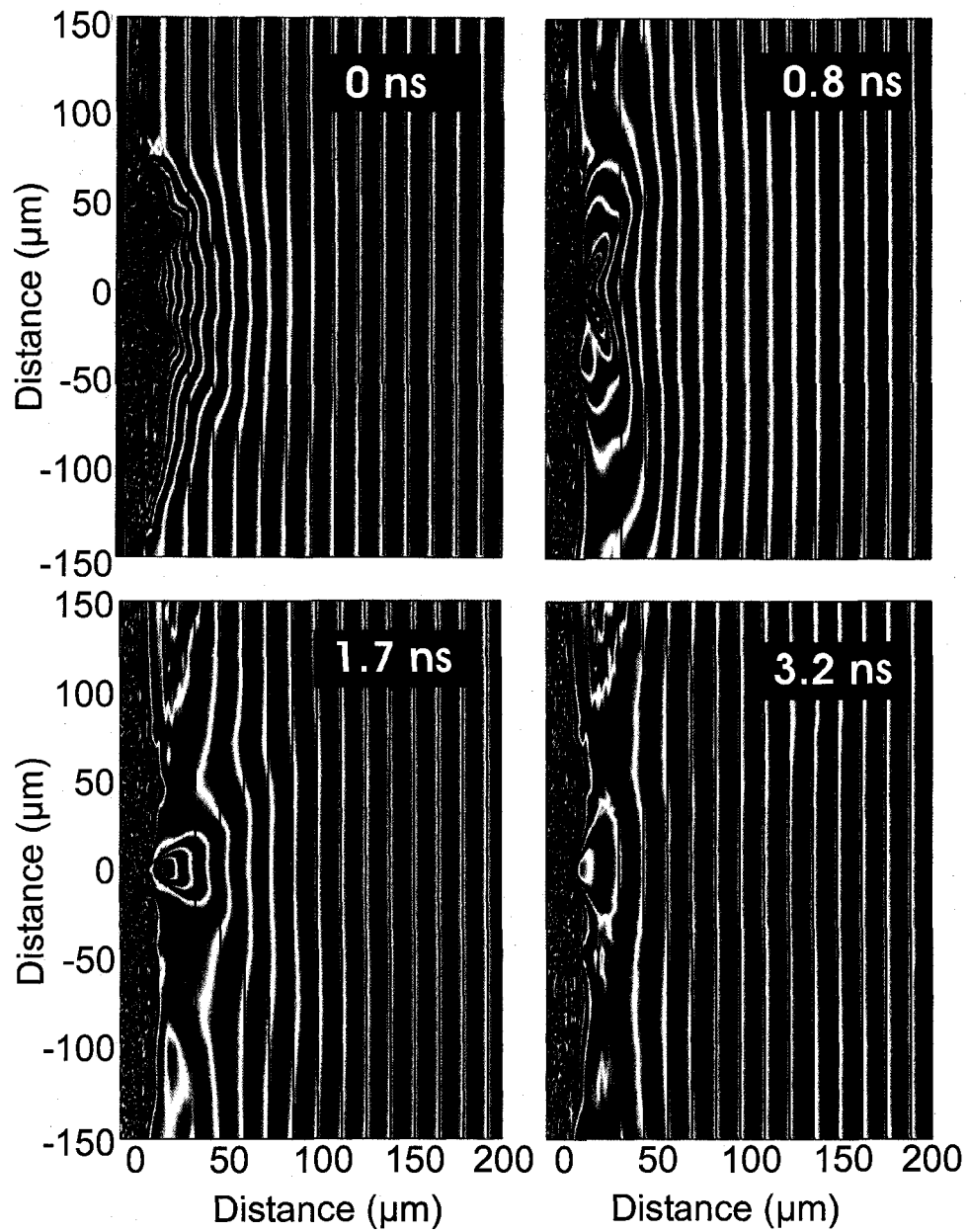


Figure 4.7: Synthesized interferograms computed using the calculated electron and ion densities from Fig. 4.6 and the calculated scattering factors for Al ions. The red lines indicate the position of the reference fringes.

The simulation results were used to synthesize the interferograms that are shown in Fig 4.7. These synthetic interferograms were calculated taking into account the contributions to the index of refraction from free electrons and Al ions using the computed “effective” f_Z^* factors and the electron density and ion density distributions computed with LASNEX. The synthesized interferogram corresponding to 0.8 ns delay shows the still evident central density depression and the lateral expansion observed in the measurements, and the late interferogram at 3.2 ns shows the observed negative fringe shifts in the periphery of the plasma, in good agreement with the experiment. In the simulations, the negative fringe shifts appear slightly earlier (at 0.8 ns) than in the experiment (1.1 ns) which could indicate that the cooling of the plasma in the simulations is slightly faster than in reality.

This demonstrates that for the case of the aluminum plasmas probed at $\lambda = 14.7$ nm, bound electrons contribute significantly to the index of refraction of multiply ionized plasmas. The significance of the result goes beyond this particular case, as this effect should happen at other soft x-ray wavelengths in the vicinity of absorption edges. The rest of the chapter will discuss the average atom method developed to calculate the index of refraction of plasmas, its application at different materials and different wavelengths to predict where the effect will be evident, and the experimental confirmation of these predictions.

4.4 Average Atom method

A method to calculate the optical properties of arbitrary plasmas at any wavelength was developed by W.R. Johnson [4.20]. The development of this method was motivated by the urge to be able to explain the observed anomalous fringe shifts. It is a modified version of the INFERNO average atom code [4.30]. The

INFERNO code has been used for many years to calculate the ionization conditions and absorption spectrum of plasmas under a wide variety of conditions. For finite temperatures and densities, the INFERNO code calculates a statistical population for occupation of one-electron Dirac orbitals in the plasma. The average atom method uses a non-relativistic version of INFERNO to calculate bound and continuum orbitals and the corresponding self-consistent potential.

The plasma is described by the Schrödinger equation

$$\left[\frac{p^2}{2m} - \frac{Z}{r} + V \right] u_a(\mathbf{r}) = \epsilon u_a(\mathbf{r}) \quad (4.4)$$

where the potential is divided the following way:

$$V(r) = \begin{cases} V_{dir} + V_{exch} & \text{inside the cell} \\ 0 & \text{outside the cell} \end{cases} \quad (4.5)$$

The direct part of the potential is obtained from the contribution to the charge from the bound electrons and from the continuum free electrons.

$$\nabla^2 V_{dir} = -4\pi(\rho_b + \rho_c) \quad (4.6)$$

and the exchange potential is given by the local density approximation

$$V_{exch} = \left(\frac{3}{\pi} \rho(r) \right)^{1/3} \quad (4.7)$$

The bound state contribution to the density is given by

$$4\pi r^2 \rho_b(r) = \sum_{nl} 2(2l+1) f_{nl} P_{nl}(r)^2 \quad (4.8)$$

where $P_{nl}(r)$ is the radial wave function and f_{nl} is the Fermi distribution function for a state with quantum numbers (nl) .

$$f_{nl} = \frac{1}{a + \exp[(\epsilon_{nl} - \mu)/kT]} \quad (4.9)$$

where μ is the chemical potential, and T is the temperature, and k is the Boltzmann constant. For continuum (free) electrons, the bound-state radial function is replaced by the continuum wave function with the corresponding substitution of the summation over levels with an integral over energies $P_d(r)$.

To ensure that each cell has Z electrons

$$Z = \int_{r < R} \rho(r) d^3r \equiv \int_0^R 4\pi r^2 \rho(r) dr \quad (4.10)$$

These equations are solved self consistently to obtain the chemical potential μ , the potential $V(r)$ and the electron density $\rho(r)$ that describe the average atom. To model the effect of incident light, a time dependent field is applied to the average atom. The vector potential used to describe the field is

$$A(t) = \hat{z} \frac{F}{\omega} \cos(\omega t) \quad (4.11)$$

By keeping only terms up to linear in F , a perturbed Schrödinger equation is found and solved to obtain a solution that then can be used to calculate the current and, by considering only the part of the current that is in phase with the driving field, the conductivity can be obtained. This is an average-atom version of the Kubo-Greenwood equation [4.31, 4.32] for the frequency-dependent conductivity of the plasma.

$$\mathbf{J} = \sigma(\omega) \mathbf{E} \quad (4.12)$$

From the conductivity, the complex dielectric function can be obtained by using the relation

$$\epsilon_r(\omega) = 1 + i \frac{4\pi\sigma(\omega)}{\omega} \quad (4.13)$$

The imaginary part of the complex dielectric function is proportional to the real part of the conductivity. The real part of the dielectric function can be found from its imaginary part using a Kramers-Kronig dispersion relation.

$$\Re[\epsilon(\omega)] = 1 - \frac{4\pi\Im[\sigma(\omega)]}{\omega} \quad \Im[\epsilon(\omega)] = \frac{4\pi\Re[\sigma(\omega)]}{\omega} \quad (4.14)$$

The complex index of refraction in terms of the complex dielectric function is

$$\eta + i\kappa = \sqrt{\epsilon}, \quad (4.15)$$

and then, the real and imaginary parts of the complex index of refraction are explicitly given in terms of the complex dielectric function

$$\eta(\omega) = \sqrt{\frac{\sqrt{(\Re[\epsilon(\omega)])^2 + (\Im[\epsilon(\omega)])^2} + \Re[\epsilon(\omega)]}{2}} \quad (4.16)$$

and

$$\kappa(\omega) = \sqrt{\frac{\sqrt{(\Re[\epsilon(\omega)])^2 + (\Im[\epsilon(\omega)])^2} - \Re[\epsilon(\omega)]}{2}} \quad (4.17)$$

4.5 Anomalous fringe shifts at 46.9 nm

The first step in the search for materials that could have an index of refraction greater than one at 26.5 eV (46.9 nm) is to look in the Henke tables [4.25] for neutral materials that have an absorption edge near 26.5 eV. Tin ($Z=50$) is one to stand out as a candidate with the $N_44d^{3/2}$ and $N_54d^{5/2}$ edges at 24.9 and 23.9 eV. The next step is to check if, for the materials found, the f_1^0 coefficient is negative at 26.5 eV. Finding a negative f_1^0 values for neutral material is usually an indication that a plasma of that material with a low ionization will have negative f_1^0 as well, as was found to be the case for the aluminum plasmas at 84.4 eV (14.7 nm).

However the lowest published value for f_1^0 in the Henke tables is at an energy of 30 eV. Since the absorption coefficient f_2^0 has published values down to 10 eV, it is possible to use the Kramers-Kronig dispersion relation to calculate an estimate of f_1^0 below 30 eV. The f_1^0 values above 30 eV from Henke were used to compare with the calculations and to adjust a constant offset. This was done for tin (Sn) and other nearby materials with Z between 42 and 51. Figure 4.8 shows an estimate of f_1^0 for various materials. Molybdenum (Mo), palladium (Pd) and antimony (Sb) have positive f_1^0 at 26.5 eV even though Mo and Pd have negative values at other energies while Sb stays positive for the energies shown in the figure. Silver (Ag) and tin (Sn) both have negative values of f_1^0 near 26.5 eV. Ag has negative values over the entire range from 10 to 35 eV while Sn is negative from 21 to 60 eV. For Sn f_1^0 is estimated to be -1.8 while for Ag f_1^0 is estimated to be -2.1 at 26.5 eV. Both Ag and Sn look to be promising candidates to do further calculations and experiments.

For neutral tin, the absorption coefficient at the 46.9 nm wavelength corresponding to the Ne-like Ar laser is too high to permit probing through 1 mm long plasma, but the absorption edge moves to higher energy when the material is ionized. From the Dirac-Slater calculations of Scofield [4.15] the ionization potential of the outer electron for singly ionized tin is 12.9 eV and doubly ionized is 30.1 eV. Doubly ionized tin looks promising as a candidate to show anomalous fringe shifts because the 26.5 eV X-ray laser would not have enough energy to photo-ionize Sn III and therefore the absorption coefficient will be much smaller than for neutral tin. Also, from [4.33], Sn III has 3 absorption lines at 26.72, 27.58, and 28.03 eV that have been measured experimentally. These are the $4d^{10}5s^2\ ^1S_0 - 4d^95s^25p^1\ ^3P_1, ^1P_1, ^3D_1$ lines. The 26.5 eV Ne-like soft x-ray laser is situated on the low

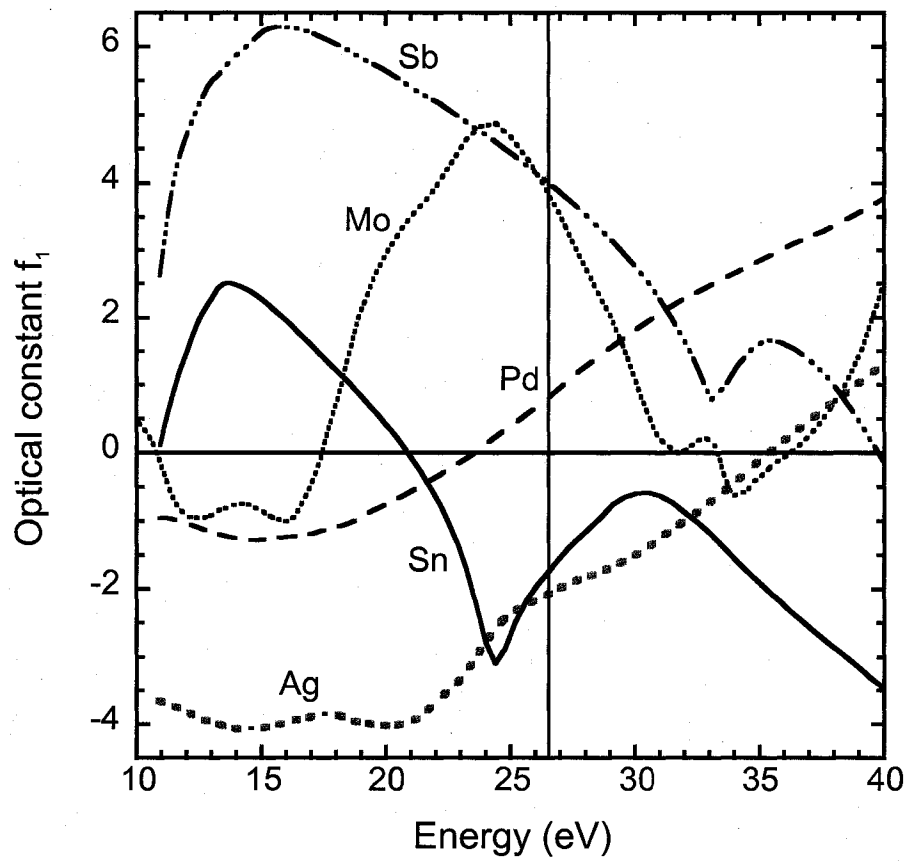


Figure 4.8: Optical constant f_1^0 versus photon energy for various neutral materials. These values are an extrapolation of the Henke tables to lower energy.

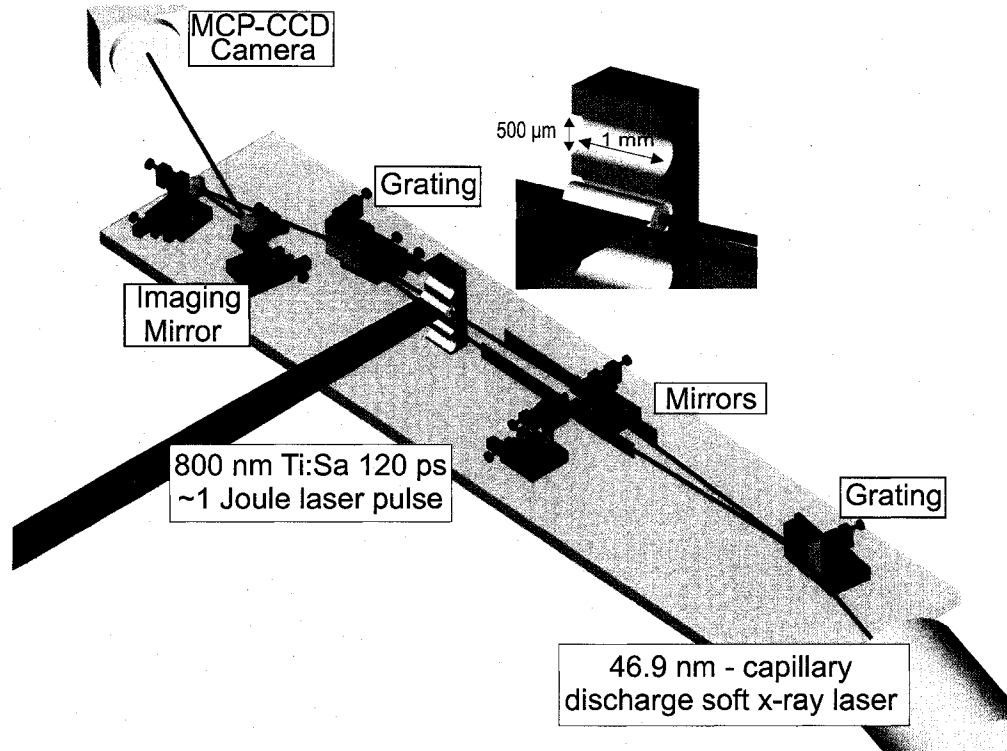


Figure 4.9: Experimental setup showing the Diffraction Grating Interferometer and detailed schematic of the $500 \mu\text{m} \times 1000 \mu\text{m}$ semi-cylindrical targets used.

energy side of these strong lines, so the lines should have a negative contribution to the f_1^0 value at this energy.

4.6 Plasma interferometry setup for the 46.9 nm experiments

The calculations suggested that anomalous fringe shifts should be observed in tin plasmas at a probe wavelength of 46.9 nm. To conduct plasma interferometry experiments at this wavelength, an experimental setup very similar to the one used for the aluminum plasmas at 14.7 nm of section 4.1 was used. It comprises the amplitude division Diffraction Grating Interferometer [4.7,4.22] described in detail in section 2.4 combined with a 46.9 nm table-top Ne-like Ar capillary discharge laser [4.34] that was described in section 1.4.1. The experimental set up is illustrated in

Fig. 4.9. The plasma was generated by irradiating a 1 mm long semi-cylindrical target with an 800 nm wavelength laser pulse of 120 ps (FWHM) and up to 1 J of energy. A line focus typically ~ 1.7 mm long and $310 \mu\text{m}$ wide, resulting in an irradiance of $\sim 1.3 \times 10^{12} \text{ W cm}^{-2}$, was formed in the target plane using the combination of a 7 m focal length spherical lens and a variable cylindrical lens created by combining a positive and a negative 1 m focal length cylindrical lenses placed a few cm apart. The line focus shape and the intensity of the heating beam in the target plane were monitored on every shot by imaging the reflection off a 4 % beam splitter onto a CCD camera. The target consisted of a pure slab of the material chosen, with semi-cylindrical cavities $500 \mu\text{m}$ in diameter machined on the front surface as shown in the detail in Fig. 4.9. The size of the slab was $1 \text{ mm} \times 4 \text{ mm} \times 4 \text{ cm}$ and the material used had a purity of at least 99.9 %. This target geometry combined with a relatively wide line focus irradiation generated a hot dense plasma that converged on the axis of the cavity and that lasted several ns due to new material emanated from the target walls [4.35]. The plasma remains sufficiently dense to produce measurable fringe shifts late in the evolution when it recombines into ions with low charge states following expansion and cooling. This makes the anomalous fringe shifts more evident and easier to observe than would be the case in a flat slab target laser-created plasma experiment. The plasma and the corresponding fringe pattern was imaged with $\sim 25\times$ magnification using Sc/Si multilayer optics [4.36] onto a Microchannel plate charge-coupled device (MCP-CCD) detector combination. The compact 46.9 nm Ne-like Ar capillary discharge-pumped laser, discussed in section 1.4.1, generated pulses of ~ 1 ns duration and energies of ~ 0.1 mJ. The soft x-ray laser was laser triggered achieving a measured jitter of ~ 1 -2 ns that increased the yield of the experiment.

4.7 Anomalous fringe shifts in tin plasmas probed at 46.9 nm

Anomalous fringe shifts were also observed in tin plasmas. Figure 4.10 shows three interferograms taken at different times during the evolution of tin plasmas. At 2.7 ns after the arrival of the heating laser pulse the creation of a concentrated region of dense plasma is observed near the geometrical center of the groove. This dense plasma region is formed by the convergence of the plasma that is emanated from the target wall throughout the life of the plasma. A complete analysis of the dynamics of the plasmas generated inside semi-cylindrical grooves is outside the main scope of this work but carbon and aluminum plasma dynamics are discussed by Purvis *et al.* [4.35]. At this relatively early time in the evolution, the plasma is still hot and highly ionized, so the contribution of bound electrons to the index of refraction (and therefore to the fringe shifts) can be neglected. All the fringes shift towards the right of the reference fringes. Under the assumption of negligible bound electron contribution it is possible to compute an electron density map of this plasma, resulting in a peak density of $2 \times 10^{19} \text{ cm}^{-3}$.

Later in time, starting around 20 ns after plasma irradiation (the frame shown was taken at 21.8 ns), the probe beam is nearly completely absorbed inside the cavity. This is because the plasma present in this region cools down allowing photo ionization of the plasma by the probe beam. The once greatly disturbed fringes are now less shifted, an indication that the index of refraction is now close to 1. Such fringe behavior indicates that either the plasma density has decreased to very low values, or that the bound electrons contribute significantly to the index of refraction and compensate for the contribution of free electrons resulting in an index of refraction close to one. If the latter was the dominant cause, it would be expected that as the bound electron contribution becomes more important, the

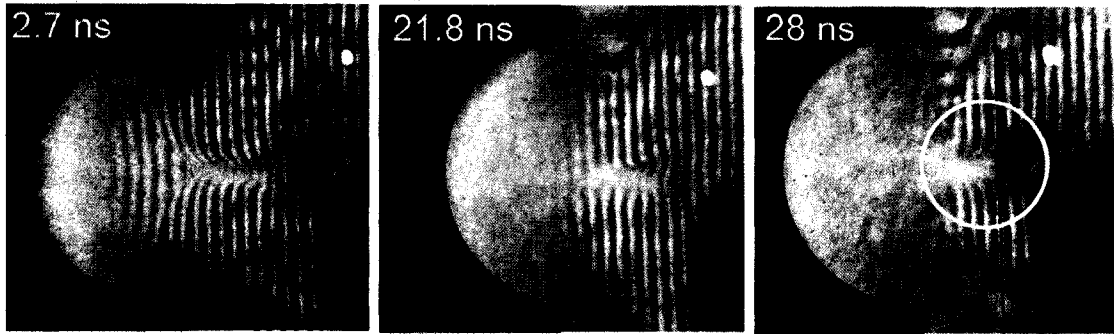


Figure 4.10: Soft x-ray interferograms corresponding to three times during the evolution of Sn plasmas generated by illuminating a 500 μ m diameter Sn semi-cylindrical groove with a $\sim 1.3 \times 10^{12} \text{ W cm}^{-2}$, 800 nm, 120 ps laser beam. The early shot (4.5 ns from the heating beam) shows a plasma for which the fringes shift to the right, while the later frame (33 ns) shows fringes that bend to the left of the reference line (drawn), an indication of an index of refraction greater than one.

fringe shift should be reversed. The interferogram corresponding to a time delay of 28 ns on Fig. 4.10 shows even higher absorption, now extending to the region of the density build up, at the geometrical axis of the groove. At this time, and in this region, the interference fringes are observed to bend toward the target, indicating an index of refraction greater than one. The black vertical line drawn on this last frame represents the position of a reference fringe in the absence of plasma. This clearly shows that the fringes are shifting in the opposite direction as expected if only free electrons were contributing to the index of refraction. A naive interpretation of the results would yield an unphysical negative electron density.

The scattering factor f_2^0 for SnIII is estimated by using the neutral absorption coefficient published in the Henke tables for energies above the calculated photo-ionization edge at 30 eV. This was combined with a multi-configuration Dirac-Fock calculation by J. Scofield [4.37] for the low energy 5s-5p lines near 5 and 10 eV, and the measured 4d-5p lines near 27 eV [4.33]. Then this absorption coefficient was used in the Kramers-Kronig dispersion relation to determine the optical constant

f_1^0 versus photon energy, as shown by the dotted line in Fig. 4.11. At the 26.5 eV energy of the Ne-like Ar soft x-ray laser line f_1^0 SnIII was estimated to be -13, which makes the index of refraction larger than one. The value for f_1^0 would be 2 (2 free electrons) if only the free electrons contributed to the index of refraction. The most important contribution to f_1^0 at this energy is from the measured 4d-5p lines at 26.72, 27.58, and 28.03 eV [4.33].

The second method used to estimate the index of refraction for the tin plasma is to use the new average atom code described in section 4.4. For the model, a tin plasma with an ion density of 10^{20} cm⁻³ and a temperature of 4 eV was chosen. These conditions produce a plasma with a mean ionization, \bar{Z} , of ~ 2 . This was found by calculating the mean ionization of the plasma to be 1.49, 1.98, 2.40, and 4.25, for the electron temperatures of 3, 4, 5, and 10 eV. The solid line in Fig. 4.11 shows the optical constant f_1^0 versus photon energy calculated by the average atom code. This is compared with the calculation of f_1^0 for SnIII described above, shown by the dotted line. The agreement between the two methods is excellent in the region near 26.5 eV. At 26.5 eV the average atom code predicts $f_1^0 = -10$. It is somewhat fortuitous that the average atom calculations have the strong 4d-5p absorption line within 0.1 eV of the experimentally measured values since normally the calculation results have to be shifted to ensure that the relevant absorption features line up [4.18, 4.19]. This result gives confidence on the Average Atom method to predict the index of refraction of plasmas but underscores the importance of having spectroscopic experimental data together with the calculations to accurately predict f_1^0 and this data is not always available in the literature.

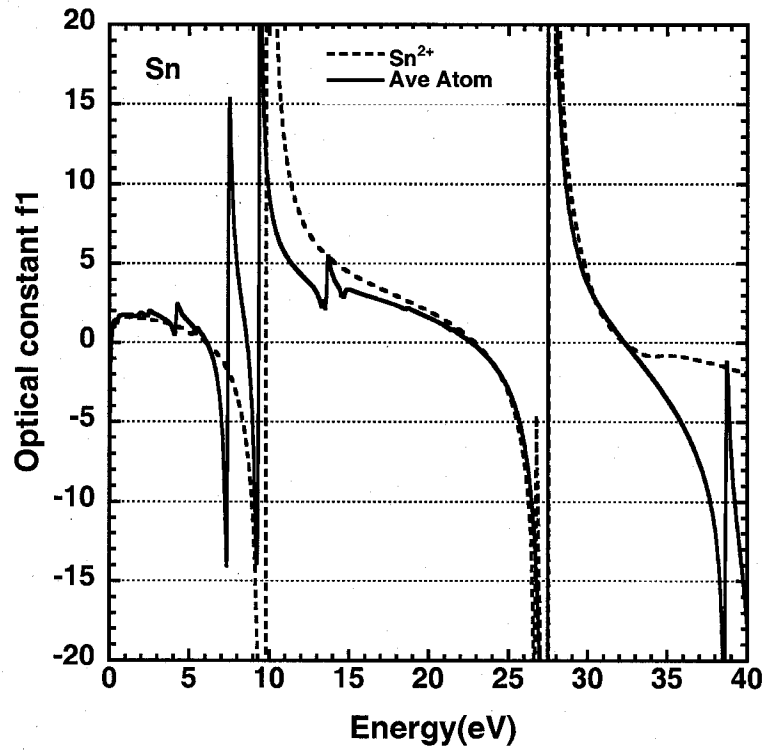


Figure 4.11: Optical constant f_1^0 versus photon energy calculated directly for SnIII (dotted line) and by the average atom code (solid line) for a Sn plasma with an ion density of 10^{20} cm^{-3} , a temperature of 4 eV, and $\bar{Z} = 1.98$.

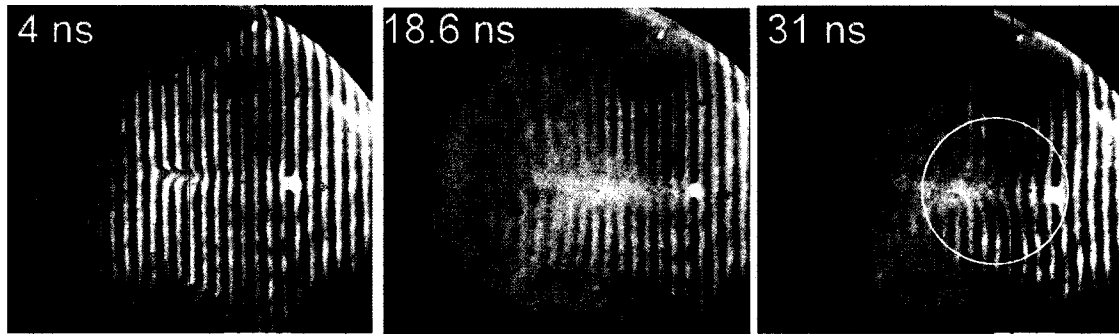


Figure 4.12: Soft x-ray interferograms of a Silver plasma, the experimental conditions are the same as those used to obtain the interferograms in figure 4.10. Anomalous fringe shifts are clearly observed in the late stages of the evolution. The black line in the 31 ns frame represents the position of the reference fringes.

4.8 Anomalous fringe shifts in Silver plasmas probed at 46.9 nm

Similar results to those in tin plasmas were obtained for Silver plasmas also created inside semi-cylindrical cavities. Figure 4.12 shows three interferograms corresponding to different times during the evolution of a Silver plasma. At 4 ns after the arrival of the heating laser pulse, the creation of a concentrated region of dense plasma is again observed. At this time only the probe beam that travels close to the target is absorbed.

Later in time, once again around 20 ns after plasma irradiation (the frame shown was taken at 18.6 ns), more absorption is observed along with a flattening of the fringes. At this point the contribution from the free electrons is probably being compensated by the bound electrons in the low charge ions. The interferogram corresponding to a time delay of 31 ns on Fig. 4.12 shows similar absorption but now the interference fringes are observed to bend toward the target, to the left of the black reference line drawn as a guide, indicating an index of refraction greater than one.

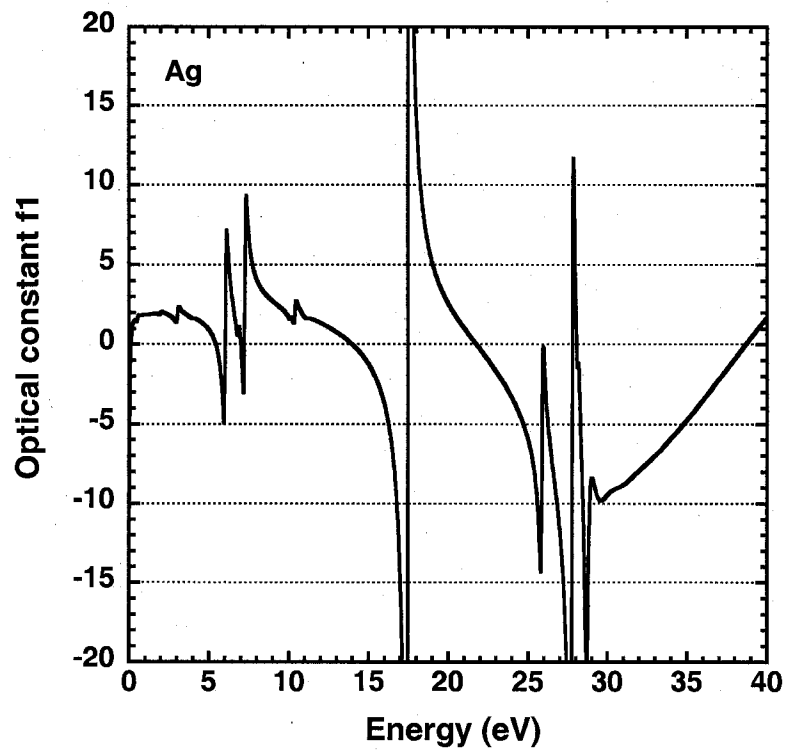


Figure 4.13: Optical constant f_1^0 versus photon energy calculated by the average atom code for a Ag plasma with an ion density of 10^{20} cm^{-3} , a temperature of 4 eV, and $\bar{Z} = 2.08$.

Average atom calculations of Ag plasmas with ion density of 10^{20} cm^{-3} and a temperature of 4 eV were performed. Under these conditions $\bar{Z} = 2.08$ indicates a doubly-ionized plasma and Fig. 4.13 shows the predicted optical constant f_1^0 versus photon energy. The structure is more complicated than for Sn because of multiple strong lines but the average atom code predicts f_1^0 to be -7 at 26.5 eV. It also predicts that f_1^0 will be less than zero from 21.8 to 27.8 eV and 28.1 to 38.6 eV. However, there is substantial variation in the magnitude of f_1^0 over this range. In the absence of experimental data on the positions of the absorption lines there is less confidence in the absolute position of the energy scale. But the calculation definitely shows that AgIII should be responsible for the anomalous dispersion observed. There is insufficient experimental data to estimate the f_1^0 value for Silver plasmas with confidence as described above for tin, but based on calculations, doubly-ionized Silver will be expected to have 4d-4f and 4d-6p lines in the 25 to 30 eV region that could result in a negative f_1^0 value at 26.5 eV. In addition the photo-ionization absorption edge for doubly-ionized Silver is at 35 eV, which means absorption in the Ag III plasma should be small at 26.5 eV.

4.9 Anomalous fringe shifts in carbon plasmas probed at 46.9 nm

Carbon plasmas were also created and probed inside semi-cylindrical targets, taking advantage of the same setup used for the tin and Silver plasma experiments. For the case of Carbon the interferograms obtained clearly show regions with an index of refraction greater than one, both at early and late times in the evolution. Figure 4.14 shows interferograms corresponding to two different times during the evolution of Carbon plasmas. The 5 ns frame shows interference fringes with maximum shifts on-axis due to the convergence of the plasma produced by irradiating

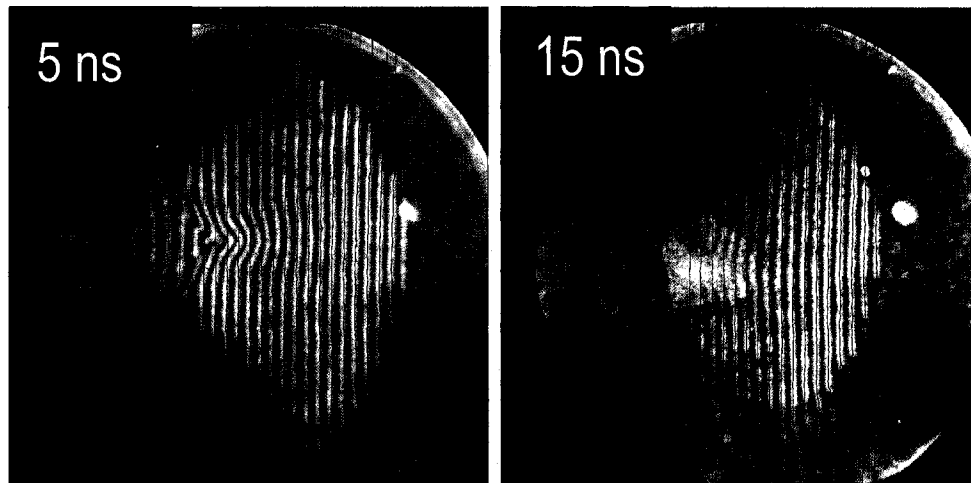


Figure 4.14: Soft X-ray interferograms taken at 5 and 15 ns in the evolution of a Carbon plasma created inside a 500 μm diameter semi-cylindrical groove with an irradiance of $\sim 1 \times 10^{12} \text{ Wcm}^{-2}$ was formed at the target plane, using the same setup as described above.

the walls of the semi-cylindrical target. At this time, anomalous fringe shift are observed at the bottom of the groove. The 15 ns frame shows absorption of the probe beam that indicates a colder plasma and the now familiar anomalous fringes that can be seen on the semi-cylinder's geometrical axis. To more clearly display the anomalous fringe shifts, Fig. 4.15 shows two-dimensional maps of the number of fringe shifts obtained from these interferograms. The plasma at the axis of the cylindrical groove in the 5 ns frame produces approximately one fringe shift in the direction compatible with the free electron approximation, which corresponds to $\sim 5 \times 10^{19} \text{ cm}^{-3}$. Here it is reasonable to assume that only free electrons contribute to the index of refraction because this region is relatively hot and high ions should dominate.

The fringes closer to the target, at the bottom of the semi-cylindrical groove, shift to the left of the reference fringes (black lines superimposed on the image),

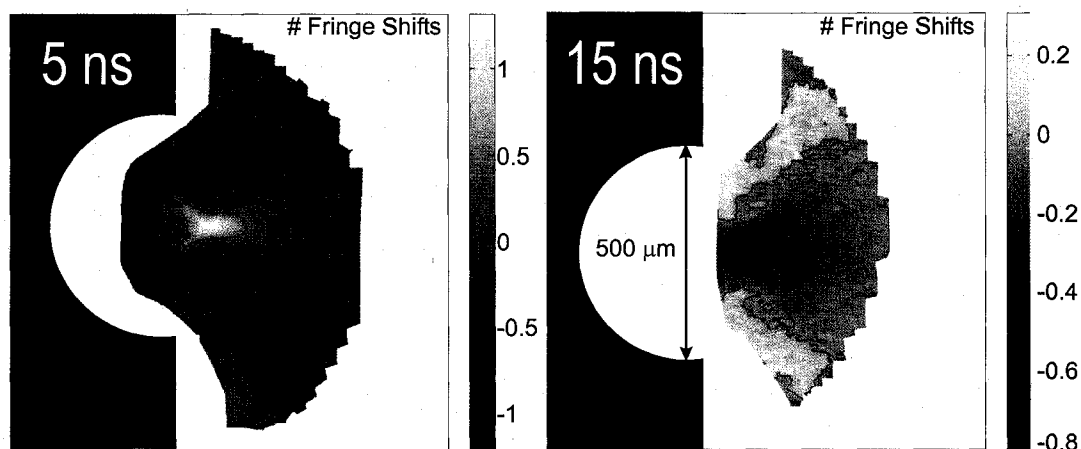


Figure 4.15: Number of fringe shifts computed from the interferograms in Fig. 4.14.

producing approximately one negative fringe shift. Later in time, the 15 ns interferogram in Fig. 4.14 shows a larger region where the probe beam is absorbed now completely filling the target cavity. Very little fringe shifts are observed overall except on the axial region that previously had the highest density, now all the fringes bend toward the left of the reference lines and reaching almost one fringe shift (-0.8). The regions with anomalous fringe shifts are always located close to the regions with high absorption, suggesting that the low ionized atoms are the cause of this anomalous index of refraction.

Average atom modeling of Carbon plasmas was performed by W. Johnson to determine the source of the bound electron contribution. A Carbon plasma with an ion density of 10^{20} cm^{-3} was used to model. By varying the temperature of this plasma through the values 3, 6, 10 and 30 eV the mean ionization varied through the values $\bar{Z}=0.96, 1.97, 2.92,$ and 3.95 . The results of the calculations are plotted in Fig. 4.16. To adjust an overall shift in the energies, the curve was offset to match the available experimental energy level data.

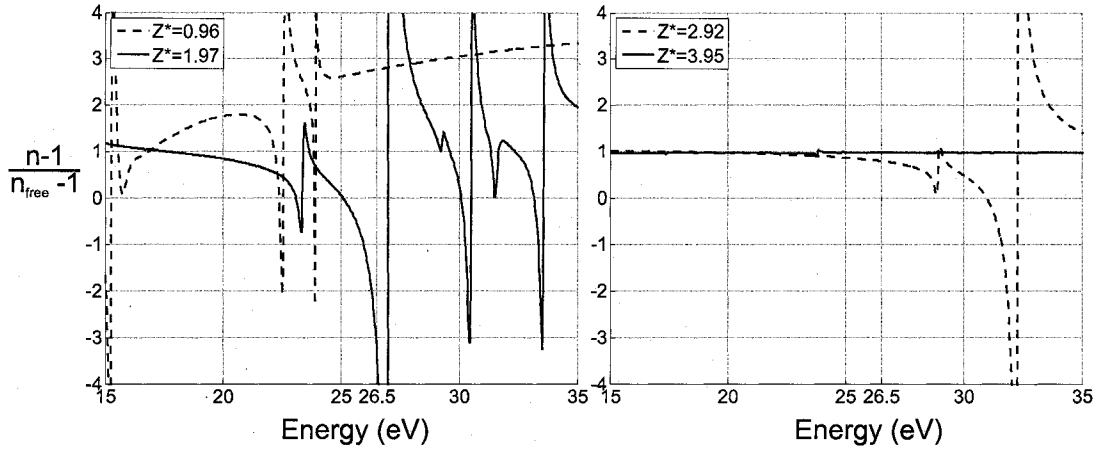


Figure 4.16: Index of refraction for Carbon plasmas computed using the Average Atom code. The plasma used had a density of 10^{20} cm^{-3} . A value of $(\eta-1)/(\eta_{free}-1)$ of 1 indicates that the contribution is solely due to free electrons.

The ratio $\frac{n-1}{n_{free}-1}$, plotted in Fig. 4.16, gives an estimate of how far the calculated index of refraction deviates from the approximation of only free electron contribution. When the ratio is one, the total index of refraction is that of the free electrons so the contribution of bound electrons is null. If the ratio is larger than one, the free and bound electrons are contributing with the same sign to the index of refraction, this can produce an overestimation of the electron density. For ratios smaller than one their contribution is opposite, but only for a value smaller than zero the bound electrons dominate the free electrons and anomalous fringe shifts would be observed in an interferogram.

The calculated ratio is larger than one for singly ionized carbon, but this will not show in the soft x-ray laser interferograms since the probe beam would be absorbed, the absorption edge is at 24.4 eV. As stated before, the region close to the target where the absorption is evident probably has a large population of neutral and singly ionized carbon atoms. For doubly ionized Carbon, there is a significant amount of structure with the ratio taking negative values for several

energy intervals, in particular close to the 26.5 eV region. The ratio approaches a value of one for triply and quadruply times ionized Carbon plasma, with a strong structure near 30 eV for triply ionized, but without a major contribution from the bound electrons at 26.5 eV. This suggests that the observed anomalous fringe shifts in carbon groove plasmas are a consequence of the dominant contribution of bound electrons from doubly ionized carbon ions to the index of refraction.

The presence of regions with anomalous fringe shifts in an interferogram does not necessarily preclude all measurement of the electron density. A validation of the different regions can be done checking the mean ionization obtained from hydrodynamic simulations. HYDRA simulations of the Carbon plasmas done by M. Purvis [4.35] produced ionization maps for the experimental conditions. Then a contour that delimits the $\bar{Z}=3$ was superimposed on the interferograms. This can be seen in the interferograms depicting the complete evolution of the Carbon plasmas shown in Fig. 4.17. The 1.3 ns frame shows a region that cannot be resolved due to motional blurring. The region to the right of the thin contour lines corresponds to the simulated plasmas with mean degree of ionization larger than 3. In these regions, that include the zone of high density build-up, the approximation that only free electrons contribute to the index of refraction should be valid and therefore the electron density maps can be expected to be accurate. The contour line moves to the right as the plasma recombines, leaving clearly negative fringe shifts to its left. The late time interferograms do not include the calculations because the HYDRA simulations were not able to produce results at these late times in the evolution. But the 10 ns frame shows the flattening of the fringes, similar to the one observed around 20 ns for tin and silver plasmas and the 15 ns frame shows the negative fringe shifts on the cavity's axis. It is then obvious

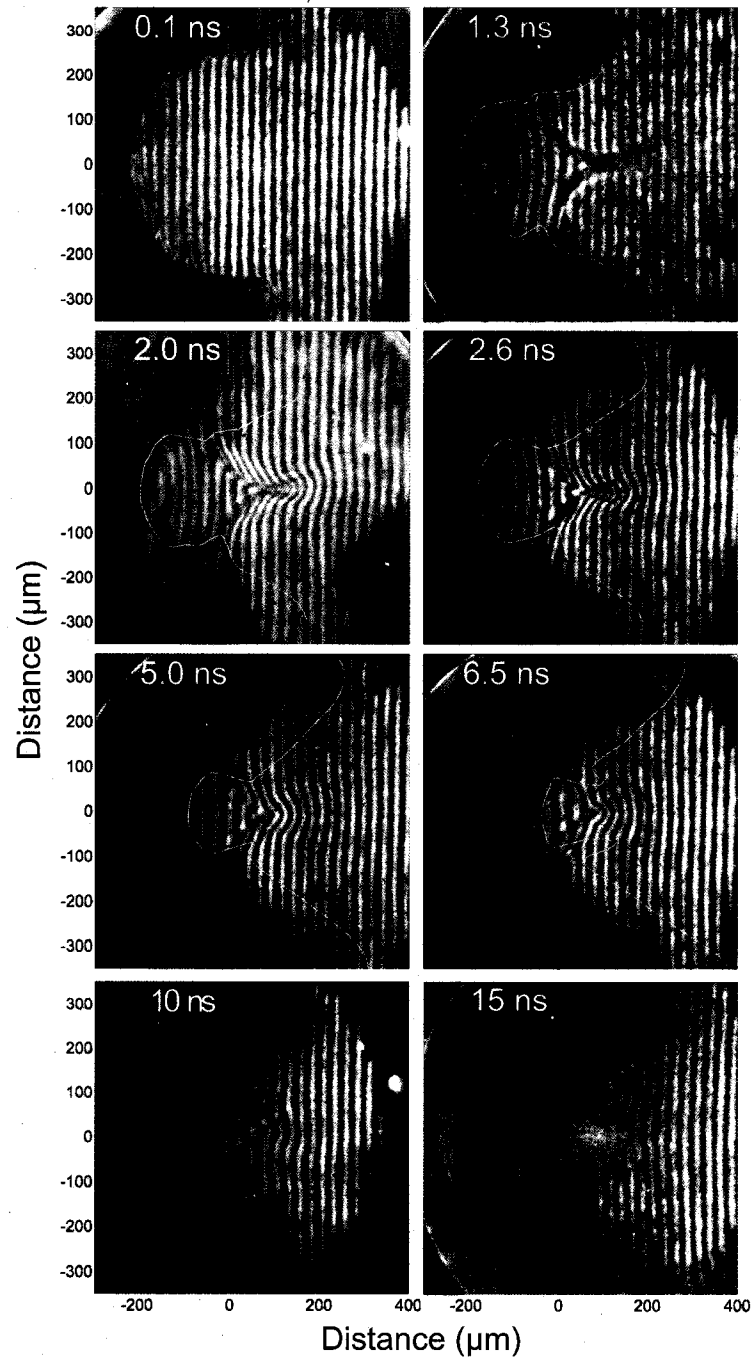


Figure 4.17: Complete sequence of interferograms of Carbon plasmas created inside a $500\ \mu\text{m}$ diameter semicylindrical groove. The white contours indicate the region in the plasma where the mean ionization is higher than 3. These contours were created using simulation results from the HYDRA code.

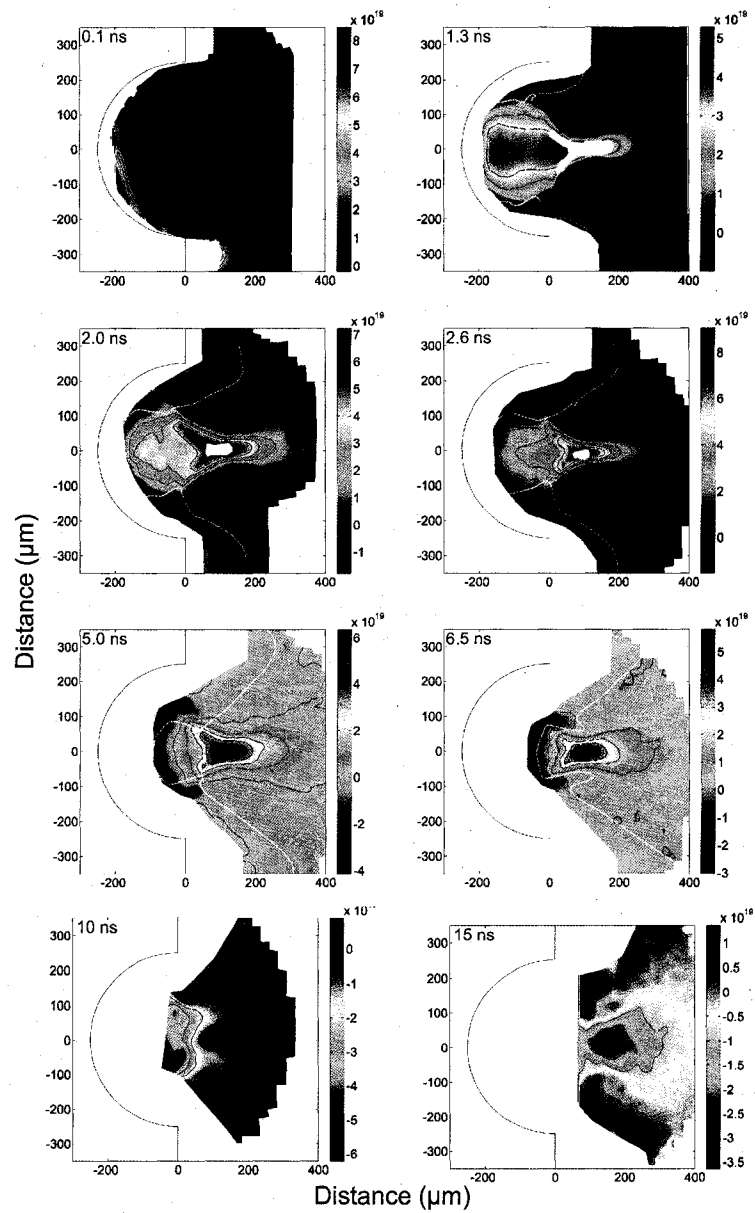


Figure 4.18: Complete sequence of density maps obtained from the interferograms in Fig. 4.17. The white contours indicate the region in the plasma where the mean ionization is higher than 3. Outside these contours unrealistic negative electron density values were measured.

that valid density maps cannot be obtained from these two late time frames. The density maps are shown in Fig. 4.18 where the $\bar{Z}=3$ contour is drawn in white. The high maps show that the density build up region, that is the region of interest of these plasmas, is away from the contour line. In fact, HYDRA predicts that this region has a mean ionization of $Z \sim 5$ which means that it is valid to assume that only the free electrons contribute to the index of refraction and that the density maps can be calculated.

4.10 Cu, Al and Mo plasmas probed at 46.9 nm

As important as finding materials in which the bound electrons contribute to the index of refraction is to find materials where the approximation of only free electron contribution is valid. Or what is equivalent, to find wavelengths at which it is possible to probe certain materials with confidence that it is possible to obtain electron density measurements from the fringe shift information. Making use of the setup described in the previous sections, but changing the target material, several plasmas were created and probed focusing on the late times in the evolution trying to detect the presence of anomalous fringe shifts. The materials tested (Cu, Al, Mo) did not present negative fringe shifts. As an example, Figure 4.19 shows 3 frames in the evolution of copper plasmas, an early shot that presents a very disturbed fringe pattern due to the density build-up on-axis, a shot close to 20 ns (shown 17.2 ns) that shows a flattening of the fringes combined with significant absorption and a late shot at 28.6 ns that does not show negative fringe shifts.

Average atom computations for copper plasmas were done using a density of $1 \times 10^{20} \text{cm}^{-3}$ and temperatures of 2,5,10,20 eV that resulted in a mean ionization of 0.84, 2.16, 3.74, and 6.24. The plots of the ratio $\frac{1-\eta}{1-\eta_{free}}$ in figure 4.20 show a

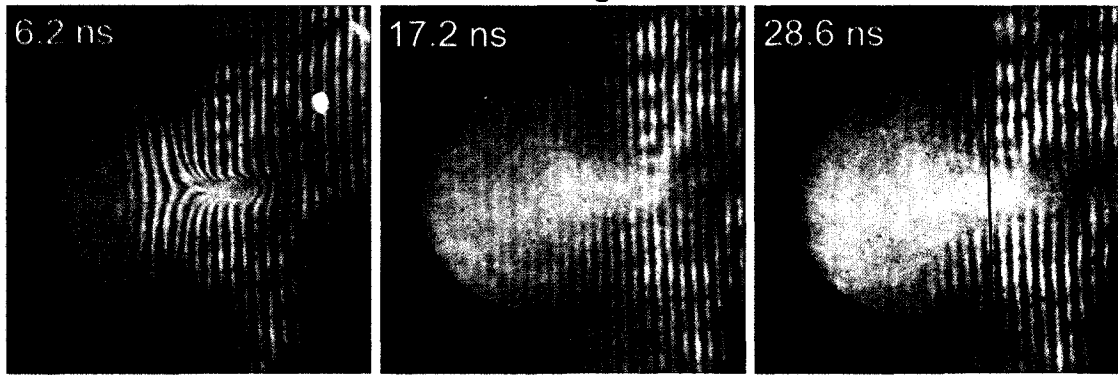


Figure 4.19: Soft x-ray interferometry data similar to that in Figures 4.10 and 4.12 showing that for the case of copper no anomalous fringe shifts are observed.

very complex structure near 26.5 eV for 2 and 5 eV. For the case of doubly ionized copper the average atom method predicts that the ratio should be 1, but this value will have a large error due to the structure present. For 10 and 20 eV the ratio is also close to 1 and the structure seems to be disappearing. This suggests that it is possible to use interferometry at 46.9 nm to confidently probe relatively highly ionized copper plasmas. These results support the conclusion that the density depression unveiled in section 3.1 is formed through the proposed mechanisms and is not intensified by the contribution of bound electrons in the colder side wings of the plasma.

Interferometry experiments performed using aluminum and molybdenum as target materials showed a very similar behavior to that of copper. No negative fringe shifts were observed at any point in the evolution of these plasmas either.

The fact that, as predicted by the model, copper and aluminum did not show negative fringe shifts in experiments under very similar conditions as those done with tin, silver and carbon plasmas supports the conclusion that the anomalous fringe shifts are caused by the contribution of bound electrons to the index of

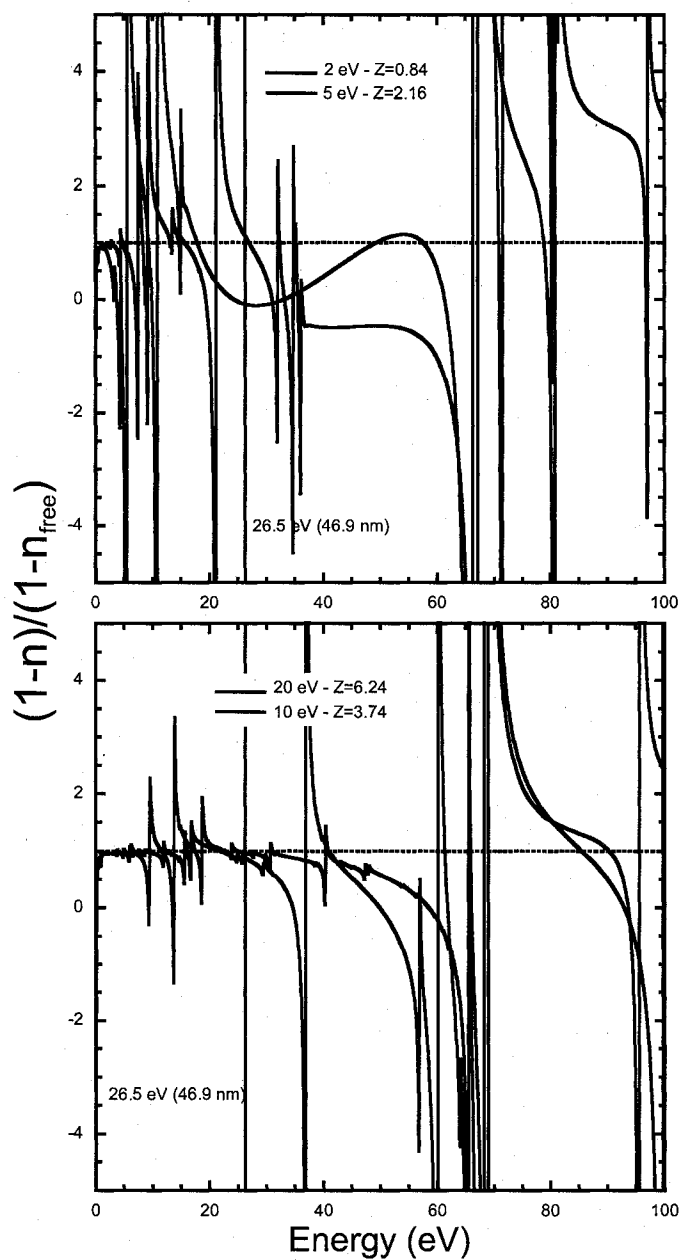


Figure 4.20: Index of refraction for copper plasmas computed using the Average Atom code. The plasma used had a density of 10^{20} cm^{-3} . A value of $(1 - \eta)/(1 - \eta_{free})$ of 1 indicates that the contribution is solely due to free electrons.

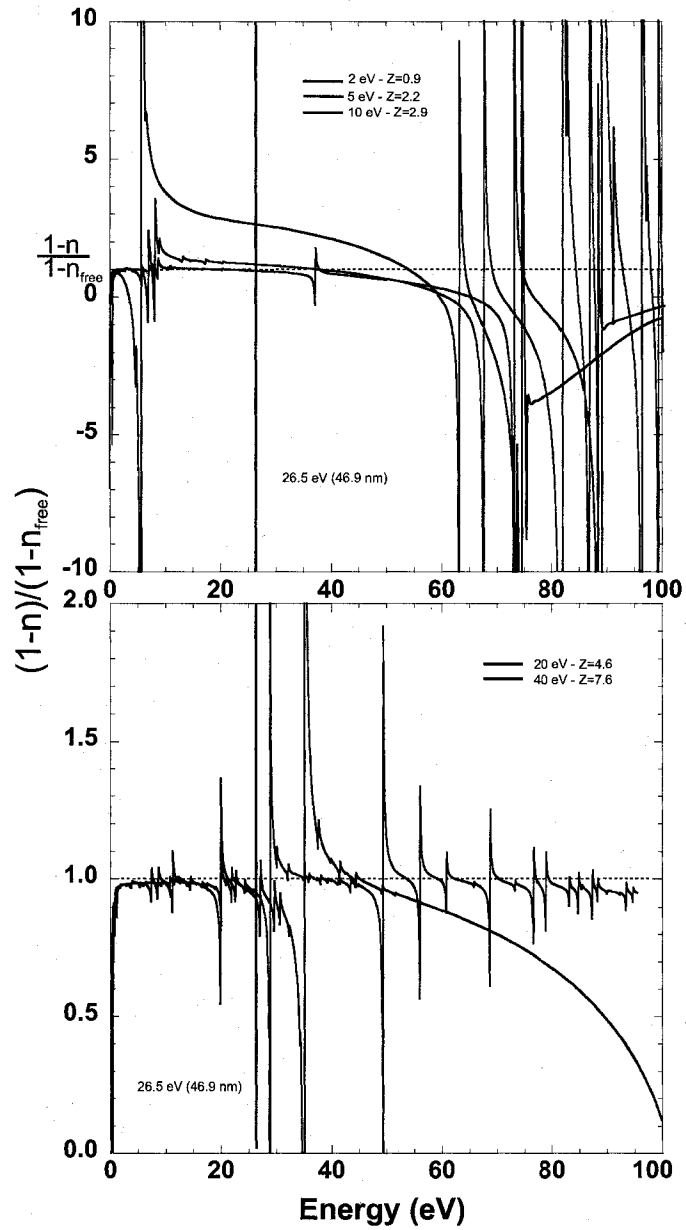


Figure 4.21: Average atom calculation of an aluminum plasma with a density of 10^{20} cm^{-3} . A value of $(1 - \eta)/(1 - \eta_{free})$ of 1 indicates that the contribution is solely due to free electrons.

refraction and are not caused by a density depression arising from the evolution of the plasma, or by refraction effects due to gradients in the plasma.

4.11 Conclusions

For decades the analysis of plasma diagnostics, such as interferometry, have relied on the approximation that the index of refraction in plasmas is due solely to the free electrons. Analysis of the aluminum plasmas soft x-ray interferometric data at 14.7 nm probe wavelengths demonstrated that bound electrons can contribute significantly to the index of refraction of multiply ionized plasmas in the vicinity of absorption lines and edges. Further studies in tin, silver and copper plasmas at 46.9 nm probe wavelength expanded the known conditions where the effects occurs. The ions responsible for the anomalous index of refraction varied: for the case of aluminum, the contribution was found to be aluminum ions Al II through Al VI. For Carbon, tin and silver C III, Sn III and Ag III were computed to be responsible for the effect. However, the importance of the bound electron contribution is not always limited to plasmas with a low mean ion charge. For example, ten times ionized Pd atoms are computed to have an f_1^0 value that is several times that of the corresponding number of free electrons, with the precise value of f_1^0 depending strongly on the position of the resonance line [4.29]. It is also important to realize that the relative contribution of bound electron scattering is not always clearly evident in soft x-ray interferograms because at these wavelengths the free and bound electrons often contribute with the same sign to the phase delay (as is the case for Pd at 14.7 nm).

The possible contribution of multiple ions to the index of refraction precludes a quantitative analysis of the interferogram. In these cases an estimate of the

electron density is not possible without knowledge of the atomic scattering factors and the use of additional tools to estimate the ion charge distribution, such as time resolved spectroscopy and modeling. Nevertheless, most hot plasmas that are many times ionized can be confidently probed using soft X-ray laser interferometry, and it is possible to select the probe wavelengths to avoid the contribution from bound electrons to the index in the particular plasma of interest. Also it is possible, as was shown for the case of Carbon plasmas, to use simulations to validate regions in the plasma where the bound electron contribution is small, or validate times in the evolution where the approximation is valid, as was the case for the aluminum plasmas probed at 14.7 nm. This shows the need to do some theoretical modeling of the plasma to verify that experiments are being done in a regime where the free electron approximation for the index of refraction is valid.

While soft x-ray laser interferometry allows measurements of higher plasma densities because of better spatial resolution, reduced absorption and reduced deflection angles within steep plasma density gradients, neglecting the contribution of bound electrons to the index of refraction could, in some cases, constitute a significant systematic error in the determination of the electron density. As X-ray free electron lasers and other sources become available [4.38] during the next decade to probe a wider variety of plasmas at higher densities the contribution of bound electrons to the index of refraction will have to be taken into account.

Bibliography

- 4.1 D. T. Attwood, D. W. Sweeney, J. M. Auerbach, and P.H.Y. Lee. Interferometric Confirmation of Radiation-Pressure Effects in Laser-Plasma Interactions. *Phys. Rev. Lett*, 40:184–187, 1978.
- 4.2 G. J. Tallents. Interferometry and refraction measurements in plasmas of elliptical cross-section . *Journal of Physics D Applied Physics*, 17:721–732, April 1984.
- 4.3 H. R. Griem. *Principles of Plasma Spectroscopy*, page 9. Cambridge University Press, 1997.
- 4.4 L. B. Da Silva, T. W. Barbee Jr., R. Cauble, P. Celliers, D. Ciarlo, S. Libby, R. A. London, D. Matthews, S. Mrowka, J. C. Moreno, D. Ress, J.E. Trebes, A. S. Wan, and F. Weber. Electron density measurements of high density plasmas using soft x-ray laser interferometry. *Physical Review Letters*, 74(20):3991, 1995.
- 4.5 J. J. Rocca, C. H. Moreno, M. C. Marconi, and K. Kanizay. Soft-x-ray laser interferometry of a plasma with a tabletop laser and a Lloyd's mirror. *Optics Letters*, 24(6):420–422, 1999.

- 4.6 C. H. Moreno, M. C. Marconi, K. Kanizay, J. J. Rocca, Y. A. Uspenskii, A. V. Vinogradov, and Y. A. Pershin. Soft-x-ray laser interferometry of a pinch discharge using a tabletop laser. *Physical Review E*, 60(1):911–917, 1999.
- 4.7 J. Filevich, K. Kanizay, M. C. Marconi, J. L. A. Chilla, and J. J. Rocca. Dense plasma diagnostics with an amplitude-division soft-x-ray laser interferometer based on diffraction gratings. *Optics Letters*, 25(5):356–358, 2000.
- 4.8 R. F. Smith, J. Dunn, J. Nilsen, V. N. Shlyaptsev, S. Moon, J. Filevich, J. J. Rocca, M. C. Marconi, J. R. Hunter, and T. W. Barbee. Picosecond X-Ray Laser Interferometry of Dense Plasmas. *Physical Review Letters*, 89(6):065004–+, July 2002.
- 4.9 J. J. Rocca, E. C. Hammarsten, E. Jankowska, J. Filevich, M. C. Marconi, S. Moon, and V. N. Shlyaptsev. Application of extremely compact capillary discharge soft x-ray lasers to dense plasma diagnostics. *Physics of Plasmas*, 10(5):2031–2038, 2003.
- 4.10 J. Filevich, J. J. Rocca, E. Jankowska, E. C. Hammarsten, K. Kanizay, M. C. Marconi, S. J. Moon, and V. N. Shlyaptsev. Two-dimensional effects in laser-created plasmas measured with soft-x-ray laser interferometry. *Physical Review E*, 67(5):056409, 2003.
- 4.11 F. Albert, D. Joyeux, P. Jaegle, A. Carillon, J. P. Chauvineau, G. Jamelot, A. Klisnick, J. C. Lagron, D. Phalippou, D. Ros, S. Sebban, and P. Zeitoun. Interferograms obtained with an x-ray laser by means of a wavefront division interferometer. *Optics Communications*, 142:184–188, 1997.

- 4.12 D. Descamps, C. Lyngå, J. Norin, A. L'Huillier, C.-G. Wahlström, J.-F. Hergott, H. Merdji, P. Salières, M. Bellini, and T. W. Hänsch. Extreme ultraviolet interferometry measurements with high-order harmonics. *Optics Letters*, 25:135–137, January 2000.
- 4.13 J. Filevich, J.J. Rocca, M.C. Marconi, S.J. Moon, J. Nilsen, J.H. Scofield, J. Dunn, R.F. Smith, R. Keenan, J.R. Hunter, and V.N. Shlyaptsev. Observation of a multiply ionized plasma with index of refraction greater than one. *Physical Review Letters*, 94(035005), 2005.
- 4.14 H. Tang, O. Guilbaud, G. Jamelot, D. Ros, A. Klisnick, D. Joyeux, D. Phalippou, M. Kado, M. Nishikino, M. Kishimoto, K. Sukegawa, M. Ishino, K. Nagashima, and H. Daido. Diagnostics of laser-induced plasma with soft X-ray (13.9 nm) bi-mirror interference microscopy. *Applied Physics B: Lasers and Optics*, 78:975–977, 2004.
- 4.15 Jim Scofield. Private Communication, 2004.
- 4.16 G. D. Zimmerman and W. L. Kruer. Numerical simulation of laser-initiated fusion. *Comments Plasma Phys. Controlled Fusion*, 2:51, 1975.
- 4.17 J. Nilsen and J. H. Scofield. Plasmas with an index of refraction greater than 1. *Optics Letters*, 29:2677–2679, November 2004.
- 4.18 J. Nilsen and W. R. Johnson. Plasma interferometry and how the bound-electron contribution can bend fringes in unexpected ways. *ao*, 44:7295–7301, December 2005.

- 4.19 J. Nilsen, W. R. Johnson, C. A. Iglesias, and J. H. Scofield. Impact of anomalous dispersion on the interferometer measurements of plasmas. *Journal of Quantitative Spectroscopy and Radiative Transfer*, 99:425–438, May 2006.
- 4.20 W. R. Johnson, C. Guet, and G. F. Bertsch. Optical properties of plasmas based on an average-atom model. *Journal of Quantitative Spectroscopy and Radiative Transfer*, 99:327–340, May 2006.
- 4.21 J. L. A. Chilla, J. J. Rocca, O. E. Martinez, and M.C. Marconi. Soft x-ray interferometer for single-shot laser linewidth measurements. *Optics Letters*, 21(13):955–957, 1996.
- 4.22 J. Filevich, J. J. Rocca, M. C. Marconi, R. F. Smith, J. Dunn, R. Keenan, J.R. Hunter, S.J. Moon, J. Nilsen, A. Ng, V. N. Shlyaptsev, and T. W. Barbee. Picosecond resolution soft x-ray laser plasma interferometry. *Applied Optics*, 43(19), July 2004.
- 4.23 J. Dunn, R. F. Smith, R. Shepherd, R. Booth, J. Nilsen, J. R. Hunter, and V. N. Shlyaptsev. Temporal characterization of a picosecond laser-pumped x-ray laser (for applications). In E. E. Fill and S. Suckewer, editors, *SPIE Int. Soc. Opt. Eng. Proc*, volume 5197, pages 51–59, 2003.
- 4.24 J. Dunn, Y. Li, A. L. Osterheld, J. Nilsen, J. R. Hunter, and V. N. Shlyaptsev. Gain saturation regime for laser-driven tabletop, transient Ni-like ion x-ray lasers. *Physical Review Letters*, 84(21):4834–4837, 2000.
- 4.25 B. L. Henke, E. M. Gullikson, and J. C. Davis. X-ray interactions : photoabsorption, scattering, transmission, and reflection at $E = 50\text{--}30000$ eV, $Z=1\text{--}92$. *Atomic Data and Nuclear Data Tables*, 54(2):181–342, 1993.

- 4.26 E. M. Gullikson, P. Denham, S. Mrowka, and J. H. Underwood. Absolute photoabsorption measurements of Mg, Al, and Si in the soft-x-ray region below the L_{2,3} edges. *Physical Review B*, 49:16283–8, 1994.
- 4.27 A. Aguilar, J. B. West, R. A. Phaneuf, R. L. Brooks, F. Folkmann, H. Kjeldsen, J. D. Bozek, A. S. Schlachter, and C. Cisneros. Photoionization of isoelectronic ions: mg^+ and al^{2+} . *Physical Review A*, 67:012701, 2003.
- 4.28 I. M. Savukov. Accurate calculations of energies and oscillator strengths for light neon-like ions. *Journal of Physics B: Atomic, Molecular and Optical Physics*, 36(24):4789–4797, 2003.
- 4.29 J. Nilsen and J. H. Scofield. Applications of x-ray laser utilizing plasmas that are only a few times ionised. *UCRL-PROC-204652*, 2004. Livermore, CA.
- 4.30 D. A. Liberman. INFERNO - A better model of atoms in dense plasmas. *Journal of Quantitative Spectroscopy and Radiative Transfer*, 27:335–339, March 1982.
- 4.31 D A Greenwood. The Boltzmann equation in the theory of electrical conduction in metals. *Proceedings of the Physical Society*, 71(4):585–596, 1958.
- 4.32 Kubo, R. *Journal Physical Society of Japan*, 12:570, 1957.
- 4.33 P. Dunne, F. O'Reilly, G. O'Sullivan, and N. Murphy. LETTER TO THE EDITOR: 4d photoabsorption in Sn III. *Journal of Physics B Atomic Molecular Physics*, 32:L597–L602, October 1999.
- 4.34 B. R. Benware, C. D. Macchietto, C. H. Moreno, and J. J. Rocca. Demonstration of a high average power tabletop soft x-ray laser. *Physical Review Letters*, 81(26):5804–5807, 1998.

- 4.35 Mike Purvis, Jonathan Grava, Jorge Filevich, Mario C. Marconi, Jorge J. Rocca, James Dunn, Stephen J. Moon, Vyacheslav N. Shlyaptsev, and Elizabeth Jankowska. Dynamics of converging laser-created plasmas in semi-cylindrical cavities studied using soft x-ray laser interferometry. *Submitted to PRE*, 2007.
- 4.36 Y. A. Uspenskii, V. E. Levashov, A. V. Vinogradov, A. I. Fedorenko, V. V. Kondratenko, Y. P. Pershin, E. N. Zubarev, and V. Y. Fedotov. High-reflectivity multilayer mirrors for a vacuum-ultraviolet interval of 35-50 nm. *Optics Letters*, 23:771, 1998.
- 4.37 I. P. Grant, B. J. McKenzie, P. H. Norrington, D. F. Mayers, and N. C. Pyper. An atomic multiconfigurational Dirac-Fock package. *Computer Physics Communications*, 21:207–231, December 1980.
- 4.38 A. Meseck, M. Abo-Bakr, D. Krämer, B. Kuske, and S. Reiche. BESSY soft X-ray FEL. *Nuclear Instruments and Methods in Physics Research A*, 528:577–581, August 2004.

Chapter 5

SUMMARY

In conclusion, this Dissertation presented results of newly observed phenomena in dense plasmas resulting from soft x-ray laser interferometry experiments. The study made use of a new soft x-ray interferometer that is capable of diagnosing large scale high density plasmas. This Diffraction Grating Interferometer design, which uses diffraction gratings as beam splitters, results in a robust setup that is very well suited for plasma diagnostics. Two versions of the interferometer were successfully constructed to work in combination with soft x-ray lasers operating at two different wavelengths (46.9 nm and 14.7 nm) and with two different pulse durations (1 ns and 5 ps) and were tested with excellent fringe visibility over, at least, the whole detector area. These two interferometry setups have produced a large amount of data, probing plasma densities up to a few μm away from the target surface and to densities that are very close to the heating beam critical density: $\sim 1 \times 10^{21} \text{ cm}^{-3}$. The data obtained have been used to understand new plasma phenomena and to compare with hydrodynamic simulations to benchmark these codes.

The experimental results presented in chapter 3 show a very noticeable on-axis density depression, observed in plasmas that were generated under very different irradiation conditions: a 13 ns long laser pulse both in a line focus and a spot focus illuminating copper targets and a 600 ps short laser pulse in a line focus illuminating aluminum targets. By combining the experimental results with two dimensional hydrodynamic LASNEX simulations the effect was understood. For all the cases studied, the main mechanism responsible for the density depression is the build-up of cold material generated by an increased ablated area caused mainly by XUV plasma radiation emitted from the central hot region in the plasma, combined with pressure balance due to the difference in temperature between this hot central

region and the colder sidelobes. The simulations indicate that the formation of a central density depression is essentially a universal effect that should be observed over a relatively wide range of plasma parameters.

The soft x-ray plasma interferometry experiments presented in chapter 4 demonstrated that bound electrons can contribute significantly to the index of refraction of multiply ionized plasmas in the vicinity of absorption lines and edges. The assumption that only the free electrons contribute to the index of refraction has been widely used in the analysis of plasma diagnostics experiments, including all soft x-ray laser plasma diagnostics to date. The bound electron contribution to the index of refraction was first observed in aluminum plasmas probed at 14.7 nm wavelengths and then, in further studies, in tin, silver and copper plasmas at 46.9 nm probe wavelength.

The ions most responsible for the bound electron contribution to the index of refraction varied: for the case of aluminum probed at 14.7 nm, the contribution was found to be strongest in the ions Al II through Al VI. For carbon, tin and silver, C III, Sn III and Ag III were computed to be responsible for the effect. However, the importance of the bound electron contribution is not always limited to plasmas with a low mean ion charge. For example, ten times ionized Pd atoms are computed to have a significant contribution at 14.7 nm. It is also important to realize that the relative contribution of bound electron scattering is not always clearly evident in soft x-ray interferograms because at these wavelengths the free and bound electrons often contribute with the same sign to the phase delay (as is the case for Pd at 14.7 nm). In those cases, the effect would most likely remain hidden and the measured electron density would be an overestimation of the actual value.

In cases where ions contribute to the index of refraction an estimate of the electron density is not possible without knowledge of the atomic scattering factors

and the use of additional tools to estimate the ion charge distribution, such as a combination of time resolved spectroscopy and modeling. Nevertheless, most hot plasmas that are many times ionized can be confidently probed using soft x-ray laser interferometry, and it is possible to select the probe wavelengths to avoid the contribution from bound electrons to the index in the particular plasma of interest. It is also possible to use simulations results to validate regions in the plasma where the bound electron contribution is small. While soft x-ray laser interferometry allows measurements of higher plasma densities because of better spatial resolution, reduced absorption and reduced deflection angles within steep plasma density gradients, neglecting the contribution of bound electrons to the index of refraction could, in some cases, constitute a significant systematic error in the determination of the electron density.

The results presented here constitute the first demonstration of the use of table-top soft x-ray laser interferometry in the study of complex high density plasma phenomena. The Diffraction Grating Interferometer is scalable to significantly shorter wavelengths, and constitutes a promising scheme for extending interferometry to the study of very dense plasmas such as those investigated for inertial confinement fusion.